UNIVERSITA' DEGLI STUDI DI PAVIA

FACOLTA' DI INGEGNERIA
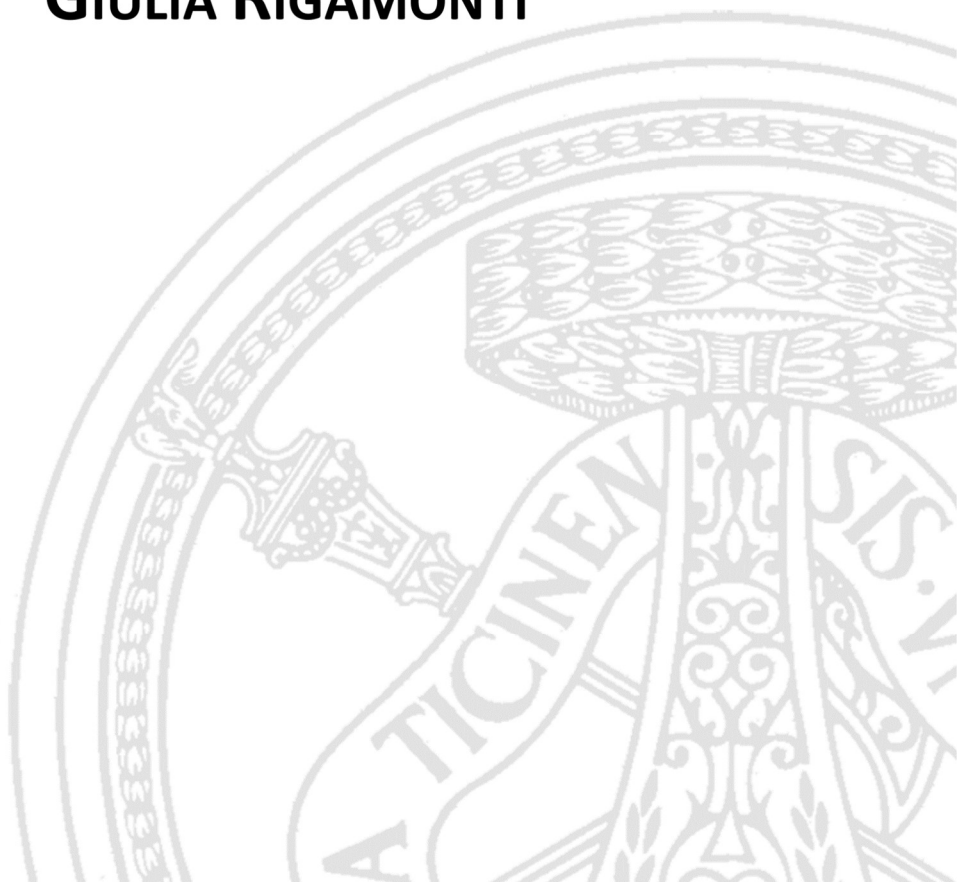### DIPARTIMENTO DI INGEGNERIA INDUSTRIALE E DELL'INFORMAZIONE

DOTTORATO DI RICERCA IN BIOINGEGNERIA E BIOINFORMATICA
XXX CICLO - 2017

DEVELOPMENT OF OPTICAL BIOSENSORS AND IMAGING SYSTEMS BASED ON INTERFERENCE EFFECTS

PhD Thesis by
GIULIA RIGAMONTI

Advisor:
Prof. Sabina Merlo

PhD Program Chair:
Prof. Riccardo Bellazzi

Acknowledgments

First of all, I would like to express my truthful gratitude to Prof. Sabina Merlo, my PhD advisor, for her constant help, guidance, motivation and support. I would like to extend my gratitude to Prof. Giuliano Mazzini, for all the fruitful discussions and his contributions to the activities on cell culture. Thank as well to Dr. Riccardo Vicini, Dr. Anna Ivana Scovassi and Dr. Ennio Prosperi, for providing the cell samples. My gratitude goes as well to Dr. Francesca Carpignano for the help and collaboration in part of the presented activities.

I want to express my gratitude to Prof. Selim Unlu for accepting me in his research group, giving me the opportunity to join a cutting edge research reality. My sincere thanks also goes to Dr. Derin Sevenler for helping me during my stay at the OCN laboratory, and to all the other group members for the warm welcome and their help: Steve, Oguzhan, Fulia, Elif and Jake.

A special thanks to all the people from LabEO, with a particular mention to Andrea Fanzio for his technical support, and to all the guys part of the PhD program: thank to you all for the unique moments spent together during these years.

I want to thank as well Prof. Marcella Chiari and Prof. Maria Pesavento for providing help and materials for the devices functionalization experiments as well as Prof. Ferdinando Auricchio and Dr. Stefania Marconi for the fruitful collaboration in the design and fabrication of the 3D-printed support device within the sensor development project.

Finally, I would like to express all my gratitude to my family, my lifelong friends, and, last but not the least, to Paolo.

IV

List of Abbreviations

λ_c	Central emission wavelength of the optical source
1D	One-dimensional
2D	Two dimensional
3D	Three-dimensional
A/D	Analog to Digital
ASE	Amplified Spontaneous Emission
AuNP	Gold Nanoparticle
BSA	Bovine Serum Albumin
C1,C2	Couplers
CCD	Charge-Coupled Device
CFBG	Chirped Fiber Bragg Grating
CHT	Circular Hough Transform
CMOS	Complementary Metal-Oxide Semiconductor
DC	Direct Current
DLP	Digital Light Processing
DMA	Dimethylacetamide
D-MEM	Dulbecco's Modified Eagle's Medium
EFA	Evanescent Field Absorption
EG	Ethylene Glycol
FBG	Fiber Bragg Grating
FBS	Fetal Bovine Serum
FCS	Fetal Calf Serum
FFT	Fast Fourier Transform
FO	Fiber Optic
FOV	Field of View
FPI	Fabry-Pérot Interferometer
FSC	Forward Scattering
FSR	Free Spectral Range
FWHM	Full Width Half Maximum
HSA	Human Serum Albumin
HUVEC	Human umbilical vein endothelial cells
IR	Infrared
IRIS	Interferometric Reflectance Imaging Sensor
L_C	Coherence length
LCORR	Liquid Core Optical Ring Resonator
LD	Laser Diode
LoD	Limit of Detection
LPFG	Long Period Fiber Gratings

MAPS	[3-(methacryloyl-oxy)propyl]trimethoxysilyl
MEMS	Micro Electro-Mechanical Systems
MI	Michelson Interferometer
MIP	Molecularly Imprinted Polymer
MM	Mismatch
MMF	Multimode Fiber
MOF	Microstructured Optical Fiber
MZI	Mach-Zehnder Interferometer
NA	Numerical Aperture
NaPB	Sodium Phosphate
NAS	N,N-acryloyloxysuccinimide
NIR	Near Infrared
NOSA	Nanoscale Optofluidic Sensor Array
OCT	Optical Coherence Tomography
OI	Optical Isolator
OP	Optical Path
OSA	Optical Spectrum Analyzer
PBG	Photonic Bandgap
PBS	Phosphate-Buffered Saline
PD	Photodiode
PhC	Photonic Crystal
PI	Propidium Iodide
PM	Perfect Match
PMMA	Poly(methyl methacrylate)
R	Reflectivity
RBC	Red Blood Cell
RCF	Relative Centrifugal Force
RI	Refractive index
RPMI 1640	Roswell Park Memorial Institute medium
RPMI-7951	Roswell Park Memorial Institute melanoma cells
S	Sensitivity
Si	Silicon
SiO_2	Silicon Dioxide
SiON	Silicon Oxynitride
Si_3N_4	Silicon Nitride
SLED	Superluminescent Light Emitting Diode
SMF	Single Mode Fiber
SNP	Single Nucleotide Polymorphism
SP-IRIS	Single Particle Interferometric Reflectance Imaging Sensor
SPR	Surface Plasmon Resonance
SPW	Surface Plasmon Wave
SSC	Saline-Sodium Citrate
STL	Standard Triangulation Format
Ta_2O_5	Tantalum Pentoxide
THP-1	Human leukemic monocyte
WGM	Whispering Gallery Mode
WT	Wild-type

Abstract (Italiano)

L'interferometria ottica è una tecnica ampiamente utilzzata in vari ambiti, basata sul ben noto fenomeno fisico dell'interferenza della luce come onda. Le tecniche interferometriche trovano ad oggi utilizzo in vari campi, con applicazioni che vanno dall'astronomia e la radioastionomia fino alla diagnostica medica. Le attività svolte durante il mio dottorato di ricerca si sono principlamente concentrate sull'utilizzo degli effetti dell'interferenza luminosa per lo sviluppo e l'applicazione di biosensori ottici e sistemi di imaging. La principale attività su cui mi sono concentrata ha riguardato lo sviluppo di un sensore biochimico micro-opto-fluidico e *label-free* (ovvero che non richiede l'utilizzo di marcatori) che sfrutta effetti di interferenza di sorgenti luminose nel vicino infrarosso. Negli ultimi anni, un interesse sempre crescente è stato rivolto allo sviluppo di sensori ottici biologici e biochimici per il monitoraggio della salute e della qualità, con particolare attenzione ad aspetti quali la miniaturizzazione, la bassa invasività e il basso costo. L'economicità, in particolare, è fortemente desiderabile nei settori clinico e biomedico, nei quali l'utilizzo di sensori usa e getta ha la potenzialità di ridurre i rischi di contaminazione. La miniaturizzazione è un altro fattore particolarmente importante, dal momento che consente di lavorare con piccoli volumi di campione, di ridurre il tempo di risposta, di migliorare il controllo dei processi e di realizzare strumenti portabili. In questa tesi viene discusso lo sviluppo di un sistema di *sensing* basato su un setup riconfigurabile completamente realizzato in fibra ottica per la rivelazione volumetrica dell'indice di rifrazione di fluidi che sfrutta effetti di interferenza su dispositivi commericiali. Il sistema proposto risponde ai requisiti sopracitati. Infatti, la rivelazione ottica è stata realizzata utilizzando sorgenti ottiche nel vicino infrarosso, un intervallo di lunghezze d'onda dove l'assorbimento, e quindi l'invasività per i tessuti biologici è minimo. E' stato inoltre possibile lavorare con dispositivi miniaturizzati, dal momento che l'indice di rifrazione di una soluzione dipende dalla concentrazione dell'analita e non dal numero totale di molecole. In particolare, abbiamo investigato diversi dispositivi con dimensioni carattereristiche che vanno da qualche a centinaia di micrometri, ovvero capillari rettangolari in vetro a sezione rettangolare, commercializzati da Vitrocom™, e *μ-slides* polimeriche commerializzate da IBIDI™. Entrambi i dispositivi sono perfettamente adatti per l'*imaging* ottico; in aggiunta, sono dispositivi commercialmente

disponibili a basso costo, consentendo pertanto la realizzazione di sensori usa e getta. Attraverso misure di interferometria a bassa coerenza abbiamo ricavato l'indice di rifrazione sia di soluzioni omogenee (inserite in vari tipi di dispositivi), sia di sostanze altamente diffondenti, come popolazioni di cellule in condizioni normali e tumorali, confinate in microcapillari rettangolari in vetro.

Grazie alla loro struttura simmetrica, i capillari sono inoltre adatti per la rivelazione di indici di rifrazione di fluidi tramite misure spettrali. In particolare, sono state realizzate misurazioni sperimentali di riflettività (R) e trasmissività (T) spettrale, e, tramite monitoraggio del rapporto T/R, sono state rivelate variazioni indice di rifrazione, ottenendo sensibilità e limiti di rivelazione comparabili a valori reperiti in letteratura ottenuti su dispositivi più complessi e costosi. La rivelazione della potenza ottica sia riflessa che trasmessa consente di eliminare eventuali fluttuazioni della sorgente di lettura, rendendo il sistema adatto anche per la rivelazione in ampiezza realizzata a singola lunghezza d'onda.

La seconda attività che ho portato avanti durante il dottorato di ricerca ha riguardato il monitoraggio *label-free* e *real-time* di sequenze nucleotidiche attraverso *l'Interferometric Reflectance Imaging Sensor* (IRIS), una piattaforma di *imaging* che consente la rivelazione ottica di varie biomolecole in maniera altamente sensibile, riproducibile e *high-throughput*. IRIS è stato realizzato presso il Laboratorio di Caratterizzazione Ottica e Nanofotonica della Boston University, Boston, Massachussetts. In particolare, ho sfruttato IRIS per il monitoraggio della denaturazione di sequenze nucleotidiche indotta da variazioni di temperatura, in modo da comprendere meglio le proprietà termodinamiche di sequenze di interesse nella ricerca oncologica.

A margine, ma di nuovo collegato al tema dell'interferenza ottica, è descritto un metodo innovativo per la generazione di luce strutturata nel vicino infrarosso basato su sistemi microelettromeccanici per l'*imaging* tridimensionale (3D). Negli ultimi anni, lo sviluppo di sistemi di *imaging* 3D è stato oggetto di grande interesse, dal momento che le possibili applicazioni trovano spazio in diversi campi, tra cui quello automotive, della microsopia a superisoluzione, della scienza terrestre e l'*imaging* medico. L'utilizzo di luce strutturata si è dimostrato particolarmente interessante per la rivelazione di oggetti e il rivelamento del movimento. In questa tesi viene discussa la realizzazione di un sistema ottico per la generazione di luce strutturata e la sua applicazione alla rivelazione della profondità di oggetti.

Abstract (English)

Optical interferometry is a widely employed technique, relying on the well-known physical phenomenon of interference of light as a wave. Interferometric techniques are nowadays applied in several fields, with applications going from astronomy and radioastronomy to medical diagnostic. The research activities conducted during my PhD have been mainly focused on the exploitation of light interference effects for the development and application of optical biosensors and imaging systems. The principal activity I carried out has been devoted to the development of a label-free (i.e. not requiring exogenous markers) micro-opto-fluidic biochemical sensor exploiting interference effects in the near-infrared (NIR). In the last decades, a growing interest has been addressed to the development of optical biological and biochemical sensors for health and quality monitoring, with particular attention to miniaturization, low-invasiveness and low-cost. Low-cost is particularly desirable in the clinical and biomedical field, where the employment of disposable sensors would reduce cross-contamination risks. Miniaturization is as well strongly enviable, since it allows to deal with smaller sample volumes, reduces the response time, improves the process control and enables for the realization of portable instruments. In this dissertation, the development of a sensing system based on an all-fiber reconfigurable setup allowing volumetric refractive index (RI) detection by exploiting interference effects on off-the-shelf disposable devices is presented. The proposed system answers the previously cited requirements. In fact, optical detection was performed with non-contact, remote optical read-out exploiting near-infrared sources, thus emitting in a wavelength region where the absorption, and thus the invasiveness for biological samples is particularly low. Since the RI of a solution scales with the analyte concentration rather than with the total number of molecules, miniaturization was also exploitable. In particular, we investigated several devices with characteristic dimensions from a few micrometers up to hundreds of micrometers, i.e. rectangular glass-micro capillaries commercialized by Vitrocom™, and polymeric μ-slides commercialized by IBIDI™. Both kinds of device are perfectly suitable for the optical imaging; moreover, they are low-cost off-the-shelf devices, thus enabling for the realization of disposable sensors. Through low-coherence interferometric measurements we were able to retrieve the RI of homogenous solutions (contained in various types of devices) as well as of highly scattering media, such as population of cells in normal and malignant condition gently confined in rectangular glass micro-capillaries.

Thanks to their symmetrical structure, capillaries are as well particularly suited for RI detection by means of spectral measurements. In particular, we measured both transmissivity (T) and reflectivity (R) spectra, and, by monitoring the T/R spectral ratio, we detected RI variations obtaining sensitivity and limit of detection (LoD) values comparable to those find in the literature relative to more complex and expensive devices. Collection of both T and R spectra enabled for source fluctuation compensation, making the system suitable also for single wavelength amplitude detection.

The second activity I have carried out during my PhD regarded the label-free real-time monitoring of nucleotide sequences through the Interferometric Reflectance Imaging Sensor (IRIS), an imaging platform enabling for the optical detection of various biomolecules with high-throughput, high sensitivity and reproducibility. IRIS was developed by the Laboratory of Optical Characterization and Nanophotonics (OCN) of Boston University, Boston, Massachusetts. In particular, I applied the system to the monitoring of nucleotide sequences dehybridization induced by temperature variation, in order to better understand the thermodynamic properties of sequences of interest in cancer investigation.

As an aside, but again related to optical interference effects, an innovative method for generating infrared (IR) structured light based on microelectromechanical systems (MEMS) for three-dimensional (3D) imaging was investigated. In the last decades, 3D-imaging system development has been object of great interest, since possible applications find place in several field, such as automotive, super-resolution microscopy, earth science and medical imaging. Structured light approaches have been demonstrated particularly interesting for object detection and motion tracking. The realized optical system and its application to object depth perception is discussed.

Contents

Introduction

Light interference is a well-known physical phenomenon relying on the wave theory of light, firstly demonstrated by Thomas Young through the double-slit experiment in 1803 [1], that opened the way to the development of a wide class of optical interferometric techniques. In 1965, with the advent of the first lasers, a new class of interferometry-based instruments, able to measure vibrations and displacement with sub-micrometric resolution, spread rapidly [2]. Nowadays, optical interferometry is widely employed in several fields and applications, such as astronomy, remote sensing, biochemical sensing, and medical diagnostic. In the medical field, interferometry is for example at the basis of Optical Coherence Tomography (OCT), an established diagnostic imaging technique for the high resolution and 3D imaging of highly scattering media such as biological tissues.

In the course of my PhD, I have investigated the potentiality of light interference for the development of optical biosensors and advanced imaging systems. Main activity has been devoted to the development of a label-free micro-fluidic chemical sensor based on low-cost disposable devices exploiting light interference in the near-infrared region.

Over the years, a growing interest has been addressed to the monitoring of health, food quality, environmental conditions, and quality of life. Following this need, many chemical and biochemical sensors have been proposed in the last decades. Among the others, optical detection methods offer several advantages, allowing a fast, high-sensitive and low-invasive detection. In particular, label-free detection, not requiring exogenous markers, represents a cheaper solution, with lower risk of error and the capability of performing real-time detection. With the technological advance, sensors have moved from bulky devices to miniaturized systems that can be easily integrated with fluidic systems and electronic components. In the biomedical field, the development of low-cost miniaturized disposable sensors is still an open field of research, and a lot of effort has been put by researchers in developing more and more performant sensors. Low-cost is a factor of particular interest in sensors for biomedical application, where the use of disposable devices could reduce carry-over and cross-contamination. Miniaturization of analytical systems has great impact, since it allows to deal with smaller sample volumes, reduces the response time, improves the process control and enables for the realization of portable instruments.

In my dissertation, to answer to the listed needs, I am going to present the development of a sensing platform based on an all-fiber reconfigurable setup allowing to perform RI detection of fluids of biological interest in off-the-shelf disposable micro-devices.

As a secondary activity, label-free real-time monitoring of nucleotide sequences interaction has been realized exploiting the IRIS (Interferometric Reflectance Imaging System) platform, developed by the OCN Laboratory at Boston University, Boston, Massachusetts, USA. IRIS exploits optical interferometry and spectroscopy to detect and quantify particle accumulation on a bilayer chip composed by silicon and silicon dioxide (SiO_2/Si) in a microarray format.

As an aside, but again related to optical interference effects, I am going to illustrate an innovative method for the generation of infrared structured light based on MEMS systems for 3D imaging. In the last decades, 3D imaging systems have been object of great interest. In fact, most of the existing cameras are just suitable for the collection of 2D images, but are unable to retrieve information about the object depth. 3D imaging systems for objects recognition and movement tracking are of great impact in several field, such as automotive, super-resolution microscopy, earth science and medical imaging. With the advance of technology, the availability of miniaturized components and new techniques lead to the development and commercialization of a wide range of products. New generations of cellular phones are already announced to host miniaturized 3D imaging systems.

All the above mentioned activities have the common denominator of exploiting optical interference effects to enable an efficient detection.

Activities related to the development of the structured light generation system and of the micro-opto-fluidic sensor have been conducted at the ElectroOptics Laboratory of Electrical and Computer Engineering of the University of Pavia, Pavia, Italy, whereas activities concerning the IRIS system have been realized at the OCN Laboratory, Boston University, Boston, Massachusetts, USA.

Here, a brief summary of this dissertation is reported.

Chapter 1: after a review of the state of the art in the field of optical biosensing, I will describe the employed off-the-shelf devices. i.e. rectangular glass micro-capillaries as well as micro-fluidic polymeric slides, and their main sensing applications. Then, the reconfigurable setup employed to perform refractometric measurements based on low-coherence interferometry and spectral detection in the near-infrared will be presented.

In Chapter 2 I will illustrate the theoretical background of low-coherence interferometry and the experimental results collected thanks to its application in sensing. The theoretical background and principle of operation of the measuring technique, as well as the developed instrumental

configuration, will be discussed. Afterwards, I will report the main results accomplished by performing refractometric experiments on both homogenous and highly scattering media, such as population of cells gently confined in rectangular glass capillaries.

In Chapter 3, the reconfigurable system will be presented in the arrangement set for spectral detection of RI variations. The functionality of rectangular glass capillaries as optical transducers will be discussed and results of numerical simulation based on an analytical model will be presented. Experimental verification of the expected performances will then be proved and documented. Finally, translation of spectral shift into amplitude detection at single-wavelength will be considered for simple detection of RI variations.

In Chapter 4, I will present the activity carried out at the OCN laboratory at Boston University. The low-magnification version of the IRIS system will be demonstrated for the investigation of DNA thermodynamics of nucleotide sequences of interest, as part of a larger project aimed to detecting rare nucleotide mutation for cancer identification.

Appendix A will present the development of an innovative micro-system for generating infrared structured light suitable for 3D imaging. I will describe the optoelectronic configuration, with details on the silicon micro-structures employed as system core elements, that are MEMS micro-mirror and diffractive structures. After testing diffractive elements characterized by different sizes, experimental results about object depth perception obtained with the arranged configuration will be presented.

Chapter **1**

Toward the development of a micro-opto-fluidic chemical sensor: core devices and read-out techniques

In the first part of this dissertation, I will propose a micro-opto-fluidic biochemical sensor for RI detection based on off-the-shelf core elements.

In the following chapter, I will first review the state of the art of optical biosensors for RI measurement. Afterwards, I will present the devices employed as core elements of the propose system and describe the reconfigurable setup employed to perform the optical measurements, which results are presented in Chapter 2 and 3.

1.1. Refractive index optical sensors: state of the art

In this section, the most widely employed optical sensor architectures for RI measurements are introduced and compared on the basis of parameters of merit. In particular, I will focus my attention on optical biosensors working without exogenous markers, i.e. label-free biosensors. Let's first define the parameters most widely employed to describe a sensor performance in the general sensing field.

One of the most employed parameter to describe the performances of a sensor is the sensitivity. Sensitivity is defined as the change of the output signal as a function of a measured sensor property, and thus, in case of linear relationship, is equal to the slope of the transfer function [3]. In the field of biochemical analysis, sensitivity is usually expressed as a function of analyte concentration or of RI. Related to the sensitivity is the LoD, i.e.

the minimum change in the monitored variable (mass, concentration, RI) that can be detected by the sensor over the background signal. The LoD is related to the sensor sensitivity and resolution, where the resolution of the measurement depends on the read-out method and the overall noise [4].

The dynamic range is the maximum interval of the variable under test that can be monitored by the sensor. Other additional aspects that have to be taken into account when developing a biochemical sensor are the sample volume, defined as the minimum quantity of sample that is needed to perform a reliable measurement, the cost of the system and its portability. Cost is an important factor in those fields, such as the biomedical and clinical environment, where disposable elements are preferable in order to reduce cross-contamination of the samples. Small sample volumes are as well usually desirable, creating an increasing interest in the development and use of micrometric devices and of microfluidic systems. In conclusion, we can summarize the desired characteristics of a biosensor with: high sensitivity, low limit of detection, wide dynamic range, portability, low cost, fastness of response (in principle a real-time response is preferable) and good reliability. Based on the transduction mechanism that enables the detection of the parameter of interest, different kind of sensors can be identified: mechanical, electrical, electrochemical, thermal, magnetic and optical.

Among the others, optical detection methods offer many advantages: are intrinsically less invasive, exhibit a fast response, allowing in principle to perform real-time measurements, can achieve high sensitivity values and good accuracy. Optical detection methods can be further divided into two categories: label-based and label-free. Label-based detection exploits marking molecules, such as metal nanorods or beads, plasmonic or magnetic nanoparticles, or, most commonly, fluorescent dyes, that bind to the analyte or chemical that needs to be detected. Bound markers are then usually identified by means of optical microscopy based methods or other kind of imaging systems. Label-based optical sensors can reach very high sensitivity values and low limit of detection, but presents many drawbacks.

First of all, the use of exogenous markers add complexity to the detection protocol, requiring more steps compared to label-free methods, and thus increasing the risk of errors. Moreover, labels are usually costly, and their employment is thus not advisable in realizing low-cost systems. Finally, in label-based methods the possibility of studying biological systems in real-time can be limited by photo-bleaching or photo-toxicity of the fluorescent dyes.

For these reasons, in last decades, an increasing interest have been addressed to label-free detection methods, that are able to measure a parameter under observation with no need of additional markers. The detection method of label-free sensors is usually based on the observation of a change of amplitude, phase, polarization or frequency of the input read-out beam as a consequence of a chemical or physical change of the sample under test.

Recently, increasing attention has been devoted to label-free optical systems sensitive to volumetric changes of RI in fluids. RI sensors are good candidates for the realization of micro-opto-fluidic systems: in fact, extremely small sample quantities are sufficient for an efficient detection, since RI signals scales with the concentration, rather than on the total sample number of molecules. Many different architectures have been proposed, relying on different principles of operation. Between them, photonic crystals, ring resonators, interferometry based sensor, surface plasmon resonance based sensors and slot-waveguides are the most widely used, and a lot of effort has been put by researchers in developing more and more performant platforms. RI biochemical sensor based on the cited structures and methods have been extensively proposed in the literature with many different applications. Let's see what are the principle of operation, the main field of use, the obtained performances and the eventual drawbacks of the various cited architectures.

Surface Plasmon Resonance (SPR) based sensors exploit Surface Plasmon wave (SPW), to perform an efficient detection of RI changes at the interface between two media. In the last decade SPR sensor technologies have been commercialized by several companies, and SPR is still the leading technology for real-time observation of biomolecular bindings. An SPW is an oscillation of the charge density that may occur at the interface between two materials that exhibit dielectric constant of opposite signs. The SPW electromagnetic field can penetrate of about 100 nm in the surrounding media, and the depth of penetration depends on the wavelength and on the dielectric constant of the materials at the interface. The confinement of the SPW field in such a small region results in a high light-matter interaction at the interface, thus leading to a high sensitivity of SPR to events happening close to the surface. Different methods have been implemented to excite the SPR, such as prism coupling, grating coupling, optical fiber coupling or waveguide coupling.

In prism coupling, as the incident light is totally internal reflected by the prism, an evanescent field is generated at the interface between the prism and the lower metal layer. The field penetrates into the conductive layer, and, if the propagation constant of the evanescent field equals that of the SPW, the incident energy is transferred to the SPW itself. This match can happen just for determined incident angles (or wavelengths). As the RI of the media surrounding the metal changes, the resonant angle (or wavelength), consequently changes. SPR sensor based on prism coupling have demonstrated good performances: Lam et al. [5], for example, proposed a prism SPR sensor to monitor glucose concentration in ranges of clinical interest, obtaining LoD around 8.7×10^{-6} RIU.

Another good solution to obtain performant and miniaturized systems is optical fiber coupling: usually a portion of the fiber cladding is removed and the remaining is covered with a metallic layer to enable SPW coupling. More complex solution exploiting optical fibers have been proposed, like

the use of microstructured optical fibers (MOF), or Fiber Bragg Gratings (FBG).

Yang et al. [6], performed simultaneous measurement of temperature and RI with an SPR sensor based on MOF covered with a gold layer, obtaining a sensitivity value for RI sensing higher than 2000 nm/RIU. In [7], Al-Qazwini et al, developed an RI sensor based on SPR in etched plastic optical fibers. Through testing with aqueous solutions with increasing RI, they obtained sensitivities around 1600 nm/RIU. Hu et al. proposed a fiber optic SPR sensor based on a Multimode Fiber-Fiber Bragg Grating-Multimode Fiber (MMF-FBG-MMF) structure, achieving a sensitivity around 2500 nm/RIU and LoD better than $2x10^{-7}$ RIU [8]. Zhang et al. investigate the performances of a U-bent optical fiber decorated with gold nano-particles and covered with graphene, obtaining sensitivity values around 1200 nm/RIU [9]. Lei et al. obtained a maximum sensitivity of 628 nm/RIU and a LoD around $7x10^{-6}$ RIU employing a second order distributed feedback SPR cavity on a Single Mode Fiber (SMF) end facet [10]. Another alternative to achieve an efficient SPW coupling lie in the use of optical waveguides. In this case, metal is deposited on the waveguide, and as the light travels through it, an evanescent field is generated at the metal-waveguide interface. Waveguide coupling offers different advantages, such as the chance of creating miniaturized, integrated and multiplexed systems just by fabricating multiple sensors on a single chip. Dostálek et al. built an SPR sensor exploiting waveguide coupling capable of measuring bulk RI changes smaller than 1.2×10^{-6} RI [11], while in [12], a LoD equal to $2.3x10^{-5}$ RIU was demonstrated for an optical waveguide SPR sensor exploiting dual emitting diodes. The last coupling alternative relies on the use of gratings. The read-out light beam is shined on a metallic grating: if the momentum of the light diffracted parallel to the grating surface equals the SPW propagation constant, light is coupled in the SPW. Grating couplers offer the advantages of be mass produced, leading to a low-cost of production for a single element.

Another important class of label-free optical biosensors are those exploiting interferometry. Between other RI optical sensors, interferometry based ones have been demonstrated to reach the best performances in terms of limit of detection, with impressive LoD values, as low as 10^{-9} RIU [13]. Interferometric biosensor can be realized in a large variety of materials, mostly developed through microelectronic fabrication technique or starting from commercial products [14], as, for example, optical fibers [15]. Several different architectures have been proposed in the literature, based on Young interferometers, Mach-Zehnder interferometers (MZI), Michelson interferometers (MI), bimodal interferometers and Fabry-Pérot interferometers.

In a MZI, radiation from a read-out source is split in two branches, the reference one, and the measuring one, that is sensitive to external RI changes. Light coming from the two paths is then recombined and the output intensity is detected. As a RI change occurs in the media

surrounding the measuring path, light travelling through it undergoes a phase shift, thus resulting in a change of the output signal. MZI based biosensors have been developed employing various materials, such as polymers or glass [16], [17], and, more often, silicon nitride (Si_3N_4) and silicon oxynitride (SiON) waveguides on silicon substrates [18]–[21]. Several sensors based on MZI can be found in the literature: in [22], for example, Gao et al. proposed a biochemical sensor based on the combination of a nanoplasmonic structure and the MZI architecture, reaching sensitivities higher than 3500 nm/RIU and LoD around 1.5×10^{-5} RIU. Liu et al. [19] demonstrated the functionality of a MZI biosensor based on a silicon nitride waveguide and a strip waveguide fabricated through standard complementary metal–oxide–semiconductor (CMOS) processes. The device was tested with an amplified spontaneous emission (ASE) source emitting around 1550 nm for increasing concentration of NaCl solutions, obtaining LoD of the order of 10^{-6} RIU and sensitivity around 1970 nm/RIU. A MZI optical fiber biosensor was proposed in [23], where Mach-Zehnder interference was induced into a micro-cavity fabricated by means of femtosecond laser micromachining and chemical etching within a single-mode fiber. Through testing with BSA solutions and a broad-band light source, a detection limit of 3.5×10^{-5} RIU was obtained.

Another class of interferometers are those relying on the Michelson configuration. In a standard MI, read-out light is redirected by a beam-splitter on two difference path, the reference and the sensing one. Light is then back-reflected by two reflective elements at the end of both paths and recombined at the beam-splitter and finally detected by a monitoring system. Thus, on the contrary to Mach-Zehnder interferometers, light travels each path twice. If light encounters different media on the two arms, or paths of different length, a phase difference is accumulated, that can provide information about the difference in RI or length on the two arms.

MIs have been combined with broadband light sources or single wavelength sources. When exploiting laser sources, the Michelson configuration is usually employed to detect sub-wavelength vibration or displacement, while broad-band MIs allow to reconstruct the RI profile of the tested samples, such as in OCT [24].

Exploiting broadband read-out sources in the near infrared, Zhang et al. [25] proposed a fiber optic MI exploiting a SMF as reference arm and a section of high birefringence fiber serving both as sensing arm and probe for simultaneous sensing of RI and temperature. Zhou et al. [26], as well, proposed an optical fiber MI for RI sensing fabricated by splicing a section of a thin core fiber to a standard SMF with a core offset, obtaining a measurement resolution of 4.9×10^{-6} RIU. In [27], a LoD equal to 5.1×10^{-4} RIU was obtained creating a single symmetrically abrupt taper region in a short piece of single-mode fiber terminated by 500 nm thick gold coating and employing a broad-band source emitting in the range of 1530-1600 nm.

In Young interferometers, the read-out beam from a laser source is divided through a Y-junction in two different arms, one of which is sensitive to external RI changes. Differently from the MZI, the two arms don't recombine but the optical output signal form interference fringes on a detector, such as a Charge-Coupled Device (CCD) sensor. Phase shift is then usually detected by means of Fourier Transform based methods. Ahmadi et al. obtained a resolution of $1x10^{-6}$ RIU using a slot waveguide Young interferometer realized in polymeric materials [28], while in [29] SiON technology was employed to develop an integrated biosensor based on a Young configuration, reaching LoD around $6x10^{-8}$ RIU. Schmitt et al. [30] obtained a LoD value as low as $9x10^{-9}$ with a Young interferometer configuration based on commercial planar Ta_2O_5 waveguides investigated with a superluminescent diode emitting at $\lambda = 675$ nm.

A more recent class of interferometric biosensors relies on bimodal interferometry [14]. In a bimodal interferometer, the interference occurs between the fundamental and the first mode of monochromatic light propagating into a single planar waveguide. In particular, light from a coherent source is coupled (usually by means of a grating) in the straight waveguide that, in its first part, supports just the fundamental mode. Then, after a determined distance, the waveguide is differently shaped in order to support the first-mode as well. First-order mode and fundamental mode interfere between each other, and travel till the end of the waveguide. The interferogram is then recorded by means of an external photodetector. The simplicity of the design is thus a strength of this kind of interferometers: no reference path is needed, a factor particularly interesting in view of the realization of miniaturized systems. The sensing area is located on the bimodal part of the waveguide. A variation of RI in the sensing area causes a variation of the difference in phase between the two supported modes, resulting in a variation of the monitored intensity at the output detector. Duval et al. [31] proposed a lab-on-a-chip platform provided with 16 different bimodal interferometers fabricated by standard silicon process integrated with sub-wavelength gratings for light coupling. A 3D polymeric microfluidic network was as well included. Employing a laser source emitting at $\lambda \sim 658$ nm, they obtained a bulk RI LoD equal to $3.3x10^{-7}$ RIU. Zanoviev et al. reported a LoD of $2.5x10^{-7}$ using as well a bimodal interferometer fabricated by standard silicon process and a He-Ne laser source ($\lambda \sim 633$ nm). They further test the applicability of the sensor as label-free biosensor by the real-time monitoring of the biomolecular interaction of BSA and antiBSA [32].

Fabry-Pérot interferometers based RI sensors have been as well proposed. A Fabry-Pérot interferometer (FPI), or Fabry-Pérot etalon, further discussed in Chapter 3, is a device composed by two parallel highly reflective surfaces, divided by a gap. As a read-out beam is shined on one of its surface, interference will occur between beams reflected (and transmitted) multiple times at each RI interface. As the RI of the crossed

media is changed, light undergoes a phase shift proportional to the RI variation. Liu et al. [33] proposed a FPI cavity fabricated into an SMF with two open faces by femtosecond-laser induced water breakdown. The cavity had a dimension of 60 μm x 50 μm. Employing a wide spectrum light source (1200-1700 nm), they obtained a sensitivity S = 1147.48 nm/RIU and an actual LoD = 1.29×10^{-4} RIU. In [34], a FPI cavity was machined in a SMF and covered with gold layers of various thickness, in order to create a semi-transparent mirror on one side and a total-reflection mirror on the opposite one. Since light reflections of gold thin films are not affected by the RI of the various measuring media, gold deposition allows to overcome the problem of poor sensor performances usually occurring when the RI of the tested media is close to that of the optical fiber, as predicted by Fresnel laws. Employing a tunable laser continuously swept from 1530 to 1570, sensitivity around 1160 nm/RIU and RI resolution better than 1×10^{-6} RIU were found. Wu et al. [35] reached a maximum sensitivity S=1360 nm/RIU at the wavelength of 1600 nm employing a FPI fabricated by splicing a thin piece of C-shaped fiber between two standard SMF. A LoD of 7.2×10^{-5} is reported.

Another class of RI sensors relies on photonic crystals. Photonic crystals (PhC) are micro or nanostructures realized in dielectric materials arranged in a periodic configuration and with a high RI contrast. PhC are characterized by the presence of a photonic bandgap (PBG), and periodicity of the wavelength order. PhC exist in one-dimensional (1D), two-dimensional (2D) and 3D structures, depending on along which direction the dielectric constant varies. Given their particular structure, only determined wavelength of the incident light can propagate through the structure, while for wavelength within the PBG the PhC behaves like a mirror. Around the bandgap wavelength, the transmitted spectrum presents thus a low transmissivity region, corresponding to high reflectivity values in the reflected spectrum.

As the RI along the structure changes, for example as a consequence of biomolecules binding to the PhC internal walls, the peak position in wavelength is changed. In this way, a PhC behaves like an optical transducer, allowing to detect local bulk RI changes or molecular binding. Thanks to the high potential sensitivity, photonic crystals have been widely proposed as chemical or biochemical sensors. Surdo et al. [36] proposed a vertical one-dimensional silicon photonic crystal operating in the near-infrared, obtaining maximum sensitivity S=2510 nm/RIU and LoD=2×10^{-6} RIU though testing with BSA solutions. PhCs were fabricated by electrochemical micromachining (ECM) technology and provided with reservoirs, allowing self-powered capillary filling of the device. Mandal et al. [37] developed a Nanoscale Optofluidic Sensor Arrays (NOSAs) to perform highly parallel detection of biomolecular interaction in aqueous environments. 1D photonic crystals with different cavity spacing were employed and evanescently coupled to a single bus waveguide, obtaining a

11

RI detection limit of $7x10^{-5}$ RIU. A similar structure was proposed in [38] , and experimental results lead to LoD=$8.65x10^{-5}$ and sensitivity S=115.60 nm/RIU.

Wang et al. [39] designed a liquid RI sensor based on 2D structure composed of silicon-rods arranged to form a photonic quasicrystal structure, obtaining a sensitivity S = 221 nm/RIU and sensing accuracy of 10^{-4} RIU. A 3D photonic crystal RI sensor, based on a void channel photonic crystal fabricated by femtosecond laser writing in a polymer substrate, was developed by Wu et al. [40]. With this structure, they were able to detect RI changes of $6x10^{-3}$ RIU.

Another interesting solution for RI sensing is represented by fiber-optic sensors, in particular Fiber Bragg Grating (FBG) and Long-period Fiber Gratings (LPFG). In a FBG sensor, the external part of the fiber or its core is permanently altered introducing a periodic variation of the RI along one dimension. Depending on the periodicity of the structure, if broadband light is launched in fiber, just a specific wavelength, called the Bragg wavelength, is back-reflected by a FBG, while the remaining are transmitted. By monitoring the shift of the Bragg wavelength, FBG can be employed as temperature, strain or bending sensor. Beside these standard applications, FBG find also use as label-free refractometric sensors. In optical fibers light is strongly confined in the core by total internal reflection; in order to expose the evanescent field and make the sensor sensitive to external RI changes, a surface grating can be realized on the side of the fiber, or the fiber can be chemically etched down to the core. For example, in [41], Chryssis et al. reached LoD as low as 7.2×10^{-6} RIU and sensitivity S = 1394 nm/RIU by etching the cladding and part of the core of an FBG sensor and monitoring the RI change in the surrounding media. In a similar fashion, Schroeder et al. [42] developed a FBG refractometer by partially removing the fiber cladding through side polishing technology obtaining a minimum LoD of 2×10^{-5} RIU for RI values around 1.45 RIU. Huy et al. [43] reached a detection limit of $6x10^{-6}$ RIU photowriting a FBG in a three hole MOF.

A second class of refractometric fiber optic sensors employs long-period fiber gratings. These gratings exhibit a periodicity of three or four order of magnitude higher than standard FBG, usually in the range of 100 µm to 1 mm. This particular structure leads to a stronger coupling of the core mode into the cladding modes. The more intense field confinement in the fiber cladding result in a higher sensitivity of LPFG to the surrounding media RI changes. Sun et al. [44] developed an hybrid structure composed by a LPG and a chirped fiber Bragg grating (CFBG). A CFBG is a Bragg grating in which the grating RI profile has been modified, for example introducing a linear variation in the grating period (i.e. a chirp). In a CFBG the chirped grating reflects the impinging light introducing different delays for different wavelengths. Both gratings were written into a hydrogenated telecom Single Mode Fiber (SMF). With this structure, they obtained a highest RI resolution around $5.6x10^{-6}$ RIU in the RI range between 1.36

and 1.43 RIU. Good results were obtained even for lower RI values
(1.00-1.36 RIU) with detection limit of 3.4×10^{-5} RIU.

In conclusion, fiber based RI sensors offer various advantages, like high
sensitivity, small size, multiplexing capabilities, high accuracy, acceptable
cost and possibility of performing the measurement also on large distances
and in harsh environments [45]. However, they perform sufficiently good
just on a limited RI region and are strongly subject to temperature and
strain influences, making usually necessary to introduce an additional fiber
gratings or to develop hybrid complex structures to monitor the reference
wavelength.

Another class of optical biosensors extensively proposed in the literature
are those based on slot waveguides. Slot waveguides are optical
waveguides that exploit total internal reflection to confine a light beam in a
slot region with sub-wavelength dimension and low RI. The slot region is
delimited by two slabs realized in a high-RI material and the whole
structure is surrounded by a low RI cladding. This typical structure results
in a strong confinement of light in the slot region, thus allowing strong
light-analyte interaction. As a sample interacts with the guided read-out
beam, light undergoes a phase shift. Slot-waveguides based biosensors
present the advantage of being suitable for miniaturization and
consequently integration with micro-fluidic systems and electronics
components in a single chip [46]. Slot-waveguides sensors can be used both
to monitor RI change in bulk solutions or to detect biomolecules in a
sample. Different architectures have been investigated, mainly based on
interferometric configurations, like Mach-Zehnder interferometers [47] and
directional couplers [48] or on micro-resonators [49]–[51]. Through a
Mach-Zehnder configuration LoD around 10^{-5} RIU were obtained [47],
while Di Falco et al. obtained LoD equal to 7.8×10^{-6} RIU and sensitivity
values around 1500 nm/RIU employing a slotted photonic crystal cavity
[52]. Concerning the constituent materials, combinations of Si_3N_4/SiO_2 and
Si/SiO_2 are the most widely employed. Recently, Ahmadi et al. [28]
proposed a polymer slot waveguide Young interferometer coated with a
bilayer of Al_2O_3/TiO_2 detecting a RI change of 1×10^{-6} RIU.

All the classes of presented optical resonators exhibit with no doubt
many advantages, including high sensitivity and specificity. However, in
planar waveguide based optical sensors, to reach satisfying values of
sensitivities a long optical path is required: in label free sensing in fact, a
great impact on the sensitivity is given by the amount of light matter
interaction. A solution to this limitation comes from ring resonators. Ring
resonators are composed by a dielectric material shaped in circular
structures and by a straight waveguide strongly coupled to the ring, in
which the read-out beam propagates into. In ring resonator, the strength of
light-analyte interaction depends by the number of revolutions of light into
the ring structure, and no longer by the sensor physical size itself, like

happens in planar resonators. For this reason, ultra-miniaturized system can be realized without sacrificing the sensor performances.

In ring resonators, the circular track may sustain the Whispering Gallery Modes (WGM) [53], i.e. specific modes of a wave field propagating along a curved cavity and characterized by low reflection losses [13]. The existence of WGMs relies on total internal reflection at the external interface. An evanescent field is created outside the ring resonator, sensitive to the change of RI in the surrounding media or to the binding of molecules. Due to their particular structure, a strong light-analyte interaction is obtained, with no need of increasing the physical dimension of the devices. Thus, high sensitive sensors can be created in a miniaturized format, that can be easily integrated with microfluidic systems and electronic components. Kim et al. [54] developed an integrated photonic glucose biosensor exploiting a vertically coupled micro-ring resonator in polymeric waveguides, obtaining sensitivities around 200 nm/RIU and detection limit equal to $5x10^{-6}$. In [55], the functionality of a sensor realized with silicon nitride (Si_3N_4) guides on silicon oxide was demonstrated. Two ring resonators were employed, one used as sensing resonator, and one as reference resonator. Detecting the sensing ring resonance position with respect to the reference one for increasing concentrations of sucrose in solution, a LoD equal to $5x10^{-6}$ RIU was obtained. Similar detection limits and a sensitivity equal to 2169 nm/RIU were obtained in [56], employing two cascaded ring resonators and exploiting the Vernier effect. Barrios et al. [57] proposed an integrated biochemical sensor based on a micro-ring resonator structure employing slot waveguides fabricated in Si_3N_4-SiO_2, obtaining sensitivities equal to 212 nm/RIU and the LoD equal to $2x10^{-4}$ RIU.

An alternative to standard ring resonators are liquid-core optical ring-resonators (LCORR). In LCORR the WGMs are excited in a hollow circular structure, like the walls of a round capillary. The fluid to be tested flows inside the capillary channel, and, as the WGMs penetrates into the internal part of the device, the sensing is performed. LOCCR sensors have been tested in the field of chemical analysis demonstrating good efficiency. In [58], Sumetsky et al. proposed a LOCCR sensor composed by a segment of a capillary fiber coupled to a microfiber and immersed into a cured low-index medium. Launching broadband radiation into the microfiber and monitoring the transmitted spectrum as solution at increasing RI were flowing into the capillary channel, they obtained sensitivities around 800 nm/RIU. In [59] a round capillary coupled with a tapered fiber was investigated, and label free RI detection was performed obtaining a limit of detection of $2.8 x 10^{-7}$ RIU.

In conclusion, a lot of attention and effort have been put in the last decades in developing more and more performant sensors. Moreover, with the integration of optics and fluidics, systems have been rapidly moving from bulky devices to micro-opto-fluidic systems. Despite the listed

achievements, there is still need of demonstrating the use of low-cost commercially available devices as core elements of micro-opto-fluidic system for chemical and biochemical sensing. In fact, most of the sensors proposed in the literature, and that have been previously reported, employ devices obtained with micro-machining techniques or that anyway require costly procedure in order to make them suitable for sensing purposes. This need results in expensive sensing systems, with cost reducible just in case of mass production. Additionally, some of the presented measuring techniques require complex read-out systems that need to enter in contact with the sensor when performing the measurement, or even worst, with the sample itself. On the contrary, in the system we are proposing, the measurement is performed in a remote way, thus with minimum invasiveness for the sensor and the sample.

In the following sections, I will investigate the use of off-the-shelf disposable devices for the development of a micro-opto-fluidic system for biochemical sensing, with the aim of demonstrating the possibility of developing a compact and portable system for volumetric RI detection. Here, I will now present the tested devices and the instrumental configuration employed to perform RI detection.

1.2. Micro-fluidic disposable devices for refractometric measurements

In order to realize a flow-through chemical sensor, two different kind of micro-fluidic devices were tested: rectangular micro-capillaries, realized in Borosilicate glass, and a polymeric device commercialized by IBIDI™, the IBIDI™ μ-Slide VI$^{0.1}$. Both kind of devices are commercially available at low-cost, allow to work with low-quantities of material, can be easily integrated into a fluidic external system, and are realized in materials with good optical qualities: these characteristics make them perfect candidates for the realization of a low-cost micro-fluidic optical sensor. Let's see in more detail the characteristics of each employed device.

Rectangular glass micro-capillaries are off-the-shelf disposable devices available in a wide range of dimensions. A 3D representation of the device is shown in Figure 1.1, where t_f is the front-wall thickness, t_b the back-wall thickness and d the channel depth, while W represents the capillary width and h its height. Capillaries with h = 50, 100, 300, 600 mm are available, while different combinations of walls thicknesses and channel depth are offered, with dimensions in the range from 20 to 400 µm. The capillary width W is usually of one order of amplitude bigger with respect to the channel depth. The manufacturer ensures a tolerance of 10% for the channel depth d and the capillary width W and of 20% for the walls thickness. Rectangular glass micro-capillaries are realized in Borosilicate glass 3.3, a material offering good optical qualities and easy functionalization. Moreover, the flat surface allows the sample

observations under microscope at various magnifications, and is in general perfectly suitable for any optical analysis, reducing those scattering phenomena usually occurring when dealing with regular round cross-section capillaries [60]. Additionally, the internal micrometric dimensions of the device allow to work with ultra-low quantities of materials, important factor in the field of biological analysis, where often very small quantities of samples are accessible. In biological and biochemical applications, miniaturization of analytical systems would additionally allow to reduce the response time, improve process control, and realize portable instruments [61]. Another advantage relies in the fact that the major part of samples fills the capillaries just by capillary action, with no need of an external aid.
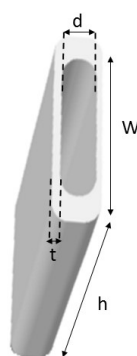
Figure 1.1 3D sketch of a rectangular glass micro-capillary; W = capillary width, t = wall thickness, d = channel depth, h = capillary height.

Thanks to presented advantages and to their versatilities, in the past years, glass micro-capillaries have been used in different fields and applications. For example, they have been widely applied in the field of biological analysis, like the observation of microorganisms in their natural environment [62]. Recently, rectangular glass micro-capillaries were successfully proposed as acoustic resonators for particles and cells trapping using standing wave [63] [64]. Hammarstrom et al. [63], [65], for instance, applied acoustic wave trapping in glass flat capillaries to confine and dispense red blood cells from diluted blood. In this field, this kind of devices offers the advantage of low-cost together with the low acoustic losses and good mechanical properties of glass. Morrish et al [66] employed round mirrored glass capillaries to perform optical detection of fluids and gases flowing inside the channel. Previous work investigated rectangular glass capillaries for capillary zone electrophoresis to obtain high resolution separations in the analysis of complex mixture [67]. Moreover, as stated before, rectangular glass micro-capillaries are of great interest in various micro-opto-fluidic systems where optical imaging or spot measurements need to be performed.

Beside all the listed advantages, a problem we had to face dealing with rectangular micro-capillaries, was to provide a good interlacement between the devices and the external fluidic system.

In fact, despite micro-fluidic devices are nowadays widely diffused in many applications, the connection of miniaturized systems with the external world remains still challenging [64] [68]. Actually, all commercially available connections for the interlacement with the fluidic systems are designed just for round section micro-capillaries. The chance of combining rectangular capillaries with advanced fluidic system, could potentially help to move already existing platform to disposable devices [64]. Fluidic interfaces need to be easy to be assembled, producible at low-costs, be biocompatible and compatible with standard tubing and fluidic components. Moreover, rectangular glass-micro capillaries, given their fragility, need to be protected along all their length.

To answer to the listed requirements and allow an easy integration with the experimental setup, a custom polymeric support was designed. The device was created in collaboration with the β-lab of the Department of Civil Engineering of the University of Pavia, under the supervision of Prof. Auricchio. The support was designed with a CAD software (SolidWorks® - Dassault Systèmes) and realized through 3D printing technology.
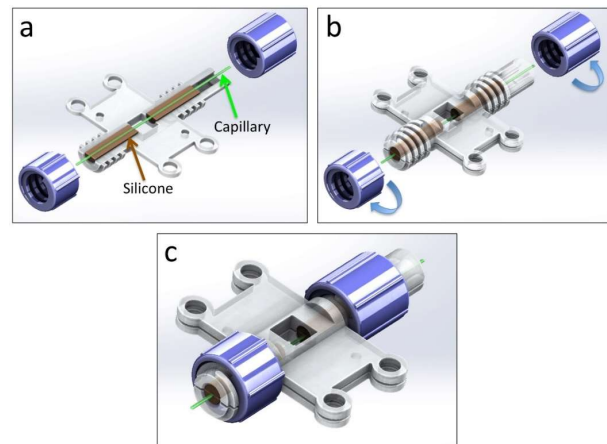
Figure 1.2 Reconstruction of the 3D printed polymeric support holding a rectangular glass micro-capillary.

As can be seen in Figure 1.2, the supporting device is composed by four parts to be assembled. Two symmetric halves compose the main structure and hold the capillary in their central semicircular channel. Given the fragility and the narrow section of the micro-capillary, four silicon bearings are placed in the inner channel of the support to protect the micro-capillary from being damaged by the contact with the rigid walls (Figure 1.2 a). Two threatened caps of different length fasten the main structure (Figure 1.2 b); in particular, the shortest one allows the fluidic feeding of the capillary, while the longer one simplify the connection with the external fluidic

system. Two rectangular handles with four holes each enable to fix the whole device (Figure 1.2 c) to the experimental setup. A window placed in the middle of the structure ensures a clear path for the read-out optical beam. The four parts were exported as Standard Triangulation Language (STL) format and 25 μm thick layers in methacrylate photopolymer resin (FLGPCL03) were printed using a Form2 (Formlabs) printer, based on stereolithographic technology. The bearings, instead, were created using a 3D printed mold in which to pour a bi-component silicon mixture (Sylgard 184 – Dow Corning).

Let's know present the second kind of device, i.e. a polymeric micro-fluidic slide commercialized by IBIDI™. Between the wide range of commercialized devices, the IBIDI™ *μ-Slide* VI$^{0.1}$ resulted well suited for our purposes, a picture of which is shown in Figure 1.3. The device is composed by six parallel channels with length equal to 17 mm, width of 1 mm, and depth of 100 μm. The total internal volume of each channel is approximately equal to 1.7 μl. Again, the small internal dimensions allow to deal with small quantities of sample. Each channel ends at both sides with standard luer connections, enabling an easy and efficient interconnection with the external fluidic system. Samples can be introduced in the channels just by means of a syringe or a micropipette or can be integrated in a more sophisticated fluidic system able to reproduce specific flow conditions. The slide is realized in polymeric materials with excellent optical properties, comparable to that of glass [69]. Moreover, the thin front wall thickness, equal to 180 μm, allows an easy optical read-out of the materials inside the channels.
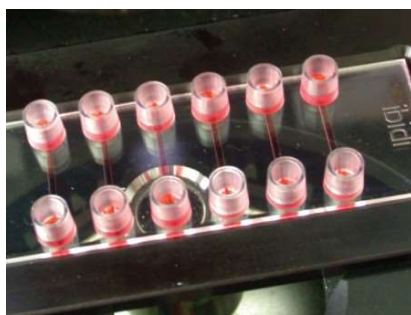
Figure 1.3 Photo of an IBIDI™ VI$^{0.1}$ μ-Slide with six 100-μm-deep channels and Luer terminations for fluidic interconnection.

IBIDI™ disposable devices are widely used in the biological and biomedical field. IBIDI™ μm-slide can be for example employed for cell culture under flow, cell based microscopy, live cell imaging, chemotaxis and angiogenesis studies, also thanks to their good optical properties. Liebl et al., for example, made use IBIDI™ μ-Slide chemotaxis to investigate the impact of cyclin-dependent kinase-5 on umbilical vein endothelial cells

(HUVEC) migration and angiogenesis [70]. Ganguly et al. investigated the processes involved in neutrophil transmigration observing their interaction with HUVEC cells grown and stimulated into a µ-slide [71]. In [72], Ashpole et al. employed IBIDI™ chambers to seed Schlemm's canal cells from human and glaucomatous patients to analyze the effect of shear stress on the nitride oxide production. In general, IBIDI™ micro-fluidic devices are perfectly suitable in all those situations in which determinate flow conditions are required, offering the additional advantage of an easy optical read-out, thanks to the good polymer optical quality and to their flat surface.

1.3. Reconfigurable instrumental configuration for remote optical measurements

As stated before, the developed sensor is based on the optical detection of the RI of fluids inserted into micro-fluidic disposable devices. Two main read-out techniques were employed, both based on broadband near-infrared radiation: low-coherence interferometry and spectral detection. Briefly, spectral detection is based on the detection of the reflected and transmitted optical power through the device under test as a function of the wavelength for RI variation. On the other side low-coherence interferometry allows the reconstruction of the RI profile of the device along the direction of the read-out beam. The two measuring techniques require different instrumental configurations, but we developed an easily reconfigurable all-fiber setup that allows to perform both kind of measurements starting from the same basic instrumental configuration, that can be adapted performing some minor changes.

Figure 1.4 shows the block diagram of the reconfigurable setup employed for both low-coherence interferometry and spectral detection. The experimental configurations employed for each kind of measuring technique can be easily obtained from the common setup with small changes, and will be described in more detail in paragraph 2.2 and paragraph 3.2. Briefly, radiation from a broad-band light source is coupled in standard telecommunication optical fiber and split by a 2x2 fiber optical coupler with 50:50 splitting ratio on two different paths. When performing interferometric measurements, the light travels through a second coupler (not shown in the picture) and is redirected on two different paths, one ending with a reference mirror and the second with the device under test. Reflected radiation is coupled back in fiber through aspheric lenses and finally reaches a photodetector. In case of spectral measurements, the mirror is tilted to avoid any back reflection, and thus the optical power reaching the photodetector comes just from the back reflection due to the device. An additional difference between the two instrumental configuration schemes regards the activation of an additional fiber optic path when performing spectral measurements, represented in Figure 1.4

with a black dotted trace. This second path is as well connected to the photodetector and allows the collection of the optical power transmitted across the device.
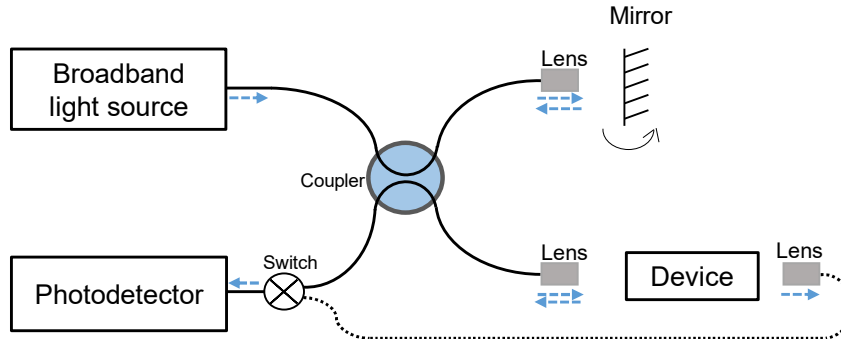
Figure 1.4 Block diagram of the reconfigurable setup employed for low-coherence and spectral measurements. The fiber optic dotted path is activated just in case of spectral measurements, to detect the optical power transmitted by the device.

A switch allows in principle to commute between the reflection and transmission spectra to be acquired by the photodetector. The use of connectorized optical fibers ensures high flexibility and rapid switching between the two configurations. Low-coherence interferometry and spectral detection require different photodetectors in order to reconstruct the collected signals. All employed read-out sources are characterized by a broadband emission spectrum in the near-infrared, thus in a wavelength region of minimum invasiveness for the biological tissues. In particular, a Tungsten lamp was used for high resolution interferometric measurements, while ASE sources were employed for spectral measurements. In particular, we exploited two SLEDs, one with central wavelength emission λ_c at approximately 1.3 µm and one with λ_c at about 1.55 µm. With respect to the Tungsten lamp, the SLEDs provides a narrower emission spectrum but higher power coupled into fibers. For preliminary alignment of the read-out beam to the device a source emitting in the red, i.e., the He-Ne laser with λ_c=632.8 nm, was employed. Regarding the photodetectors, two photodiodes incorporated in a balanced receiver are used for performing interferometric measurements. The balanced receiver enables the efficient detection of the interferometric signal, doubling the interferometric contribution and removing DC components and other common mode signals. On the other side, an Optical Spectrum Analyzer (OSA) is necessary when performing spectral measurements, allowing to reconstruct the signal on a wide wavelength interval. Another difference between the two configurations is represented by the activation of a second fiber optic path when performing spectral measurements, devoted to the collection of the optical power transmitted through the tested device. As mentioned, in

this case the reference mirror is tilted to avoid any back reflection. Reflected and transmitted optical spectra are then acquired through a Personal Computer (PC), thanks to a GPIB connection. After acquisition, the ratio between transmissivity and reflectivity is calculated, in order to compensate for spurious source fluctuation. During the experiments, the microfluidic devices are integrated in a fluidic system for samples collection and elimination. The polymeric IBIDI™ μ-slide offers standard luer connections and can be thus easily interfaced to the external fluidic path. A peristaltic pump is used to collect and discard the tested sample. When dealing with the rectangular glass micro-capillaries, on the other side, the capillary force is sufficient to provide the device filling, while the peristaltic pump is used just to force fluid out of the capillaries.

Chapter **2**

Sensor optical read-out by means of low-coherence interferometry

This chapter is dedicated to low-coherence interferometry. First of all, the theory related to the Michelson interferometer scheme is discussed. Then, I will describe in detail the specific instrumental configuration employed to perform the measurements. Finally, I will present the experimental results reached in detecting the RI of various fluids inserted in the IBIDI™ μ-slide and in rectangular glass capillaries. Presented results were published in [73] [74] [75] [76].

2.1. Introduction to interferometry

Interferometry is a well-known technique relying on the principle of interference of light, a physical phenomenon easy explainable through the wave theory of light: as two coherent light waves (in space and time) at the same frequency interact, the result is a wave with possible amplitude values between a maximum given by the sum of the amplitude of the two original waves and a minimum equal to zero. If the first case is occurring, the interference is called completely constructive, otherwise completely destructive. Interferometric techniques allow to perform measurements of wavelengths, distances, and displacements. Interferometry was already known at the beginning of the 19th century, but it is in 1965, with the birth of the first lasers, that interferometric techniques undergo a great development, allowing the spread of a new class of instruments able to measure vibrations and displacement with sub-micrometric resolution [2]. Low-coherence interferometry, on the other side, make use of broad-band light sources to perform measurements of relative distances, or better, relative optical paths. Different interferometer architectures have been developed and applied in various field, such as Mach-Zehnder, Young,

Fabry-Pérot and bimodal interferometers [22], [28], [31], [77]–[84]. In our work, we applied a Michelson interferometer scheme to perform low-coherence interferometric measurements. The free space configuration of a Michelson interferometer is reported in Figure 2.1.
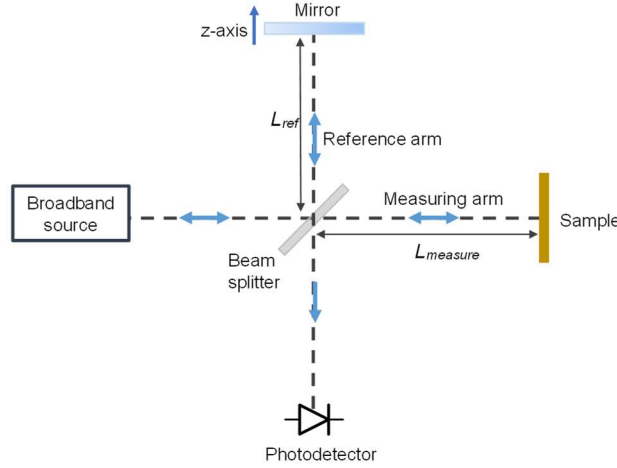
Figure 2.1 Block diagram of a low-coherence Michelson interferometer, with light propagating in free space.

Briefly, read-out radiation from a broadband light source is redirected by a beam-splitter toward two different paths: the reference path, with length L_{ref}, ending with a mirror, and the measuring path, of length $L_{measure}$, ending with the sample under test. $L_{measure}$ and L_{ref} are distances expressed in terms of optical paths, where the optical path (OP) is defined as the product between the geometrical distance and the group RI of the crossed medium. Radiation reflected by the mirror and by the sample overlaps at the beam-splitter, and is split again back toward the source and toward a single element photodetector, such as a photodiode. The interference between the two field depends on the difference in terms of optical length between the two travelled paths, and thus on the accumulated difference in phase between the two optical fields. If the spatial coherence between the waves is guaranteed, the current generated by the photodetector is proportional to the square of the modulus of the impinging electromagnetic radiation and the interferometric signal is mathematically due to the cross-product between the two fields. Given E_{ref} the electromagnetic field reflected by the mirror, and $E_{measure}$ the one reflected by the sample, we have:

$$E_{ref} = E_0 e^{[j(wt+2kL_{ref})]} \tag{1}$$

$$E_{measure} = E_0 e^{[j(wt+2kL_{measure})]} \tag{2}$$

where E_0 is the electromagnetic field in vacuum, $\omega=2\pi v$ the pulsation, with $v=c/\lambda$ the optical frequency, t is the time and k the wavevector

modulus. The current generated by the photodetector, assuming the beam splitter with a power splitting ratio of 0.5, results equal to

$$I_{PH} = I_0 R_{ref} + I_0 R_{measure} + 2I_0 r_{ref} r_{measure} |G(\tau)| \cos(\omega\tau + \emptyset) \qquad (3)$$

where I_0 is the current due to the square of the electromagnetic field propagating across the reference path if the mirror is an ideal reflector. R_{ref} and $R_{measure}$ are the reflectances, i.e. the reflection coefficient for the optical powers, while r_{ref} and $r_{measure}$ are the reflection coefficients for the optical fields. τ is the delay between the waves that have travelled along different paths and $\emptyset = (\frac{2\pi}{\lambda}) 2ndcos\theta$ is the phase delay, where *n*d* represents the optical path seen by the light. The first two terms of Eq.3 represents the DC component of the signal, while the effective interferometric component is given by the last term, characterized by the term cos ($\omega\tau$), that describes the development of the interferometric fringes for varying τ. $G(\tau)$ is the autocorrelation function or *fringe visibility* and ω is the optical pulsation. As the delay τ changes, interferometric fringes are developed, each one corresponding to a change of optical path equal to $\lambda_c/2$, where λ_c is the central emission wavelength of the read-out source. The autocorrelation function is related to the source emission spectrum and, by multiplying the cosine term, modules the amplitude of the generated interferometric fringes. The mathematical expression of the autocorrelation function, according to the Wiener-Khinchin theorem, is related to the power spectral density of the source $S(v)$ through Fourier transform, and is mathematically defined as

$$G(\tau) = \int_0^\infty S(v)e^{-j2\pi\tau} dv \qquad (4)$$

Considering the case of Gaussian emission spectrum of the source, the power spectral density results equal to

$$S(\lambda) = \frac{2\Delta\lambda\sqrt{\frac{ln2}{\pi}}}{c} e^{-4ln2\left(-\frac{\Delta\lambda^2}{\lambda_0\lambda}\right)^2} \qquad (5)$$

here expressed in the wavelength domain, in practical interferometric measurements usually preferred to the optical frequency domain. Consequently, the autocorrelation function can be easily found equal to

$$G(\tau) = e^{-\left(\frac{\pi c\tau}{2\Delta\lambda\sqrt{ln2}}\right)^2} e^{-j2\pi\frac{c}{\lambda_0}\tau} \qquad (6)$$

where $\Delta\lambda$ is the width of the source emission spectrum in the wavelength domain. An important parameter of a light source is its coherence length L_c, that is equal to the difference between the measuring and reference path that halves the amplitude of the interferometric fringes. It can be calculated as:

$$L_c = \frac{2cln2}{\pi n} * \frac{1}{\Delta v} = = \frac{2ln2}{\pi n} * \frac{\lambda_0^2}{\Delta \lambda} \sim 0.44 \frac{\lambda_0^2}{\Delta \lambda} \qquad (7)$$

where n is the RI of the medium in which the light is travelling and the final approximation is calculated for n~1 (air). As the reference mirror position is fixed, the delay τ between the optical fields that have travelled the reference and measuring path is constant in time, and consequently no interferometric fringes are detected. Indeed, if the mirror is moved with a constant reference speed v_{ref}, the temporal delay between the optical fields varies as a function of time, following the relation

$$\tau(t) = 2\left(\frac{\Delta z}{c}\right) = 2\left(\frac{v_{ref}t - z_0}{c}\right) \qquad (8)$$

where z_0 is the initial position of the reference mirror and $v_{ref}t$ represents the mirror displacement in a time t. The multiplying coefficient equal to 2 derives by the fact that the light travels two times each path, first to reach the mirror and the sample and then when is back-reflected to reach the photodetector. From the mathematical expression of τ is possible to derive the optical path difference as a function of the delay, as $\Delta z = c\tau/2$. Consequently, the photodetected current I_{ph} can be expressed as:

$$I_{ph} = I_0 R_{ref} + I_0 R_{measure} + 2I_0 r_{ref} r_{measure} \cos\left(\frac{4\pi}{\lambda_0}\Delta z + \emptyset\right) \qquad (9)$$

As already stated, a Michelson interferometric scheme can exploit both broadband or narrowband optical sources. To perform measurements of very small displacements or vibrations, high temporal coherence sources are employed, such as a laser. Figure 2.2 shows a typical emission spectrum of a narrowband optical source.
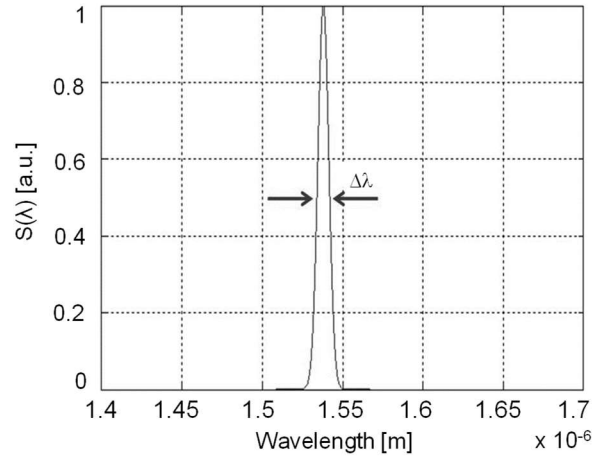
Figure 2.2 Spectral density of a high temporal coherence source.

For high temporal coherence sources, the autocorrelation function can be considered approximately constant. Setting $G(\tau)$ equal to 1, the interferometric component of the detected signal results thus proportional just to $\cos((4\pi/\lambda)\,\Delta z + \emptyset)$, and for $\emptyset = \pi/2$, a condition known as working in quadrature, equal to $\sin((4\pi/\lambda)\,\Delta z)$. Figure 2.3 shows an example of interferometric signal obtained with a laser source when the autocorrelation function is equal to 1.
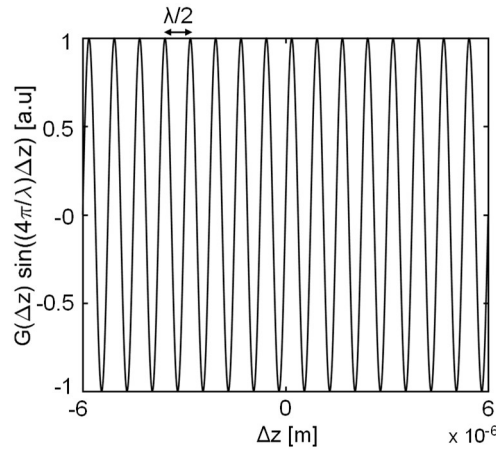
Figure 2.3 Example of interferometric signal generated by a high temporal coherence source.

The signal is periodic and each interferometric fringe corresponds to a displacement equal to $\lambda/2$, where λ is the central wavelength emission of the source. If the mirror position is fixed is possible to retrieve the sample displacement just by counting the number of interferometric fringes. On the other side, if the Michelson interferometer makes use of a low temporal coherence sources, with a wide emission bandwidth, the autocorrelation function cannot be considered constant, and therefore it produces a modulation of the interferometric signal.
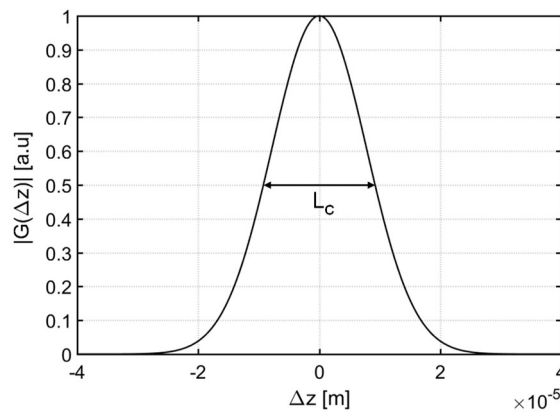
Figure 2.4 Gaussian autocorrelation function, typical of broadband light sources. L_c: coherence length of the source.

Figure 2.4 shows an example of a Gaussian autocorrelation function typical of broadband light sources. The maximum of G(z) occurs at $\Delta z = 0$, thus when the measuring and reference path are equal, and then decreases as the difference in OP between the two paths increases. While interferometers employing sources with high temporal coherence allow the detection of vibrations or displacements, low-coherence interferometry can be applied to detect the relative distance between different layers of a sample. The typical interferometric signal generated by a low temporal coherence source when investigating a single reflective interface sample is shown in Figure 2.5.
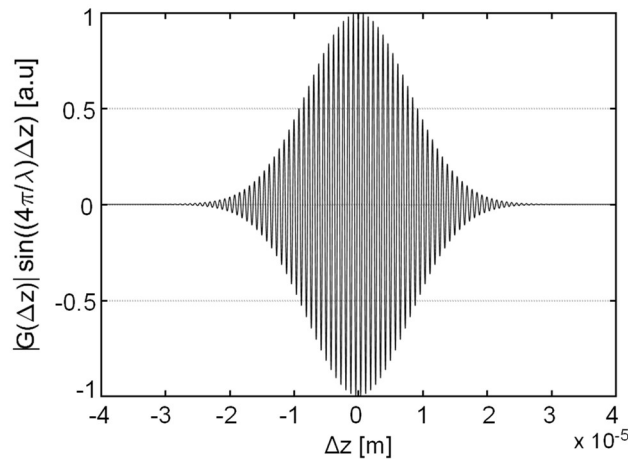
Figure 2.5 Product between periodic interferometric fringes and the autocorrelation function.

The position of the interferometric signal peak corresponds to the distance of the mirror that equals the distance to the reflective interface of the sample.

Low-coherence Michelson interferometers are perfectly suitable not only for the investigation of single interface structures, but also for the examination of multilayer samples. This can be accounted by moving the reference mirror along the z axis. As the mirror is displaced, group of interferometric fringes are developed each time the distance (in OP) between the mirror and the beam-splitter equals the distance to each of the sample reflective interfaces. This kind of configuration is reported in Figure 2.6, where the sample is composed by two reflective interfaces separated by a distance d and z_1 and z_2 represent the mirror positions for which the two groups of interferometric fringes are developed.
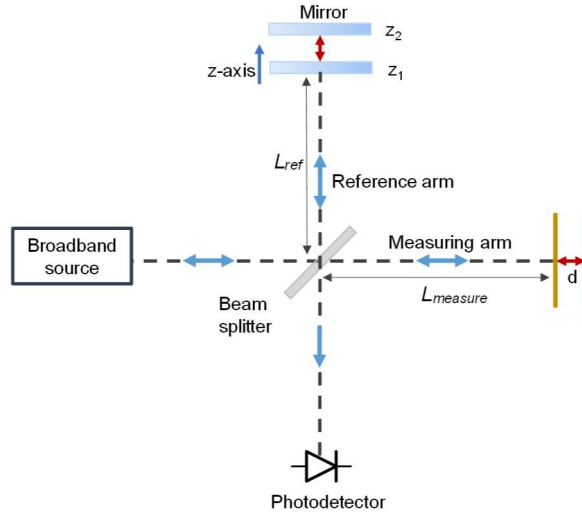
Figure 2.6 Schema of a Michelson interferometer for detection of sample multiple interfaces.
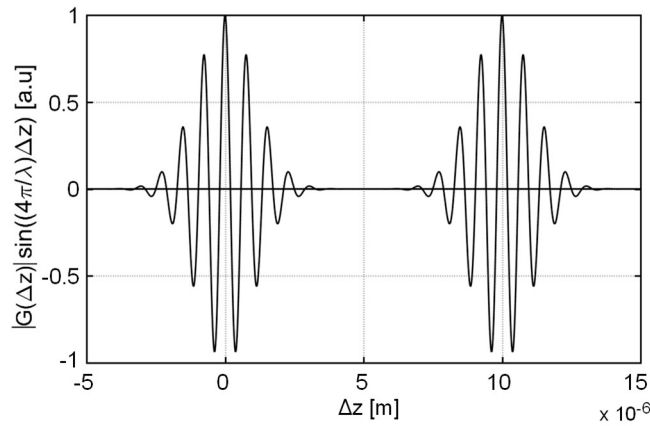
Figure 2.7 Interferometric signal relative to a sample with two reflective interfaces.

Figure 2.7 shows a typical interferometric signal collected when investigating a structure like the one in Figure 2.6. The parameter d is the geometrical distance between the two reflective layers of the sample under test, and is related to the optical path distance $\Delta z = z_2 - z_1$, through the relation

$$OP = n_g \cdot d \qquad (10)$$

where n_g is the group RI of the crossed media. We are here considering the group RI because low-coherence interferometry, as already stated, is based on the interference of wave groups; the carrier wave moves with a speed $v_p = c/n_p$, where n_p is the phase RI and c the speed of light in the vacuum, while the group propagation speed inside the medium is defined as

$v_g = c/n_g$, where n_g is the group RI, that can be expressed as $n_g = n_p - \lambda \frac{dn}{d\lambda}$. The term $dn/d\lambda$ represents the optical dispersion of the medium, relative to the dependence of the RI on the wavelength. Finally, the relationship between the mirror displacement Δz and the physical distance d between the sample interfaces is found equal to $d = \frac{z2 - z1}{n_g}$.

Thus, in this configuration, the Michelson interferometer can be employed to recover the optical path distance between different interfaces of a device. If the geometrical dimension d is known, the group RI of the media crossed by light can be retrieved as $n_g = \frac{OP}{d}$. On the opposite, given the RI of the media, the geometrical dimension of the structure can be reconstructed.

2.2. Instrumental configuration for low-coherence interferometric measurements

To perform low-coherence interferometric measurements we developed a custom designed all-fiber interferometer based on the Michelson configuration. The realized instrumental configuration in shown in Figure 2.8. Radiation from a broadband radiation is coupled in standard telecommunication optical fiber (9/125 core/cladding diameter, SMF). In the experimental verifications, two different broadband read-out sources were employed: a Tungsten lamp and a SLED. The lamp provides a SMF coupled optical power of about -60 dBm/10 nm in the wavelength range from 1.2 μm to 1.6 μm while the SLED (Covega Thorlabs SLD1021) provides a Gaussian emission spectrum with central wavelength $\lambda_c = 1.293$ μm and SMF coupled power approximately equal to 100 μW, when pumped with a current around 11.4 mA at T=25 °C. When employing the SLED, a fiber pig-tailed optical isolator (OI) is used to protect the light source from undesired back-reflections. The emission spectra are shown in Figure 2.9 (lamp) and in Figure 2.10 (SLED). The read-out radiation crosses two bidirectional 2X2 Fiber-Optic (FO) couplers with 50:50 splitting ratio and flat spectral response to be redirected on two different FO paths, i.e. the measuring path and the reference path, both ending with a pigtail-style focuser with aspheric lens (by OzOptics) for the remote read-out of the device under test. The reference path ends with a mirror, mounted on a translational stage, while the measuring path ends with the device to be tested. Port 1 of the first coupler is connected to the broadband light source, port 2 to port 1 of the second coupler, while port 3 is connected to the fist photodiode (PD1 in Figure 2.8) and port 4 is closed to avoid undesired back reflections. Regarding the second coupler, it is connected to the second photodiode (PD2 in Figure 2.8) through port 3, while port 2 and 4 lead respectively to the mirror and the sample under test.

In order to minimize optical dispersions, the reference and measuring paths are matched in length, with a maximum difference of 1 mm.

The two lenses that terminate both paths generate a 50-µm spot at a distance of 23.5 mm, allowing to perform a remote, and thus minimally invasive, optical read-out. Light impinges orthogonally on the devices: low numeric aperture lenses are used, in order to couple back in fiber just that light components that are orthogonally back-reflected, limiting the access of diffused components that have travelled for longer paths at different angles. Back-reflected radiation is coupled back in fiber, and, crossing again the couplers, reaches the two photodiodes, incorporated in a custom designed balanced receiver. The balanced receiver allows an efficient detection of the interferogram by removing the DC component and other common mode signals, while doubling the interferometric component. Moreover, it performs electronic amplification of the photo-generated signals in order to compensate for the different optical powers impinging on the two photodiodes.
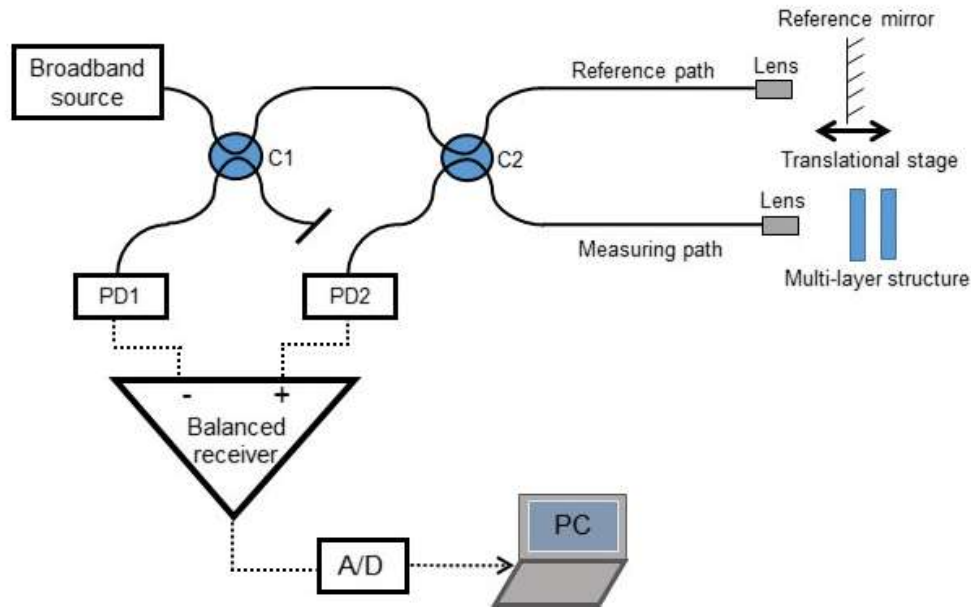
Figure 2.8 Instrumental configuration for low-coherence interferometric measurements. PD1, PD2: photodiodes. A/D: analog to digital converter. C1, C2: couplers. Black solid lines: fiber optic paths; black dashed lines: electric connections.

The generated output voltage is connected to an analog to digital (A/D) conversion board and signals are finally acquired with a PC by means of a LabVIEW interface. The reflective mirror is mounted on a computer controlled translation stage that allows to change the reference path length. Indeed, group of interferometric fringes are detected each time the distance between the reference path and the optical path length to each internal interface of the device is less than the coherence length of the source.
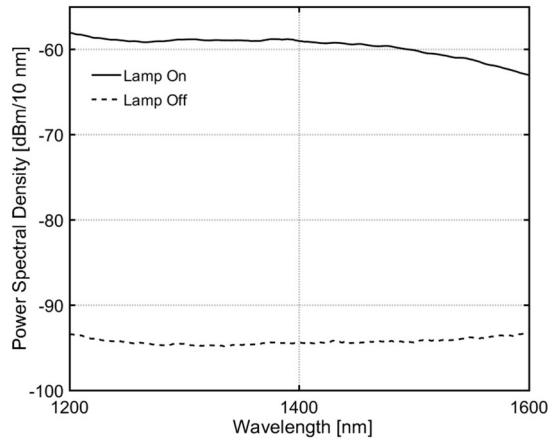
Figure 2.9 Power spectral density of a Tungsten lamp. Solid line: lamp on. Black dashed line: lamp off.
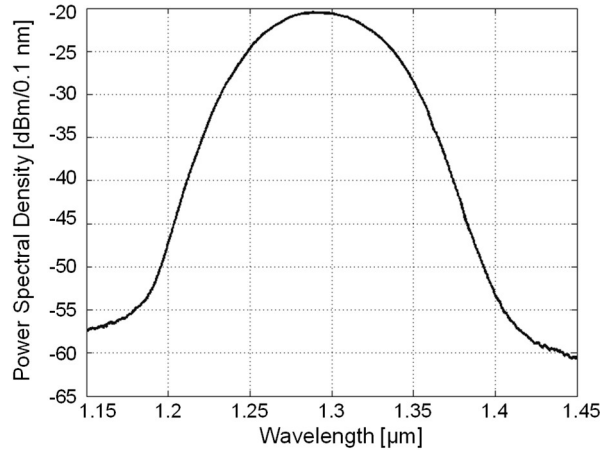
Figure 2.10 Power spectral density of a SLED source pumped with I=11.4 mA at T= 25 °C. λ_c = 1293 nm.

The computer controlled stage allows a maximum achievable speed of 1 mm/s, with a maximum moving dynamic of 5 mm and minimum performable steps equal to 50 nm. In practical experiments, the stage speed was usually set to 10 or 5 μm/s. Small mirror displacements can be as well obtained by means of a piezoceramic actuator controlled by a function generator and a piezoelectric driver. The reference mirror and the device under test are fixed to micro-precision mountings movable along the x-y-z axes, in order to obtain a precise alignment between the device surface and the read-out beam for the optimization of the back-reflected light coupling. Tested devices are interlaced to an external fluidic system through standard luer connections to provide channel filling and easy discard of the samples.

2.3. Experimental results on polymeric devices

This section discusses the experimental results obtained by applying the low coherence interferometric read-out method on the IBIDI™ VI$^{0.1}$ μ-Slide filled with homogenous fluid media [76]. The device structure was firstly characterized by means of the Tungsten lamp and the SLED source. Afterwards, RI sensing was performed by exploiting both read-out sources when flowing through the channel glucose solutions in water at increasing concentration.

2.3.1. Device characterization

In order to characterize the structure of the IBIDI™ VI$^{0.1}$ μ-Slide, a read-out beam was shined orthogonally to the frontal face of one of the six channels the slide is provided with. Figure 2.11 shows the collected signal, as a function of time, obtained when the Tungsten lamp was exploited as read-out source.
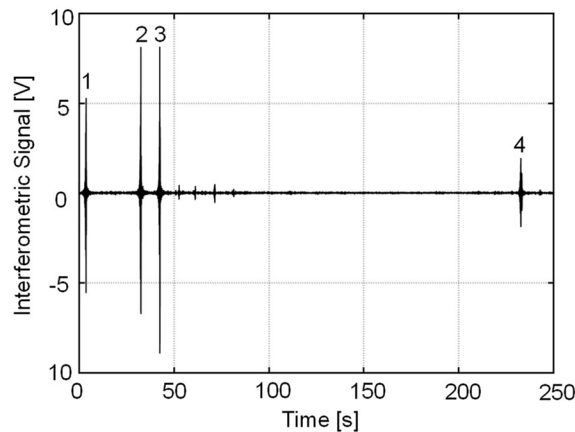
Figure 2.11 Interferometric signal as a function of time relative to an empty IBIDI™ VI$^{0.1}$ μ-Slide channel obtained with a Tungsten lamp as read-out source.

Signals were filtered with a digital band-pass Butterworth filter with f_1=1 Hz and f_2=30 Hz to improve the signal to noise ratio. A Butterworth filter is characterized by a flat frequency response in the passband, and was chosen with a trial and error approach. As expected, four main group of fringes are easily identifiable, each one corresponding to a reflective interface of the device. In particular, peak 1 corresponds to the air/polymer interface, relative to the beginning of the slide front wall, peak 2 corresponds to the polymer/channel interface, peak 3 to the end of the channel (thus to the channel/polymer interface), while peak 4 is related to the end of the slide, and consequently to a polymer/air interface. Moreover,

33

four peaks of smaller amplitude are observable, that were found corresponding to multiple round-trips of the light through the devices, as will be further explained. Acquired signal in the time domain were easily converted in the optical path domain through the relationship $OP = v * t$, where v is the speed of the translation stage, here set equal to 10 μm/s. The signal normalized to the peak amplitude and expressed in absolute value is shown in Figure 2.12 (a).
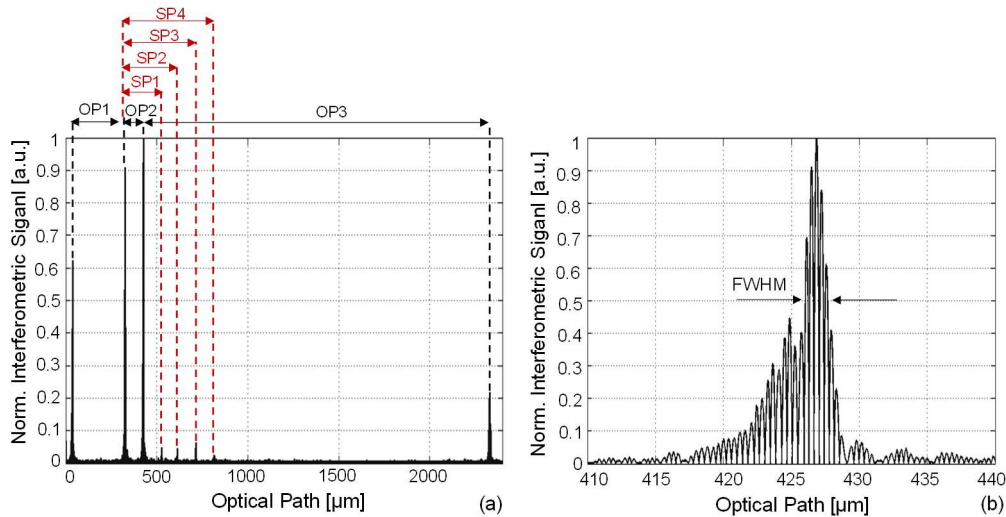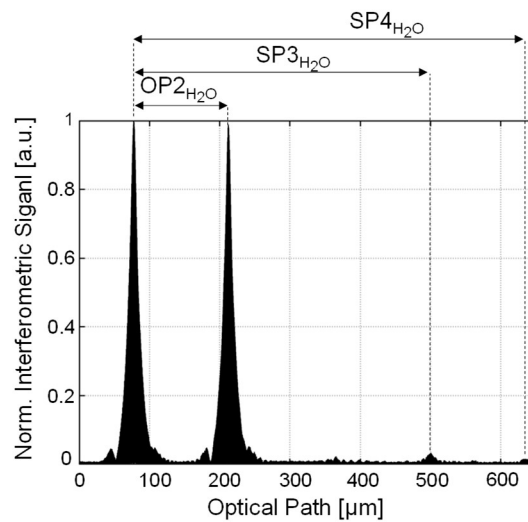

Figura 2.12 (a) Normalized interferometric signal, in absolute value, as a function of the optical path obtained on an empty IBIDI™ VI[0.1] μ-Slide channel using the Tungsten lamp as read-out source. OP1, OP2, OP3: optical paths relative to a single trip of the light across the front layer facing the read-out fiber, the channel, and the back layer, respectively. Note the presence of small amplitude fringe groups due to multiple roundtrips, yielding SP1 = 2·OP2, SP2 = OP1, SP3 = OP1 + OP2, SP4 = OP1 + (2·OP2). (b) Zoom of a single air polymer interface. FWHM: Full Width Half Maximum.

An important parameter when investigating multilayer structures is the axial resolution of the measuring system, which affects the ability to distinguish the various device interfaces. The axial resolution depends on the coherence length (L_c) of the source, which is defined as the width at half maximum (*Full Width Half Maximum*, FWHM) of the autocorrelation function. If two consecutive interfaces are placed at a distance in optical path smaller than FWHM of the autocorrelation function, they won't be distinguishable by the measuring system, as they will lie under the same envelope. To a wide emission spectrum corresponds a short coherence length of the source, that leads to a good axial resolution. Figure 2.12 (b) shows a zoom of the interferogram in Figure 2.12 (a) over a single air-polymer interface. The highlighted FWHM resulted equal to 1.7 μm, thus perfectly suitable to distinguish the consecutive interfaces of the IBIDI™ μ-slide. By taking the distance between the interferometric peaks of the

signal in Figure 2.12 (a), is possible to retrieve the optical path seen by the light when crossing each composing layer of the device. OP1 consequently corresponds to the front slide wall, OP2 to the channel, and OP3 to the long back wall. In particular, we found OP1=289.1 µm, OP2=100.0 µm, OP3=1902.2 µm. The channel depth is in perfect accordance with the declared dimensions, considering the RI of air n_{air}~1 RIU (and recalling Eq. 10). The four highlighted SP paths, instead, correspond to multiple round trips of light into the device composing layers, and in particular we found: SP1 = 2·OP2, corresponding to a double round trip of the light into the channel, SP2 = OP1, thus relative to a second round trip of the light into the polymer coverslip, SP3 = OP1 + OP2, and SP4 = OP1 + (2·OP2), resulting from a double round trip into the channel followed by an additional round trip into the coverslip. We will see how the detection of multiple round trips can be of practical interest when performing RI experimental detection. Figure 2.13 shows three interferometric signals (normalized and in absolute value) relative to the channel respectively filled with air (empty channel), water and a solution of glucose in water at a concentration of 10 % [weight/Volume, w/V]. It can be observed that, as the concentration, and thus the RI, of the fluid filling the channel increases, the optical path relative to the channel proportionally lengthen. The black trace corresponds to the empty channel, the green one to the channel filled with water and the light red one to the channel filled with a glucose solution at 10% concentration.
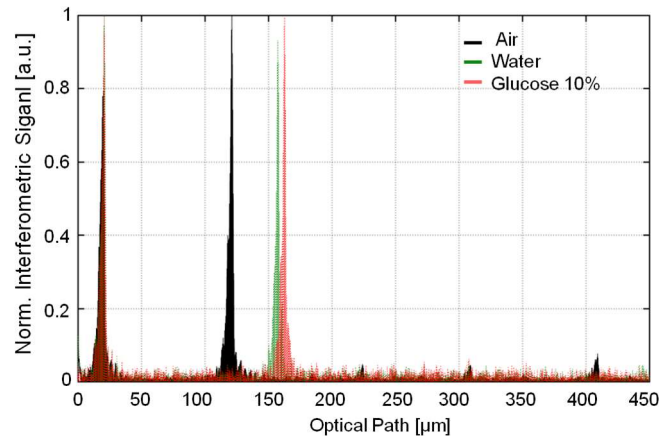
Figure 2.13 Normalized interferometric signals (in absolute value) as a function of the optical path collected employing the Tungsten lamp as read-out source. Just groups of interferometric fringes relative to the channel interfaces are shown. Black trace: signal obtained on the empty channel; green dotted trace: signal obtained on the channel filled by water; pink dotted trace: signal obtained on the channel filled by water-glucose solution with 10% concentration [w/V].

We also observed that when a fluid different from air is present in the channel, the low-amplitude group of fringes due to multiple trips are buried

into the noise. as the field reflectivity relative to these further virtual interfaces is much lower due to the lower RI step between fluids and polymer. As explained in the following section, the detection of multiple round trips is of practical interest when performing refractometric measurements. In fact, it would lead to higher sensitivity values with respect to the detection of a single light trip through the channel. We thus investigated the potentiality of the SLED source, providing higher optical power on a narrower emission interval, in detecting multiple round trips even when the channel was filled with fluids. Figure 2.14 shows the interferometric signal (in absolute value and normalized to the peak amplitude), collected using the SLED source over a channel filled with water. We found that SP1 and SP2 were not visible yet, but we were able to detect $SP3_{H2O}$ and $SP4_{H2O}$, where $SP3_{H2O}=OP1+OP2_{H2O}$, $SP4=OP1+(2*OP2_{H2O})$. In this case, the SLED was driven with I=20 mA to increase the emitted optical power. Signals acquired with the SLED source were filtered with a digital band-pass Butterworth filter with $f_1=0.1$ Hz and $f_2=200$ Hz.

Figure 2.14 Normalized interferometric signal (in absolute value) as a function of the optical path obtained on an empty IBIDI™ VI$^{0.1}$ μ-Slide channel using the SLED as read-out source. $OP2_{H2O}$: optical path relative to a single trip of light across the channel filled with water. $SPR3_{H2O}$ and $SP4_{H2O}$ are due to multiple roundtrips of light, in particular: $SP3_{H2O}=OP1+OP2_{H2O}$, $SP4=OP1+(2*OP2_{H2O})$.

Given the narrower emission window of the SLED source compared to the lamp, and consequently the longer coherence length, a higher value of FWHM was found in this case. In particular, considering a single water-polymer interface, we found a FWHM = 13.4 μm, thus still suitable for a careful investigation of the IBIDI™ μ-slide.

2.3.2. Refractive index detection of homogenous fluids

In view of the application of low-coherence interferometric measurements for RI monitoring, we performed optical path measurements over a μ-slide channel filled with solutions of glucose in water at increasing concentration, in the range from 0 up to 33% [w/V]. Increasing concentrations corresponds to increasing RI (concentration and RI are usually in a linear relationship). In particular, for glucose solutions, knowing the RI of the solvent (here water) and the concentration of the solute, is possible to retrieve the RI of the solution, through the equation [85]

$$n = n_0 + \alpha \cdot C \qquad (11)$$

where n_0 = 1.3154 RIU, C is the solute concentration and $\alpha = dn/dC$ is the RI increment specific for each solute. In case of glucose, α = 0.145 cm^3/g [86] . To ensure the channel filling and sample discard, we connected the slide to an external fluidic path. Figure 2.15 shows the IBIDI™ μ-slide fixed to a precision mounting for the efficient alignment with the read-out beam and connected to the fluidic system through standard luer connections. The bottom tube was dipped into a vial containing the solution to be tested, while the top one led to a peristaltic pump, actuated to aspire the sample. The pump was firstly activated to allow the channel filling: the measurements were performed and the sample was discarded activating again the pump in the same direction.
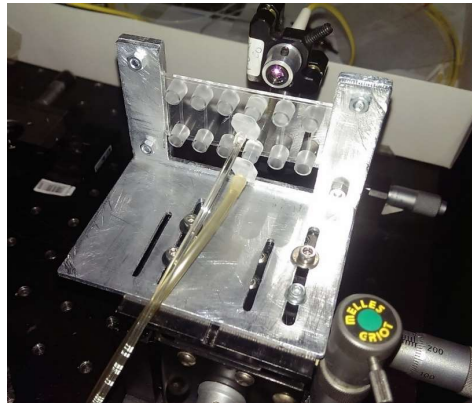
Figure 2.15 Picture of μ-Slide integrated in the experimental setup and connected to the fluidic system.

For each sample, at least three measurements were repeated. Then, from the acquired interferometric signals, we extracted the optical path OP2 relative to the channel. Figure 2.16 reports average values and standard deviations of OP2 as a function of the glucose RI. Figure 2.16 refers to the signal obtained exploiting the samples by means of a Tungsten lamp. The straight line represents the linear fitting of the data and provides the

sensitivity of the device for RI sensing, defined as the increase of the optical path relative to the channel given an increase of the RI of the filling media. In particular

$$S = \frac{dOP2}{dn} \tag{12}$$

A sensitivity S = 95.7 µm/RIU was obtained. To estimate the minimum detectable RI changes, we calculated the LoD of the measurement, defined as [4]

$$LoD = \frac{3\sigma}{S} \tag{13}$$

where S is the sensitivity and σ is the standard deviation of the experimental data. In this case, we obtained a best LoD=9.4x10^{-4} RIU. Given the definition of sensitivity it is clear how monitoring the shift of group of fringes corresponding to a double round trip of light in the fluidic channel should lead to a double sensitivity.
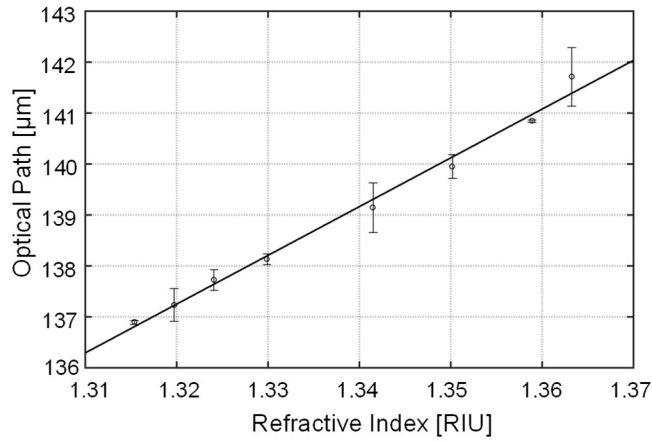
Figure 2.16 Optical path length and standard deviations of the filled fluidic channel as a function of the RI. Measurements were performed using a Tungsten lamp as read-out source. The straight line represents the best linear fitting of the data.

With this aim, we exploited the potentiality of the SLED source, providing a higher optical power on a narrower wavelength interval, allowing to obtain a better signal to noise ratio also for fringes related to multiple round trips. We monitored the increase of SP4= OP1+2*OP2 as a function of the filling media RI. Figure 2.17 shows the calibration curves obtained plotting OP2 (blue circles, referring to the left axis) and SP4 (green stars, referring to the right axis) as function of glucose solutions RI.

The blue dashed trace represents the best linear fitting of the OP2 average values, while the green solid line is relative to the SP4 average values. Monitoring the single round trip, we obtained a sensitivity

S=87.7 µm/RIU, while for the double roundtrip we obtained S=177.8 µm/RIU. As expected, the double round trip resulted in an approximately doubled sensitivity with respect to the one relative to a single crossing of the channel. We then retrieved the determination coefficient R^2, which gives the proportion of the variability of the dependent variable explained by a variation of the independent variable. R^2 can assume values between 0 and 1: the closest to 1, the higher is the proportion of the dependent variable change predictable by the independent variable. We obtained $R^2_{OP2}=0.9982$ for the single roundtrip data and $R^2_{SP4}=0.9960$ for the multiple roundtrip data, testifying a high dependence of the channel OP on the media RI. Regarding the limit of detection, we obtained a best LoD equal to 3.42×10^{-4} RIU for the single round-trip and a best LoD of 1.2×10^{-3} RIU for the multiple round-trip. It can be noticed as, despite the higher sensitivity, a lower LoD was obtained following the multiple round-trip. This can be probably addressed to the higher uncertainty in defining the exact position of the interferometric peak due to the multiple crossing of light through the channel, as a consequence of the reduction of the signal to noise ratio as the light crosses multiple times the channel.
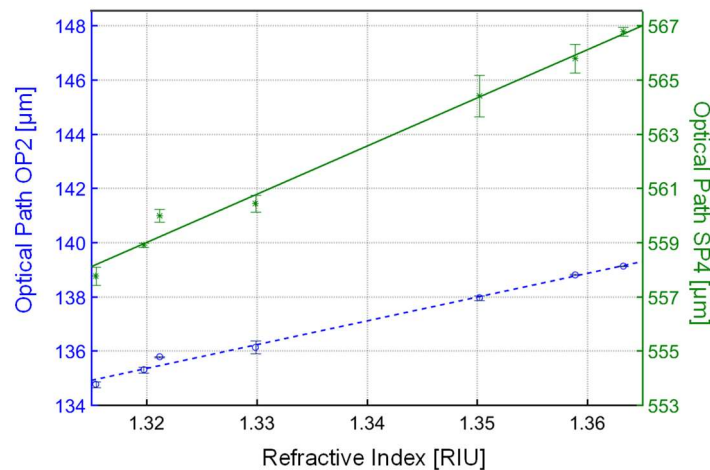
Figure 2.17 Optical path length of the filled fluidic channel obtained with a SLED source as a function of the RI. Blue circles refer to a single channel crossing (and to the left axis) while green stars refer to the double round trip (and to the right axis). Straight lines provide the linear fitting of the data.

As asserted before, in order to perform refractometric experiments, fluids were inserted into the channel by actuating the peristaltic pump, the measurements were taken, and the channel was when emptied actuating again the pump in the same direction. Optical measurements were thus performed on fluids in static conditions. In view of a possible future development consisting in performing the RI detection on fluids in motion,

we performed interferometric measurements on the IBIDI™ slide channel while the peristaltic pump was kept on and fluids were flowing.

Figure 2.18 compares signals acquired over a slide channel filled with water and with a glucose solution in water at a concentration of 33% in static condition (upper graph), to signals acquired while the same fluids were flowing (lower graph). No significant differences were observed between the signals acquired in the two experimental conditions. We retrieved the optical path OP2 from the shown traces, obtaining $OP2_{water}=134.67$ µm and $OP2_{glucose33\%}=139.05$ µm for fluids in static condition and $OP2_{m,water}=134.76$ µm and $OP2_{m,glucose33\%}=139.12$ µm for fluids in motion. As can be noticed there's a good agreement between values obtained in both experimental conditions, with a maximum difference lower than the 0.1%.
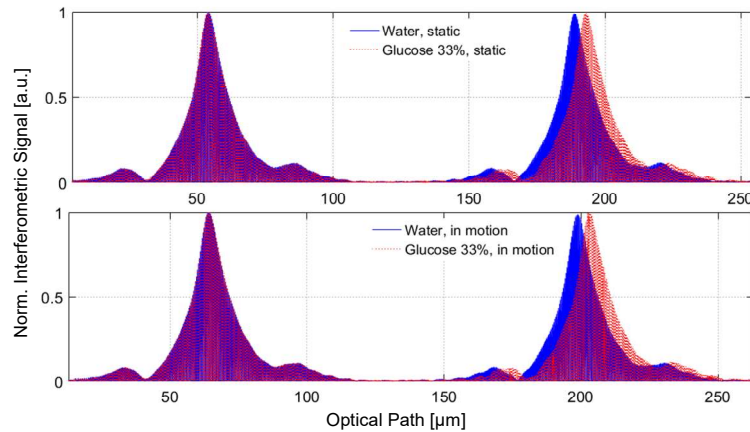
Figure 2.18 Normalized interferometric signals (in absolute value) collected on a channel of the IBIDI™ µm-slide in presence of water (blue solid trace) and glucose 33% (red dotted trace). The upper graph represents traces collected when the fluids were in static condition, while the lower ones were collected as the fluids were flowing.

In conclusions, we demonstrated the applicability of low-coherence interferometry to the RI detection of fluids inserted into a commercial polymeric device like the IBIDI™ $VI^{0.1}$ µ-Slide. Using a SLED as read-out source, we were able to monitor the double round of light into the fluidic channel, leading to a double sensitivity with respect to traditional single-path measurements. The reported experiments were performed at room temperature, with no specific temperature control, but since source and detector are on the same side, thermal control could be easily achieved on the opposite side of the device. As µ-slides can be used as flow-through device, the proposed system could be also applied in the field of drug discovery, to detect in real-time the response of a group of cells confined in the slide channels in response to external stimuli. In fact, cell damages, such apoptosis, results in changes in cell shape, morphology and size [87], which implicate variations of RI.

2.4. Experimental results on rectangular glass micro-capillaries

This section describes the experimental results obtained when testing rectangular glass micro-capillaries firstly with homogenous solutions, and subsequently with highly scattering media such as dairy products and red blood cells (RBCs). Finally, the system was applied to the detection of the average RI of populations of cells gently confined into the capillary channel. Preliminarily, the structure of capillaries with different nominal dimensions was optically investigated. All results presented in this section were attained using the Tungsten lamp as read-out source.

2.4.1. Devices characterization

In order to perform interferometric measurements on rectangular glass micro-capillaries the same instrumental configuration used for testing the IBIDI™ µ-slide was employed. A different mounting, however, was required to integrate the device into the experimental setup. In fact, as explained before, glass micro-capillaries are fragile devices that need protection and need advanced solutions to be integrated into the external fluidic path. As already explained in Paragraph 1.2, a custom 3D printed support was developed to overcome these challenges. Figure 2.19 shows a picture of a rectangular glass capillary inserted into the polymeric support and integrated into the experimental setup. The luer end is connected through standard tubing to a peristaltic pump, employed just to push fluids out of the device after the measurements, since fluids entered in the device just by capillary action.
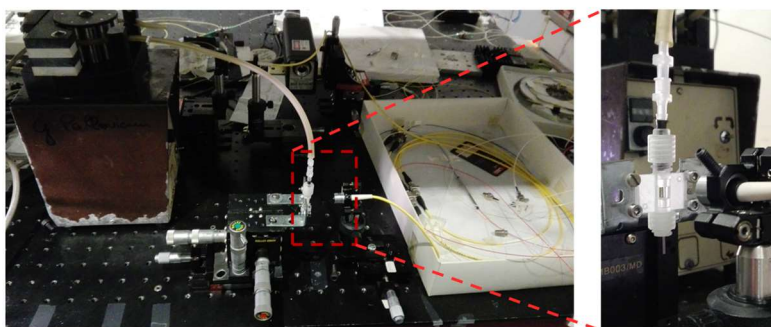
Figure 2.19 Picture of a rectangular glass micro-capillary inserted into the 3D printed polymeric support and integrated in the experimental setup.

Before proceeding with the RI sensing experiments, the device structure was first characterized. As stated before, rectangular glass micro-capillaries are commercially available in a wide range of dimensions. For the

experiments that will be discussed in this Chapter and in the following, four types of capillaries were employed. In particular, we chose two capillaries with channel depth d=50 μm, one with walls thicknesses $t_f=t_b=50$ μm and one with 35-μm-thick walls, another capillary with channel depth d=30 μm and $t_f=t_b=21$ μm, and an additional one with a deeper channel, equal to 100 μm, and walls thicknesses equal to 70 μm. All capillaries had a width W of one order of magnitude bigger with respect to the channel depth, except for the symmetric capillary with $t_f = t_b = 50$ μm, where W=1 mm. We recall that the manufacturer ensures a tolerance of 10% for channel depth, 10% for the width, and 20% for walls thickness. All experiments on glass capillaries were performed setting a stage speed v=5 μm/s. Also in this case, interferometric signals were filtered with a digital band-pass Butterworth filter with f_1=1 Hz e f_2= 30 Hz in order to improve the signal to noise ratio.
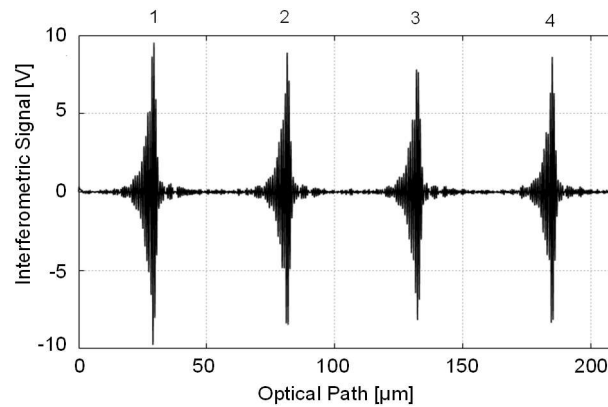
Figure 2.20 Interferometric signal as a function of the optical path obtained on an empty capillary with channel depth d=50 μm and wall thickness $t_f=t_b=35$ μm. 1, 2, 3, 4: interface positions.

Figure 2.20 shows a typical interferometric signal collected on a capillary with channel depth d=50 μm and wall thicknesses $t_f = t_b = 35$ μm. Four main fringe groups are identifiable, corresponding to the four interfaces encountered by the light when orthogonally crossing the rectangular micro-capillary. In particular, peak 1 corresponds to the beginning of the front wall, while peak 2 to its end; peak 3 and 4, in the same way, correspond to the beginning of the back wall and to the end of the capillary. Consequently, peak 1 and peak 4 always correspond to an air-glass interfaces, while peak 2 and 3 are related to the media inserted into the capillary. Figure 2.21 reports the same interferometric signal normalized to its peak amplitude and in absolute value. Taking the distance between the four interferometric peaks, we retrieved the OP value relative to the capillary composing layer. In particular, we found OP1=52.38 μm, relative to the front wall, OP2=50.89 μm, relative to the gap and OP3=52.61 μm, relative to the back wall. Considering the group RI of glass $n_{g,glass}$ = 1.4752 RIU (BOROFLOAT® Schott Glass) [88], and $n_{air} \sim$ 1 RIU,

through Eq. 10, we obtained t_f = 35.51 µm, d=OP2 and t_b = 35.66 µm. The retrieved geometrical dimensions are in good agreement with what declared by the manufacturer, considering the given tolerances.
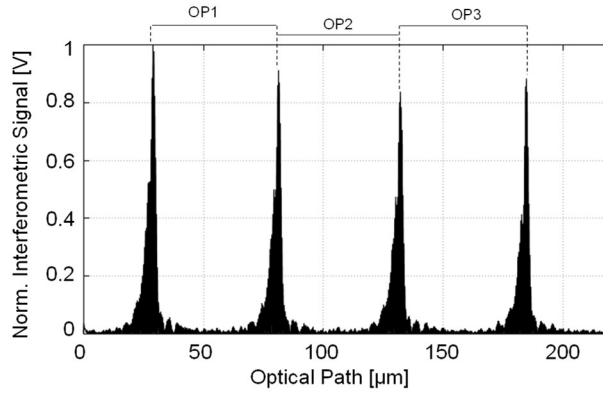
Figure 2.21 Absolute value of a normalized interferometric signal relative to an empty capillary with t_f=t_b=35 µm and d=50 µm.

Figure 2.22 and 2.23, instead, report the interferometric signals (normalized and in absolute value) obtained respectively for a capillary with t_f=t_b=21 µm and d=30 µm and for a capillary providing t_f=t_b=70 µm and d=100 µm (nominal values). Again, the measured thicknesses resulted in agreement with the declared values. Indeed, we got t_f=22.44 µm, t_b=22.30 µm and d=29.81 µm for the first kind of capillary, and t_f=79.40 µm, t_b=76.45 µm and d=101.81 µm for the second one.
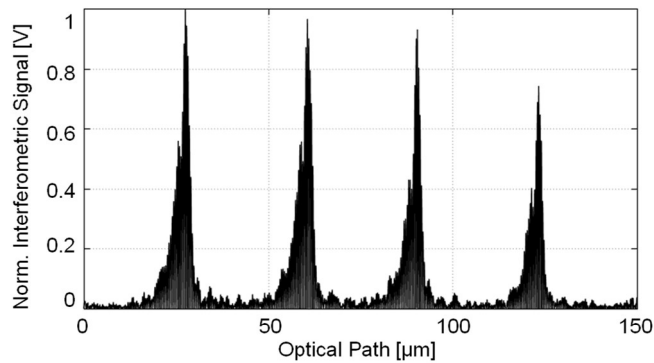
Figure 2.22 Absolute value of a normalized interferometric signal relative to an empty capillary with t_f=t_b=21 µm d=30 µm.
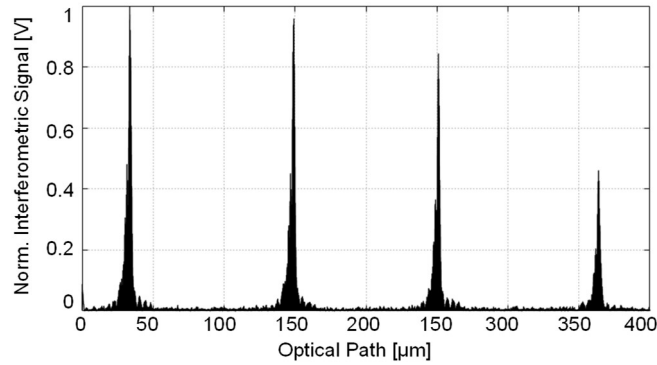
Figure 2.23 Absolute value of a normalized interferometric signal relative to an empty capillary with $t_f=t_b=70$ µm $d=100$ µm.

Figure 2.24 shows two interferometric signals (normalized and in absolute value) related to the capillary with $t_f=t_b=d=50$ µm. The pink solid trace represents the signal acquired on the empty capillary, while the black dotted trace the signal acquired on the same capillary filled with water. It can be noticed as the OP relative to the channel lengthen when a fluid with RI higher than that of air is inserted into the capillary channel (in Figure 2.24, water), while the OP values relative to the walls remain constant, since the walls thickness is obviously unaffected by the presence of fluid in the capillary. More precisely, referring to the trace relative to the empty capillary, we found $OP1_{air}=76.42$ µm, $OP2_{air}=50.57$ µm, $OP3_{air}=78.79$ µm, corresponding to geometrical dimensions $t_f=51.80$ µm, $t_b=53.41$ µm, $d=OP2_{air}$, again in accordance with the nominal values. When the capillary was filled with water, we found $OP1_{water}=76.41$ µm $\approx$ $OP1_{air}$, $OP2_{water}=67.97$ µm, $OP3_{water} = 78.57$ µm $\approx OP3_{air}$.
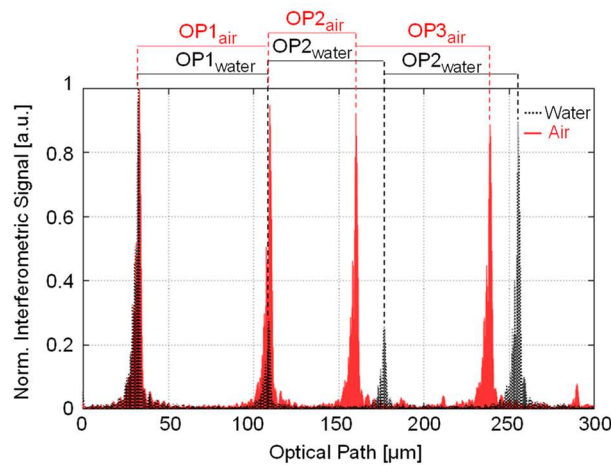
Figure 2.24 Normalized interferometric signals (in absolute value) relative to a capillary with wall thickness and channel depth equal to 50 µm. Solid pink trace: empty capillary; black dotted trace: capillary filled with water. The optical path distances relative to the glass walls and to the channel are highlighted.

Looking at Figure 2.24, an additional factor that deserves to be highlighted is the amplitude reduction of the second and third peaks detected in the presence of water with respect to the peak amplitude of the same groups measured in the presence of air. This phenomenon occurs because the difference in RI between glass and air is higher than that between glass and water, and thus is higher the percentage of back-reflected radiation at the second and third interfaces. Low-coherence interferometry allows to directly retrieve the group RI of a fluid, with no need of calibration. In fact, recalling again the OP definition given in Eq. 10, it is possible to calculate the RI of the filling media as OP_{media}/OP_{air}, where OP_{media} is the optical path relative to the capillary gap filled with a given media, while OP_{air} is the optical path measured on the empty capillary, being $n_{air} \sim 1$ RIU. Considering the OP values obtained from the two interferograms in Figure 2.24, we retrieved the group RI of water, obtaining $n_{g,water} = 1.3433$ RIU, in quite good agreement with values found in the literature [89]. Data relative to different channel fillings were sequentially taken in the same capillary position. In some cases, though, for example when investigating cell RI as described in Paragraph 2.4.4, measurements had to be taken in different capillary positions. For this reason, before proceeding with the RI detection experiments, we estimated the dimension uniformity within the same capillary and between different capillary samples. The variability of the wall thickness and in particular of the channel depth resulted reasonably low, thus suited for the experimental method we employed.

2.4.2. Refractive index detection of homogenous fluids

As first test, we performed interferometric measurements on a capillary with $t_f=t_b=d=50$ μm filled with Ethylene Glycol (EG) solutions in water at increasing concentrations [73]. Ethylene Glycol is an organic compound, mainly used as raw material for polyester fiber manufacturing and in antifreeze formulations.

In particular, we employed EG solutions in water in concentrations equal to 0%, 10%, 20%, 30%, 40%, 50%, 60%, 80% and 100%. The corresponding group RI values were retrieved from the RI of the starting components through the Lorentz-Lorenz equation [90]:

$$\frac{n_s^2 - 1}{n_s^2 + 2} = c_1 * \frac{n_1^2 - 1}{n_1^2 + 2} + c_2 * \frac{n_2^2 - 1}{n_2^2 + 2} \tag{14}$$

where n_s is the group (or phase) RI of the solution, c_1 and c_2 are the concentration of the two components and n_1 and n_2 their group (or phase) RIes. To retrieve the RI of solutions at various concentrations, we considered $n_{g,water} = 1.3519$ RIU [91] and $n_{g,EG} = 1.4276$ RIU [92] .

At least three data samples were taken for each solution and the fluid was then discarded pushing air through the actuation of the peristaltic pump. Experiments were performed starting from water and proceeding for increasing EG concentration.

Reporting the OP mean values (and the relative standard deviations) corresponding to the capillary gap and to the front and back wall as a function of the EG solution RI, the calibration curves reported in Figure 2.25 were obtained. The straight lines represent the linear fitting of the data. Taking the slope of the fitting line of the data relative to the channel, we obtained a sensitivity value S = $dOP2/dn$ = 59.11 µm/RIU. The slope of the fitting line of data relative to the front and back walls, on the other side, resulted very small, and respectively equal to -0.41 µm/RIU and 4.35 µm/RIU. This is in accordance with what expected, since the walls thickness must be unaffected by the change of the RI of the filling fluid. Given the definition of sensitivity, and considering Eq. 10, it is clear how the sensitivity is related to the geometrical dimension of the sensitive area (i.e. the channel). In this case, the theoretical sensitivity is thus $S_t \sim 50$ µm/RIU. We obtained a slightly higher value, that can be probably addressed to temperature fluctuations, being the RI depending on the temperature. All experiments were performed at room temperature, without any specific temperature control of the fluid.

Related to this dataset, we obtained a determination coefficient R^2_{gap}=0.9898, whereas, as expected, much lower values were found for the front wall, R^2_f=0.0035, and for the back wall, R^2_b=0.2462. Regarding the detection limit of the measurement, we obtained a best LoD equal to 3.5×10^{-3} RIU.
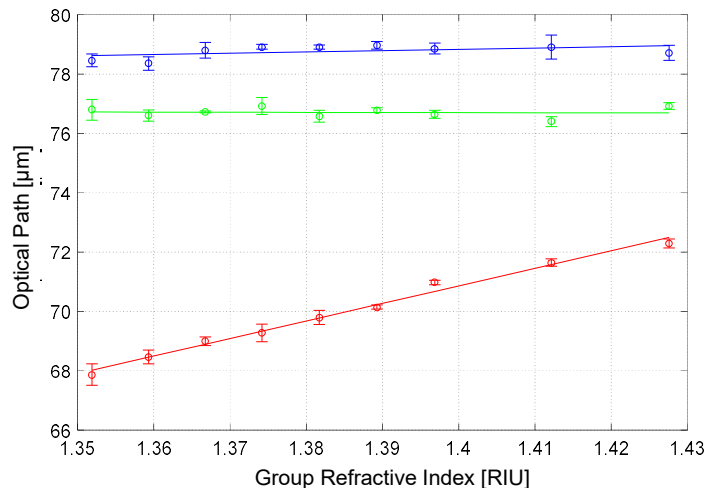
Figure 2.25 Mean values and standard deviations of the optical path values relative to the gap (red dot), the front wall (green dot) and the back wall (blue dot), obtained for a capillary with $t_f = t_b = d = 50$ µm as a function of Ethylene Glycol solutions group RI. Straight lines represent the linear fitting of the data. Average values and standard deviations are calculated at least on three values.

We then retrieved the experimental RI values of the EG solutions as $OP2_{EG}/OP2_{Air}$. Figure 2.26 shows the comparison between the experimental group RI and the ones theoretically obtained through Eq. 14, reported as a function of the EG concentration. It can be noticed as a quite good agreement is observable between theoretical and experimental data. The red dashed trace provides the linear fitting of the experimental group RIes.
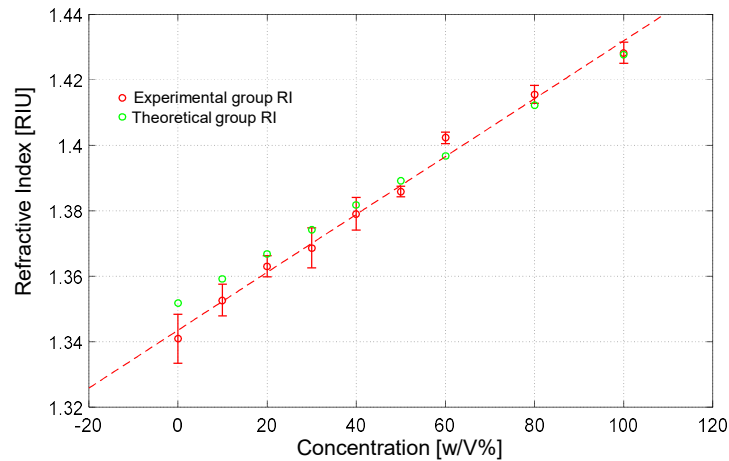
Figure 2.26 Mean values and standard deviations relative to the experimental EG group RI (in red) obtained through low-coherence reflectometry, and theoretical EG group RI calculated though the Lorentz-Lorentz equation (in green). The red dashed trace provides the linear fitting of the experimental data.

We then analyzed another 50-µm capillary filled with solutions of biological interest. In particular, we chose glucose solutions in water with concentrations from 0% to 30% as test fluids. RI values were again retrieved through Eq.14. Figure 2.27 shows the calibration curves obtained with the procedure previously discussed. Given the absence in the literature of reliable group RI values of glucose solutions, data are reported as a function of the phase RI.

Here, a sensitivity S=44.61 µm/RIU was found, while by linearly fitting the data relative to the walls we obtained slopes m_f=-0.99 µm/RIU (front wall) and m_b=4.57 µm/RIU (back wall). The relationship between phase and group RI is in principle non-linear, and small deviations of the obtained values from the expected ones can in this case also be due to the use of phase RI instead of group RI for the reconstruction of the calibration curves. In this case, we obtained a best LoD of $3.8x10^{-3}$ RIU.
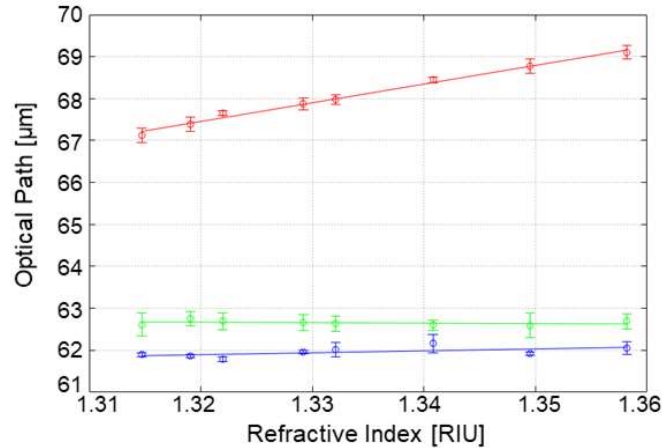
Figure 2.27 Mean values and standard deviations of the optical path values relative to the gap (red dot), the front wall (green dot) and the back wall (blue dot), obtained for a capillary with $t_f=t_b=d=50$ µm as a function of glucose solutions phase RI. Straight lines represent the linear fitting of the data. Average values and standard deviations are calculated at least on three values.

2.4.3. Investigation of highly diffusing media: dairy products and red blood cells

In the previous paragraph, low-coherence interferometric measurements were demonstrated suitable for the investigation of multilayer structures and for RI detection of homogenous fluids. Homogenous media are characterized by low scattering coefficients. This factor represents an advantage when performing RI detection through the method we proposed: in fact, the peak amplitude of the third and fourth fringe groups of an interferogram like that in Figure 2.24 depends on the scattering and/or absorption properties of the filling fluid. Whereas fluid absorption can be neglected in the near-infrared, scattering losses in dense solutions can play an important role in reducing the amplitude of the back reflected optical field.

To investigate the applicability of the proposed measuring technique to the RI detection of scattering fluids, we firstly tested it on highly diffusing media such as whole milk and dilutions of whole milk in water. Then, populations of RBCs were tested [75]. Milk is a hydrocolloid suspension of casein micelles and a colloidal emulsion of fat globules, both dispersed in a water based medium [93]. When shined with a light beam, since the RI of milk fat and casein micelles differs from that of milk serum, the impinging radiation is forced to deviate from its straight trajectory [94].

Figure 2.28 shows interferometric signals collected on a 100-µm-channel capillary filled with air (empty capillary), water, and commercial cow milk (homogenized and pasteurized). As expected, the channel OP increased when filled with fluids, while the OP relative to the walls (i.e. the distance between the first and second and third and fourth

interferogram peaks) remained constant. Moreover, as observed before, as a consequence of the lower RI difference between glass and water (or milk) with respect to glass and air, the amplitude of the second and third fringe group decreased. Additionally, the amplitude of the peaks relative to the third and fourth interfaces was further reduced by the scattering effects occurring with milk filling. Anyway, each group of fringes was still clearly recognized, allowing the OP detection and RI estimation.
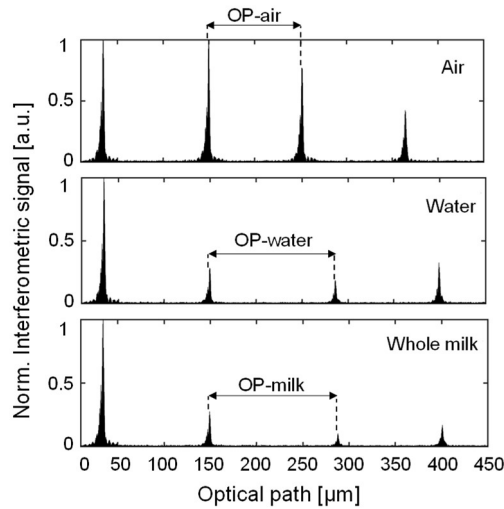
Figure 2.28 Absolute value of normalized interferometric signals as a function of the optical path obtained on a 100-µm-deep capillary in presence of air (upper trace), water (middle trace) and milk (lower trace). OP_{air}: optical path length relative to the channel filled with air; OP_{water}: optical path length relative to the channel filled with water; OP_{milk}: optical path length of the channel filled with milk.
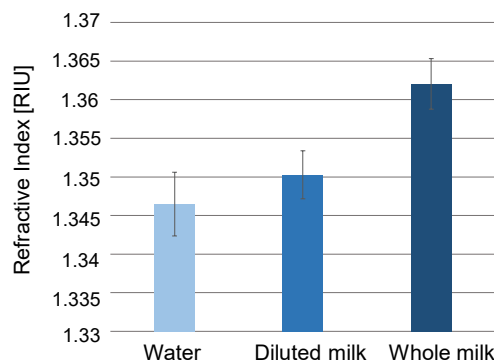
Figure 2.29 Column bar graph with average RI and standard deviations of the detected RI values of water, whole milk, and a mixture of 50% water and 50% whole milk (diluted milk).

Figure 2.29 shows the average RI values (on three data points) and standard deviations obtained for water, whole milk, and a dilution of whole

milk in water (50% milk, 50% water). The values of average group RI are: $RI_{water}=1.3465$ RIU, in good accordance with values reported in the literature [89], $RI_{whole-milk}=1.3620$ RIU and $RI_{diluted-milk}=1.3503$ RIU. Whole milk RI resulted visibly different from that of water. Moreover, a clear difference was present between whole and diluted milk RI, allowing, in principle, to detect the product adulteration due to water dilution.

We then applied the same measuring method for RI detection of normal RBCs, as their optical properties are already well documented in the literature and can be used as reference. RBCs RI can be an interesting diagnostic parameter, since an abnormal hemoglobin content, such as in iron-deficiency anemia or thalassemia, can induce an RI variation in RBCs [95]. RBCs were obtained from peripheral blood of a healthy volunteer donor. Five ml of anti-coagulated (with sodium citrate) whole blood was spun down at a Relative Centrifugal Force (RCF) of 150 g for 15 min. Plasma was aspirated and discarded and also the buffy coat at the interface (constituted by white blood cells) was eliminated. A small aliquot of the remaining concentrated RBCs was transferred at the bottom of a 1 ml plastic conic tube. Figure 2.30 (a) shows a bright field microscopy image of RBCs in a 50-µm-channel capillary. Three different region are easily identifiable, respectively filled by air, medium (i.e. plasma) and red blood cells. Figure 2.30 (b) shows the RI average values and standard deviations for plasma and RBCs relative to repeated measurements, also on different experimental samples. In particular we obtained $n_{g,Plasma} = 1.362 \pm 0.007$ and $n_{g,RBC} = 1.442 \pm 0.017$ RIU. The RI estimated for RBCs is in good agreement with values previously reported in the literature by other authors, though obtained with a more complex setup and larger sample volume. Similar values were, for example, reported in [96] [97] [98], with tomographic measurements based on index matching. These comparisons were performed to support and validate our technique for RI estimation of non-homogeneous fluids.
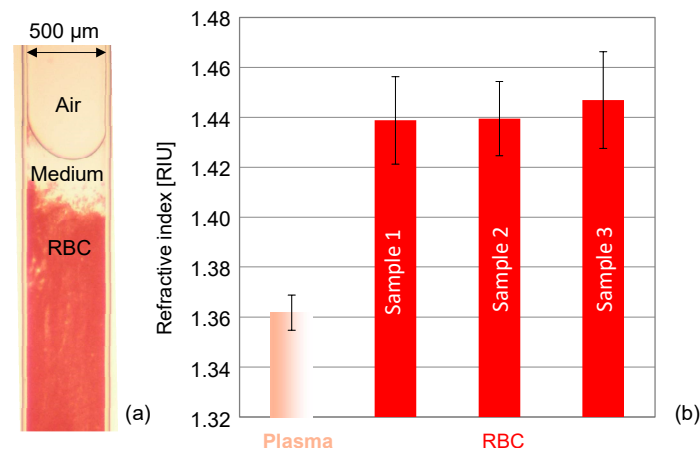
Figure 2.30 (a): Bright field image of a 50-µm capillary filled with RBCs. (b): column bar graph reporting the average values and standard deviations of the detected RI of plasma and RBCs from three different samples.

2.4.4. Advanced proof of principle: refractive index detection of normal and transformed human cells

Supported by the results obtained on highly scattering media such as whole milk and human RBCs, as an advanced proof of principle of the proposed detection method, low-coherence interferometry was applied for estimating the RI of a population of nucleated cells gently confined in rectangular glass micro-capillaries [75]. Cells RI represent an interesting parameter since it can give insight into the composition and function of cells being linked to their biophysical properties [99]. Cells RI can also provide important information in chemical analyses, in studies on cell permeability and in hematology [100] [83] [101]. Cell RI provides insights relative to the chemical composition and organization of the cell content and, therefore, this parameter has been considered highly significant also in cell biology and cyto-pathology [102] [103] [104]. Indeed, variations in tissue RI owing to changes in the cellular components play an important role in tissue light scattering effects, which have the potential to provide information about tissue pathology [99]. Moreover, in cancer biology, the RI is considered an indicator of cell malignancy [105] [106] since the RI of proliferating cells is relatively higher than that of normal quiescent cells [102] [105] [107] [108], probably because of a higher DNA content of the nucleus [109]. The RI is modulated by morphological and functional variations in the cell, particularly in transitions related to the loss of viability. Cell structural modifications induced by cell death (for apoptosis or for necrosis) are characterized not only by biochemical events but also by significant volume changes.

The apoptotic pathway is associated with a cell shrinkage whereas necrosis induces an increase in cell size. These variations are currently detected by means of light scattering measurements in flow cytometry: forward scattering (FSC) refers mainly to cell size while side scattering is related to the cell surface and to the inner structure of the cytoplasm and nucleus. FSC is strongly linked to RI since a cell volume increase/decrease induces an opposite variation of this parameter. RI may become a significant and intrinsic indicator of apoptotic cell status that is usually monitored via fluorescent detection of FITC-labeled Annexin-V [110]. A large variety of biomedical applications (among others, the area of drug discovery) may benefit from an alternative approach to scattering detection by flow cytometry (complex and expensive method) and to fluorescence measurements (characterized by a grade of cell toxicity) [111]. Several methods have been proposed to measure the cell RI, based on microscopy techniques [102] [112] [113] [114] [115], on optical trapping [116] [117] [118], or on hydro-mechanic holders [83]. Microscopy approaches require bulky imaging systems, complex analytical algorithms and allow measurements on living cells adherent to a slide or on histological slices [108]. Optical trapping techniques, on the other hand, require cell confinement by means of a light beam with high optical power, and thus may be potentially invasive for cells. Several optical interferometric

configurations [119] have been developed such as micro-chip refractometers based on a Fabry-Pèrot resonant cavity [83] [104]. Lue et al. have confined live cells in micro-channels of fixed vertical height, but accuracy has been limited by thickness variations in the horizontal plane [120]. Zilbershtein et al. [121] have demonstrated that Fourier transform infrared surface plasmon resonance can estimate the average RI of cell populations in view of its application to detect in real time the response of cells to environmental changes. Most of the reported approaches allow measurements on individual cells, even in 3D [122], and on a relatively small number of them (up to a few hundreds). Although these methods can give very accurate results, they require, in most of the cases, complex or invasive measuring techniques, often based on lengthy processes. Therefore, there is still the need to demonstrate more attractive systems to estimate cell RI (suitable also for un-fixed samples) based on miniaturized devices, better if low-cost and available off-the-shelf, easily interfaced with the selected optical read-out approach. It would be also worthy to recall that single cells belonging to the same line and resulting from the same experimental culture could be in different functional states (quiescent or proliferating) and, if proliferating, also in various phases of the cell cycle: thus, they might have different macromolecular contents and RI. Testing a cell population allows us to yield the average RI value typical of that population (for example of a tumor) overall. In biomedical analyses, it is interesting to obtain data relative to the cell population, for example for monitoring the changes in RI in response to various physical and biochemical stimuli or, in the case of the drug-discovery field where a large number of tests is required, on cell cultures.

As an advanced proof of principle of the application of low-coherence interferometry to highly scattering media such as cells populations, we applied the proposed technique to human cells belonging to the transformed and normal compartments. Further information about the employed cell lines are given in the following materials and methods paragraph.

2.4.4.1. Materials and methods

Cells from two different families were tested, i.e. hematological and epithelial cells, both in normal and transformed condition. For the hematological compartment, we investigated Huker cells (human keratinocytes) as healthy cells, while human RPMI-7951 cells were chosen as cancer counterpart. Regarding the hematological compartments, we picked monocytes as normal cells and transformed lymphoblasts as cancer cells. All tested cells were used as un-fixed and ethanol fixed samples. Fixed cells were suspended in water, while un-fixed ones were kept in culture medium. Huker cells were grown as monolayer in Dulbecco's Modified Eagle Medium (D-MEM, with glucose 4.5 g/l + 10% Fetal Bovine Serum (FBS) + penicillin and streptomycin 1%). Before reaching confluence, cells were trypsinized and harvested with the standard

methodology and recovered as a cell pellet in 1 ml conic plastic tubes. Sample were than split in two aliquots (of about 3 million cells each one): one was re-suspended in the culture medium (in the follow indicated as Medium 1) and used as un-fixed sample; the other one was washed two times in PBS and fixed in cold (-20 °C) 70% ethanol (for 1 h), then washed and re-suspended in distilled water. THP-1 (normal human monocytes, were grown in suspension in Roswell Park Memorial Institute **(**RPMI) 1640 (with $5x10^{-5}$ M2-mercaptoethanol + FBS 10% + penicillin and streptomycin 1%). Two aliquots of cells were then prepared, one as un-fixed cells in culture medium (indicated as Medium 2) and the other one as ethanol fixed cells, as previously stated for Huker cells.

RPMI-7951, i.e. cells from malignant metastatic melanoma, were grown as monolayer in D-MEM supplemented with 10% Fetal Calf Serum (FCS), 4 mM glutamine, 2 mM Na pyruvate, 100 U/ml penicillin and 0.1 mg/ml streptomycin. Before confluence, cells were treated as described above for Huker cells and the two (un-fixed and fixed) aliquots were obtained. Transformed human were grown in suspension RPMI 1640 medium supplemented with 10% FBS. Aliquots of fixed and un-fixed cells were prepared also in this case.

2.4.4.2. Microscopy analysis of cells distributions

Before proceeding with the interferometric experiments, samples confined into rectangular glass capillaries were analyzed by means of bright field and fluorescence microscopy in order to verify distribution and stability of the biological material filling the channel. Huker and THP-1 cells were used for a preliminary evaluation, being the first one epithelial and, therefore, biologically committed to aggregate, whereas the second is characterized as the largest cells (10-15 μm) in normal blood. Un-fixed cells were stained directly in their culture medium with 1 μg/ml of a supravital dye HO33342 (HO) for 30 min at 37 °C. Fixed cells were stained with 10 μg/ml of Propidium Iodide (PI) for 30 min in distilled water. After staining, cells were spun down and recovered at the bottom of a 1 ml plastic conic tube. The supernatant fluid was carefully aspirated and discarded, leaving a layer of liquid over the cell pellet. Note that RBCs, used only as un-fixed sample, did not require any fluorescent staining, since hemoglobin allows direct observation by bright field microscopy.

As an example, Figure 2.31 shows the microscopy images of capillary samples filled with air and medium and with fixed and un-fixed cells, respectively marked with PI and HO.
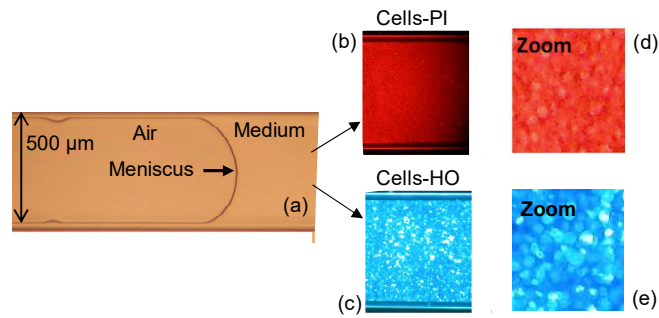
Figure 2.31 Microscopy images taken on capillaries after sample preparation. On the left, (a) typical image in bright field of the reference region filled with air and medium separated by a meniscus. On the right, typical results obtained on regions with cells: (b) fluorescence microscopy image of fixed cells labeled with PI; (c) fluorescence microscopy image of un-fixed cells labeled with HO; (d) zoom of (b) and (e) zoom of (c) for a better visualization of cells.

2.4.4.3. Cells refractive index detection

The borosilicate glass capillaries with rectangular-section channels were used as micro-opto-fluidic devices for gently confining the cells. The microscopy analysis demonstrated the presence of regions (also visible to the naked eye) with different fillings: cells, suspending medium (that was the culture medium for un-fixed cells, water for fixed cells and plasma for RBCs), and air, as shown in Figure 2.31.

We thus performed low-coherence interferometric measurements in various positions along the capillary to obtain the optical path length of the empty channel (air filling), of the channel filled with medium and of the channel filled with cells. Figure 2.32 presents the absolute value (normalized to the peak) of the interferometric signals relative to air (upper trace), culture medium (middle trace), and cell suspension (lower trace). The three traces were collected shining different areas of the capillary, corresponding to the three different fillings. Also in presence of non-homogeneous and highly scattering media as cells, all groups of interferometric fringes were still clearly detectable.
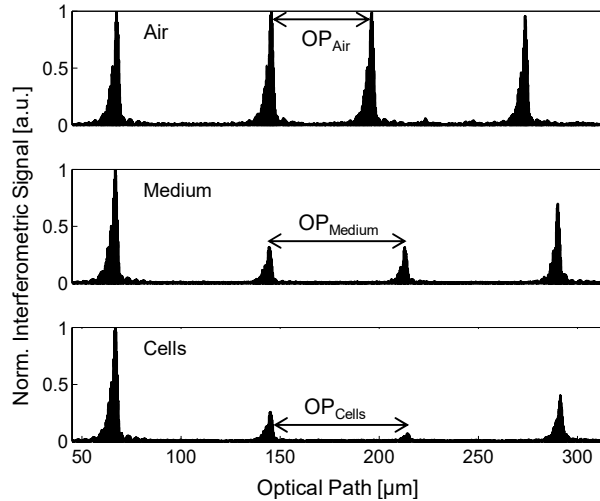
Figure 2.32 Normalized interferometric signal as a function of the optical path obtained on a 50-µm-deep capillary in presence of air (upper trace), culture medium (middle trace) and cells (lower trace). OP_{Air}: optical path length relative to the channel filled with air; OP_{Medium}: optical path length relative to the channel filled with culture medium; OP_{Cells}: optical path length of the channel filled with cells.

After peak detection and OP calculation, the group RI of the various tested fluids and cell populations were obtained as $n_{g,fluid} = OP_{fluid}/OP_{Air}$ (thus, $n_{g,Medium} = OP_{Medium}/OP_{Air}$ and $n_{g,Cells} = OP_{Cells}/OP_{Air}$). In all cases, we calculated the average and standard deviation on data from three repeated measures, also performed on different capillary samples. As the relative position of the peak of the fringe group can be determined with a resolution better than $\lambda/16 = \pm 1.550$ µm/16 $= \pm 0.097$ µm, RI differences dn = dOP/$\pm$ 0.097 µm $= \pm 0.002$ RIU were detectable. The stage velocity was set to 5 µm/s, allowing a 0.097 µm displacement to be performed in 0.02 s, corresponding to 480 data samples with a 24-kHz sampling frequency.

Figure 2.33 shows four graphs with the RI experimental values obtained on the four cell lines (two with epithelial origin and two with hematological origin) as well as on their suspending medium (i.e., water or Medium 1 and 2). Two graphs show the values obtained when considering fixed cells (a, b) and the others report the values obtained for un-fixed cells (c, d). These results clearly indicate that the RI of the cell suspension is always higher than that of the medium. Moreover, a difference between the average RI of the samples containing normal and transformed (malignant) cells, also mentioned in the literature [107] was observed.

55
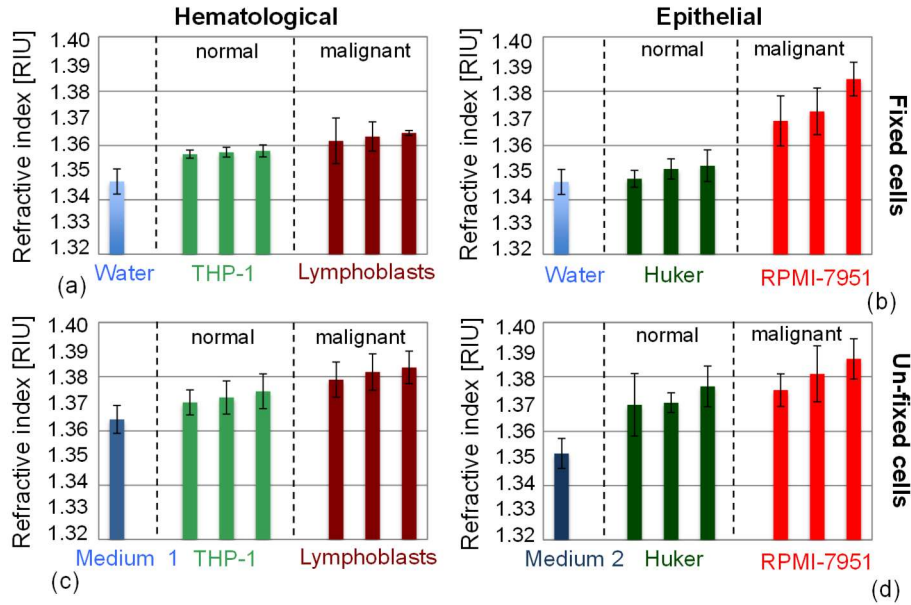
Figure 2.33 Column bar graphs with average and standard deviation values of RI obtained for four different cell lines and the medium in which they are suspended (i.e., water, Medium 1 or 2). Each graph compares RI values of normal and malignant cells with the same origin. (a,b) Fixed cells; (c,d) Un-fixed cells; (a,c) Hematological cells; (b,d) Epithelial cells.

In order to investigate the statistical significance of the observed difference, we applied a one-sided Mann-Whitney test [123], and obtained p-values < 0.05. In particular, we obtained $p = 0.04 \cdot 10^{-3}$ for fixed Lymphoblasts versus THP-1 and $p = 0.02 \cdot 10^{-3}$ for fixed RPMI versus Huker; in the case of un-fixed cells, we calculated $p = 0.04 \cdot 10^{-3}$ for Lymphoblasts versus THP-1 and $p = 19 \cdot 10^{-3}$ for RPMI versus Huker. Despite the heterogeneity of the samples, the reported values seem to witness a statistical difference between the average RI values of transformed versus normal cells, even if it should be recognized that we are here reporting only preliminary results and the p-values were calculated on data ensembles of small size. It is worthy to underline here that the arrangement of the cells inside the tested volume is random, so the measured optical path length does not correspond to a preferred axial direction of the cell. Cells are randomly oriented inside the tested volume as they are not grown adherent to the walls of the capillary.

For further validation of the obtained results, more cells samples should be analyzed. In order to obtain more data, a useful development would consist in the automatic performance of the optical measurements in several positions of the capillary, in order to have average data on a sufficient number of cells. Beside cells RI detection, the proposed method, based on a low-power infrared read-out beam, thus minimally invasive, can be potentially applied to the detection of group RI of various non-homogenous biological fluids. Moreover, as micro-capillaries can also be used as flow-through devices, it would in principle also be possible to

detect in real time the response of a group of cells or different biological samples to environmental changes induced in the capillary itself. Consequently, the presented method could be exploited in the field of drug discovery, for examining the changes in RI of a cell population to various physical and biochemical stimuli, or for sample pre-screening.

In general, biomedical research is often characterized by the requirement of sophisticated, complex and expensive instrumentation [124], that is sometimes unavailable in laboratories. On the other hand, routine applications in the same field will benefit from more compact and less expensive instrumental configurations, such as the one that we have proposed. This is the case for the example of marine biology (specifically in water pollution) where bacteria and algae may be differentiated on the basis of the RI [125] , [126].

Additionally, another emerging area of future applications to be considered is the wide field of allergology, where target cells, once activated by specific agents, immediately respond with macromolecular events located on the cell surface and shrinkage of the whole cell body. More specifically, the so-called "heavy metal" ions (and, among others, the Ni++) play a crucial role in the industry of cosmetics where a large number of specific tests are required to monitor the presence/absence of these metal ions; currently, the molecular steps are monitored by means of immuno-fluorescence cell labeling and flow cytometry. Evaluation of body size variations is usually performed by detecting FSC [110] [127] [128], and is thus an improvement in terms of reagent saving, but still time-consuming and costly. The close relation between FSC and RI [129] (detected also on fixed samples) will open new horizons in routine analyses in the drug discovery field. A further advantage of this method consists of its applicability on fixed biological samples; thus, samples can be collected, stored and analyzed later on, even in a different location.

In conclusion, we demonstrated the applicability of low-coherence interferometry based on a Michelson configuration to investigate multilayers structures in different material, such as glass and polymers. An all-fiber reconfigurable setup was employed to detect the RI of solutions inserted into the channel of off-the-shelf disposable devices easily interfaced to an external fluidic system. Refractometric measurements were performed remotely employing read-out sources in the near infrared, thus in a region of minimum absorption, and consequently minimum invasiveness, for biological tissues. The internal micrometric dimension of the employed devices allowed to work with low quantities of material, in the order of μl. The system was demonstrated suitable to the RI detection of homogenous fluids as well of highly scattering fluids such as population of cells. Implementation of temperature control could bring a significant improvement.

Chapter **3**

Refractive index sensing based on spectral reflectivity and transmissivity measurements

In this Chapter, the reconfigurable system is presented with the alternative arrangement set for spectral detection of RI variations. In the first section, the principle of operation and the theoretical background of the proposed RI sensing technique are presented. Then, I will report theoretical results obtained through numerical simulations and experimental results collected on capillaries with different sizes. Finally, the impact of the capillary dimension on the final sensor performances are discussed. A selection of these results has been published in [130].

3.1. Rectangular glass micro-capillaries as optical transducers with spectral read-out: theoretical background

3.1.1. Principle of operation

A rectangular glass micro-capillary can be viewed as a three-layered optical structure, composed by the front wall, the gap, and the back-wall. When broadband radiation is shined orthogonally to one of its flat long side, light is partially reflected and partially transmitted at each interface given by a change of material, and thus RI, along the longitudinal dimension. The back-reflected signal exhibits wavelength regions of high reflectivity separated by deep reflectivity notches. The same occurs for the transmitted signal, where transmitted minima will correspond to reflectivity

maxima and vice versa. The shape of the transmitted and reflected spectra depends on the geometric structure of the crossed device and on the RI of the composing layers. As the fluid under test can flow through the capillary channel, rectangular glass micro-capillaries can be considered as liquid-core optical cavities. Consequently, the position of the maxima (and minima) of the reflected (and transmitted) spectra depend not only on the capillary size but also on the RI of the media filling the channel. As the RI of the filling media increases, spectra minima (and maxima) are expected to shift toward longer wavelengths. This mechanism can be employed to detect the RI change of fluids flowing inside the capillary with respect to a reference fluid with known RI. The described structure represents fundamentally a multilayer Fabry-Pérot cavity. In the subsequent sections, the theoretical behavior of a single glass layer as Fabry-Pérot Etalon is introduced. Then, a multilayer structure like the rectangular micro-capillary is analyzed, and analytical expressions of the transmitted and reflected spectra are found. Numerical simulations exploiting these analytical results are subsequently performed to investigate the impact of various parameters on the sensor response.

3.1.2. Single glass layer as Fabry-Pérot Etalon

A Fabry-Pérot interferometer, also called Fabry-Pérot Etalon, is a device composed by two highly reflective surfaces, parallel between each other, divided by a gap.
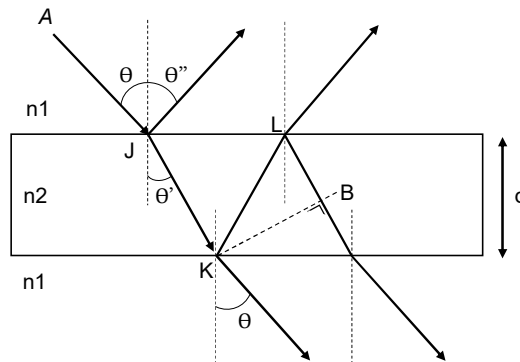
Figure 3.1 Representation of multiple reflections and refractions occurring as light impinges on a slab of RI n_2 surrounded by a medium of RI n_1.

As a plane wave with amplitude A is shined on one of its flat faces, it will be partially reflected and partially refracted at the interfaces separating two media. Transmitted light will again undergo the same process, and light will be reflected and refracted multiple times. This will lead to the creation of secondary reflected and transmitted beams of decreasing intensity. Multiple beam interference will consequently occur, resulting in

sharp interference peaks, in principle leading to a high resolution. In comparison, a Michelson interferometer is based on the observation of the interferometric pattern resulting by the interference of just two beams. A single glass layer is a very simple structure that can be modeled as a Fabry-Pérot Etalon, a schema is shown in Figure 3.1 [131]. Let's consider a glass layer of thickness d, and RI n_2, surrounded by a medium of RI n_1 (if the medium is air, $n_1 \sim 1$ RIU). We assume a plan wave of amplitude A incident on the glass slab with an angle θ to the normal at the point J. Part of the incident light will be reflected (with an angle θ'') while part will be refracted into the glass layer with an angle θ'. The angles θ' and θ'' are easily obtainable from θ through the Snell's law, expressed as:

$$n_1 \sin \theta = n_2 \sin \theta' \qquad (15)$$

$$\theta = -\theta'' \qquad (16)$$

The refracted beam will then reach the second interface between the two dielectric interfaces in the point K, where part of the field will be again reflected back into the glass, with an angle θ', and part will be refracted into the medium with RI equal to n_1 with angle θ. This process will occur multiple times, leading to the creation of reflected and refracted beams of decreasing intensities. Having travelled for different paths, the various beams will accumulate a phase difference, proportional to the covered geometrical travel and to the RI of the crossed media. Consequently, depending on their phase difference, the beams will interfere in a constructive or destructive way, also depending on the wavelength of light. The phase difference between two consecutive transmitted beams can be obtained starting from the geometrical path difference, definable as

$$p = KL + LB \qquad (17)$$

where

$$LB = KL \cos 2\theta' \qquad (18)$$

Combining the two equations, we have

$$p = KL(2 \cos^2 \theta') \qquad (19)$$

Considering $d = KL \cos \theta'$, and multiplying the geometrical path by the medium RI n_2 we finally retrieve the optical path distance between two consecutive beam as

$$\delta = 2n_2 d \cos \theta' \qquad (20)$$

This path difference consequently leads to a phase shift equal to

$$\emptyset = \frac{2\pi}{\lambda}\delta = \frac{4\pi}{\lambda}n_2 d \cos\theta' \qquad (21)$$

where λ is the wavelength of light in vacuum. The distance between two reflected beams can be easily found equal to what already calculated for transmitted beams.

Considering the air-glass interface, we can write the reflection and transmission coefficients for the perpendicular polarization s as:

$$r_s = \frac{n_1\cos\theta - n_2\cos\theta'}{n_1\cos\theta + n_2\cos\theta'} \qquad (22)$$

$$t_s = \frac{2n_1\cos\theta}{n_1\cos\theta + n_2\cos\theta'} \qquad (23)$$

and for the parallel polarization p

$$r_p = \frac{n_1\cos\theta' - n_2\cos\theta}{n_1\cos\theta' + n_2\cos\theta} \qquad (24)$$

$$t_p = \frac{2n_1\cos\theta}{n_1\cos\theta' + n_2\cos\theta} \qquad (25)$$

where $r = E_r/E_i$, field reflectivity and $t = E_t/E_i$, field transmissivity. In case of normal incidence ($\theta = 0°$), polarization does not count and the field Fresnel coefficients reduce to:

$$r_{12} = \frac{n_1 - n_2}{n_1 + n_2} \qquad (26)$$

$$r_{21} = -\frac{n_1 - n_2}{n_1 + n_2} \qquad (27)$$

$$t_{12} = \frac{2n_1}{n_1 + n_2} \qquad (28)$$

$$t_{21} = \frac{2n_2}{n_1 + n_2} \qquad (29)$$

The coefficient in energy, i.e. the reflectivity R and the transmissivity T, can be obtained as

$$R = r_{12}{}^2 = r_{21}{}^2 \qquad (30)$$

$$T = t_{12}t_{21} \tag{31}$$

In general, R and T depend on the light polarization, and if no absorption occurs at the interfaces, we have R + T = 1.
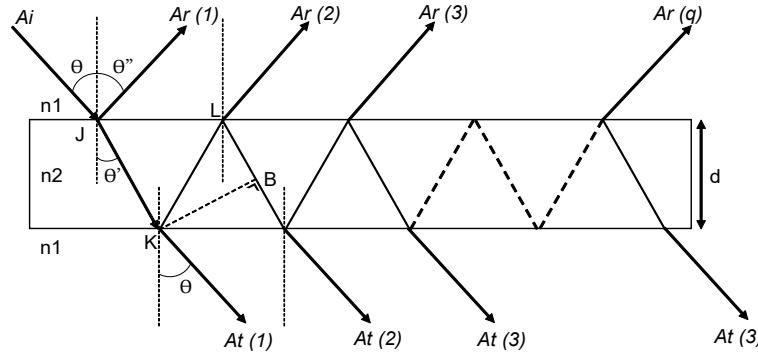
Figure 3.2 Representation of multiple transmitted and reflected beams from a slab of RI n_2 surrounded by a medium of RI n_1.

Let's consider the picture in Figure 3.2. As previously stated, the plane wave of amplitude Ai impinging on the glass slab will be reflected and transmitted N times, with $N \rightarrow \infty$. If we follow the multiple reflections process, we obtain

$$A_t(1) = t_{12}t_{21}A_i \tag{32}$$

$$A_t(2) = t_{12}t_{21}r_{21}{}^2e^{i\emptyset}A_i \tag{33}$$

....

$$A_t(q) = t_{12}t_{21}r_{21}{}^{2(q-1)}e^{i(q-1)\emptyset}A_i \tag{34}$$

Being A_t(q) the complex amplitude of the qth transmitted beam. Similarly, we can find

$$A_r(q) = t_{12}r_{21}{}^{2q-3}t_{21}e^{i(q-1)\emptyset}A_i \tag{35}$$

The amplitude of the transmitted wave is the sum of all transmitted beams over q (for q from 1 to ∞), and, by applying the identity $\sum_{q=0}^{\infty}r^q = \frac{1}{1-r}$, we find

$$A_t = \frac{t_{12}t_{21}e^{-2i\emptyset}}{1 - r_{12}{}^2e^{-i\emptyset}} * A_i \tag{36}$$

63

In a similar way, we can retrieve the amplitude of the reflected wave, equal to

$$A_r = \left(r_{12} + \frac{t_{12}t_{21}r_{21}e^{i\emptyset}}{1 - r_{21}{}^2 e^{i\emptyset}} \right) * A_i \tag{37}$$

$$\mathbf{T} = \frac{I_t}{I_i} = \frac{A_t A_t{}^*}{A_i A_i{}^*} = \left| \frac{A_t}{A_i} \right|^2 = \frac{1}{1 + F \sin^2 \frac{\emptyset}{2}} \tag{38}$$

$$F = \frac{4R}{(1 - R)^2} \tag{39}$$

$$\mathbf{R} = \left| \frac{A_r}{A_i} \right|^2 = \frac{\sin^2 \frac{\emptyset}{2}}{1 + F \sin^2 \frac{\emptyset}{2}} \tag{40}$$

Based on Eq. 38 and 40, reflectivity R and transmissivity T are periodic with period 2π. The distance between two consecutive maxima, or minima, of the periodic function, is known as the Free Spectral Range (FSR). In terms of wavelength, if we consider two consecutive transmission peaks occurring at λ_1 and λ_2, we have

$$\lambda_1 = \frac{2n_2 h cos\theta'}{m} \tag{41}$$

$$\lambda_2 = \frac{2n_2 h cos\theta'}{m + 1} \tag{42}$$

where m is an integer. If m is large, from Eq. 41 and 42 we obtain:

$$\Delta\lambda_{FSR} \approx \frac{2n_2 h \cos\theta'}{m^2} = \frac{\lambda_1{}^2}{2n_2 h \cos\theta'} \tag{43}$$

that for small angles of incidence it reduces to

$$\Delta\lambda_{FSR} = \frac{\lambda^2}{2n_2 h} \tag{44}$$

3.1.1. Micro-capillary as multilayer structure: analytical expression of reflectivity and transmissivity

In the previous paragraph, we described the principle of operation of a simple Fabry-Pérot Etalon composed by single glass slab. Let's know consider a more complex situation involving a rectangular glass micro-capillary. When this kind of device is shined with a light beam orthogonally to its long flat surface, the radiation encounters four different reflective interfaces, as described in Figure 3.3: an air-glass interface, corresponding to the beginning of the front wall, a glass-channel interface, where the channel RI depends on the capillary filling medium, a channel-glass interface, and finally a glass-air interface, corresponding to the end of the capillary. At each of these interfaces, light is partially reflected and partially transmitted, and the phenomenon is again describable by means of the Fresnel equations introduced in the previous section. Even though the reflectivity of 2D and 3D structure is often calculated by transfer matrix methods, in this case a simpler approach based on electromagnetic field propagation can be suitable. In fact, being the width and length of the capillary always bigger than the diameter of the impinging light beam, the capillary can be considered as a multilayer structure composed by alternating dielectric materials with different RI and thickness along a single axis. In this condition, electric field propagation across the capillary can be modeled as a cascade of Fabry-Pérot Etalons.
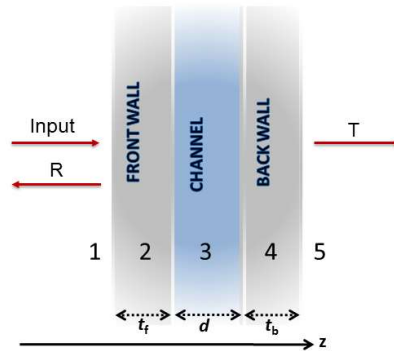
Figura 3.3 Schema of capillary interfaces.

Starting by considering the layer of the back glass wall of the capillary, we can identify two interfaces: 3–4 between channel (3) and back glass wall (4) and 4–5 between back glass-wall (4) and air (5). We assume that t_b is the thickness of the back wall, n_{glass} is the RI of glass, n is the RI of the fluid in the channel and $n_{air} = 1$ RIU. We also assume a plane wave propagating in the z-direction perpendicular to the interfaces. If we define the field reflection (r) and transmission (t) coefficients for the wave

propagating through the interfaces, starting by considering the layer of the back glass-wall of the capillary, we can write:

$$r_{3-4} = \frac{n - n_{glass}}{n + n_{glass}} = -r_{4-3} \tag{45}$$

$$r_{4-5} = \frac{n_{glass} - n_{air}}{n_{glass} + n_{air}} = \frac{n_{glass} - 1}{n_{glass} + 1} \tag{46}$$

$$t_{3-4} = \frac{2n}{n + n_{glass}} \tag{47}$$

$$t_{4-3} = \frac{2n_{glass}}{n + n_{glass}} \tag{48}$$

$$t_{4-5} = \frac{2n_{glass}}{n_{air} + n_{glass}} = \frac{2n_{glass}}{1 + n_{glass}} \tag{49}$$

then, the electric field reflection coefficient r₃₋₄' of the whole back glass-wall, considered as an overall equivalent interface 3-4', can be calculated as:

$$r_{3-4'} = r_{3-4} + \frac{t_{3-4}t_{4-3}r_{4-5}\, e^{(-j2kn_{glass}t_b)}}{1 - r_{4-3}r_{4-5}e^{(-j2kn_{glass}t_b)}} \tag{50}$$

and the electric field transmission coefficient $t_{3-4'}$ of the whole back glass-wall can be calculated as:

$$t_{3-4'} = \frac{t_{3-4}t_{4-5}e^{(-jkn_{glass}t_b)}}{1 - r_{4-3}r_{4-5}e^{(-j2kn_{glass}t_b)}} \tag{51}$$

where k = 2π/λ. By iteratively computing the electric field reflection and transmission coefficients in the backward direction with respect to the incident wave, the overall reflectivity and transmissivity of the capillary can be calculated. By considering the layer of the capillary channel, we can now identify two interfaces: 2-3 between front glass-wall (2) and channel (3) and 3-4' between channel (3) and equivalent medium 4'. We assume here that d is the channel depth. The electric field reflection coefficient $r_{2-3'}$ at the overall equivalent interface 2-3' is given by:

$$r_{2-3'} = r_{2-3} + \frac{t_{2-3}t_{3-2}r_{3-4'}\, e^{(-j2knd)}}{1 - r_{3-2}r_{3-4'}\, e^{(-j2knd)}} \tag{52}$$

and the electric field transmission coefficient $\tau_{2-3'}$ is given by:

$$t_{2-3'} = \frac{t_{2-3}t_{3-4'} \ e^{(-jkd)}}{1 - r_{3-2}r_{3-4'} \ e^{(-j2kd)}} \tag{53}$$

where

$$r_{2-3} = \frac{n_{glass} - n}{n + n_{glass}} = -r_{3-2} \tag{54}$$

$$t_{2-3} = \frac{2n_{glass}}{n + n_{glass}} \tag{55}$$

$$t_{3-2} = \frac{2n}{n + n_{glass}} \tag{56}$$

Finally, assuming that t_{f} is the thickness of the front wall, in analogy with the previous steps, the electric field reflection coefficient of the whole capillary $r_{1\text{-}2'}$ is given by:

$$r_{1-2'} = r_{1-2} + \frac{t_{1-2}t_{2-1}r_{2-3'} \ e^{(-j2kn_{glass}t_f)}}{1 - r_{2-1}r_{2-3'} \ e^{(-j2kn_{glass}t_f)}} \tag{57}$$

and the electric field transmission coefficient of the whole capillary $t_{1\text{-}2'}$ is given by:

$$t_{1-2'} = \frac{t_{1-2}t_{2-3'} \ e^{(-jkn_{\,glass}t_f)}}{1 - r_{2-1}r_{2-3'} \ e^{(-j2kn_{\,glass}t_f)}} \tag{58}$$

where

$$r_{1-2} = \frac{n_{air} - n_{glass}}{n_{air} + n_{glass}} = \frac{1 - n_{glass}}{1 + n_{glass}} = -r_{2-1} \tag{59}$$

$$t_{1-2} = \frac{2n_{air}}{n_{air} + n_{glass}} = \frac{2}{1 + n_{glass}} \tag{60}$$

$$t_{2-1} = \frac{2n_{glass}}{n_{air} + n_{glass}} = \frac{2n_{glass}}{1 + n_{glass}} \tag{61}$$

The spectral reflectivity R can be then obtained by plotting $|r_{1\text{-}2'}|^2$ as a function of the wavelength λ as the spectral transmissivity T is obtained by plotting $|t_{1\text{-}2'}|^2$ as a function of the wavelength λ.

3.1.4 Numerical evaluation of sensor functionality and performances

In order to understand the theoretical behavior of the proposed sensor for RI detection, we performed numerical simulation through MATLAB software based on the Fresnel analytical equations introduced in the precedent section. The described method was firstly applied to the estimation of the reflectivity spectrum alone [131] [133]. Here, both transmission and reflection coefficients for the electric field travelling with normal incidence through the device were recursively obtained starting from the back wall/air interface. Overall optical power transmissivity and reflectivity were then separately calculated. Finally, the T/R ratio was retrieved. Glass RI dependence on the wavelength was taken into account. Glass RI values were obtained through interpolation of data obtained from the literature for BOROFLOAT® Schott Glass [88]. No wavelength dependence, instead, was considered for the capillary filling fluids, because of the complexity of finding reliable values in the literature. With the explained method, we firstly separately obtained the overall optical power reflected and transmitted by the capillary. The result is shown in Figure 3.4.
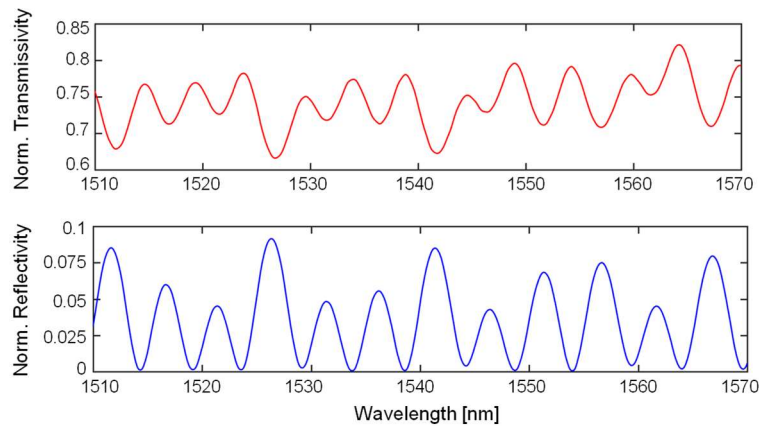
Figure 3.4 Theoretical spectra calculated through numerical simulations based on Fresnel equation for a capillary with $t_f=t_b=d=50$ μm filled with water (n_{water}=1.3154 RIU). Upper red trace: normalized transmissivity. Blue lower trace: normalized reflectivity. A moving average has been applied to numerical spectra to mimic the limited resolution bandwidth of the Optical Spectrum Analyzer employed in the experimental verifications.

The theoretical spectra are shown on a wavelength interval between 1.51 and 1.57 μm, since this band was also experimentally analyzed, for a capillary with $t_f=t_b=d=50$ μm and assuming water ($n_{fluid} = 1.3154$ RIU) as the channel filling fluid. As theoretically expected, transmissivity maxima correspond to reflectivity minima, and vice versa. A moving average has been applied to numerical spectra to mimic the limited resolution

bandwidth of the OSA later employed in the experimental verifications. Then, to observe the response of the device to flowing media RI changes, we performed numerical simulations for increasing RI values of the fluid inside the channel. Figure 3.5 shows the T/R spectra, calculated as the ratio between the obtained transmissivity T and reflectivity R, for three different RI values.

It can be observed that, as the RI of the filling media increases, the T/R spectrum undergoes a clear shift toward longer wavelengths. The $\Delta\lambda$ highlighted in the picture represents the distance, in terms of wavelength, between two consecutive maxima of the T/R spectrum. It is an important parameter of multiple optical resonances devices since it defines the maximum wavelength shift that can be followed without ambiguity, and thus the maximum exploitable RI change. It is interesting to notice that the spectra don't shift in a rigid way: indeed, peaks facing a larger $\Delta\lambda$ appear to undergo a wider translation, compared to others, given the same RI change. Moreover, in Figure 3.5, a change in the peak intensity can be observed. This phenomenon can be explained as follows: the amplitude of the peaks depends on the interference between optical fields reflected (and transmitted) at each interface. When the RI of the solution inserted in the capillary is changed, the phase cumulated by the field travelling through the capillary channel changes, as a consequence of the RI variation; consequently, the interference effect among all reflected/transmitted contributions yields a different overall amplitude. Additionally, another effect impacts on the intensity variation: when a fluid is inserted into the capillary, the RI step between the glass walls and the gap filling media decreases, causing a further change in the amplitude of reflected and transmitted fields.
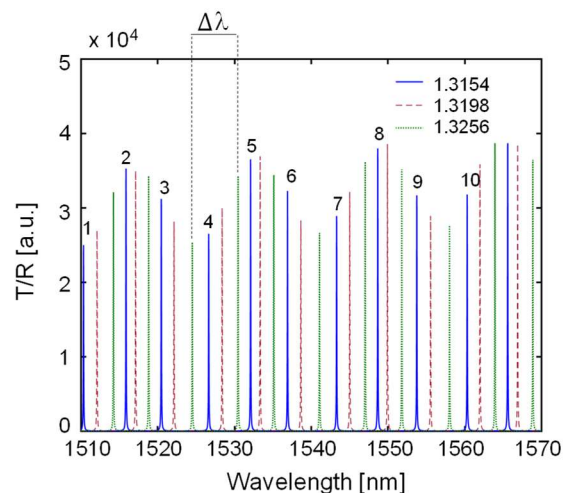
Figure 3.5 Numerical spectra obtained for a capillary with $t_f=t_b=d=50$ µm and increasing RI of the filling media. Blue solid trace: $n_{fluid}=1.3154$ RIU, red dashed trace: $n_{fluid}=1.3198$ RIU, green dotted trace: $n_{fluid}=1.3256$ RIU. $\Delta\lambda$: distance in terms of wavelength between two consecutive peaks of the same spectrum.

As explained in Paragraph 3.1.1, spectra result from the superimposition of contributes coming from different cavities and interfaces. In order to understand the contribution given by each layer, we performed the Fast Fourier Transform (FFT) of the numerical spectrum obtained for a capillary with $t_f=t_b=d=50$ μm in presence of water inside the capillary (i.e. the spectra represented by the blue solid trace in Figure 3.5). For the FFT calculation, we considered a wavelength interval between 1.4 and 1.6 μm. Figure 3.6(a) shows the obtained result: three main peaks are clearly identifiable, occurring at $1/\lambda_1= 65$ μm^{-1}, $1/\lambda_2= 125$ μm^{-1}, $1/\lambda_3= 190$ μm^{-1}.

From the theory, we know that the FSR for a Fabry-Pérot Etalon can be calculated through the relationship $FSR = \lambda^2/(2 \bullet OP)$, where OP is the optical path seen by the light when travelling through a specific cavity and λ the wavelength of the considered resonance. When the light travels through the capillary, it encounters not only the cavity composed by a single layer, i.e. the walls and the channel, but also composite cavities given by the superimposition of two or more single cavities. In particular, we can recognize the cavity given by the whole capillary and by one wall plus the channel. Considering these layers, we can calculate $OP_{wall} = n_{glass} \bullet t$, $OP_{channel} = n_{fluid} \bullet d$ (with $n_{fluid}= 1.3154$ RIU for water), $OP_{capillary}= n_{fluid} \bullet d + n_{glass} \bullet (t_f + t_b)$ and $OP_{wall+channel} = n_{glass} \bullet t_f + n_f \bullet d$, where at $\lambda=1.549$ μm we have $n_{glass} =1.4561$ RIU [88]. From these values, we obtain $FSR_{wall}=16.5$ nm, $FSR_{channel}=18.3$ nm, $FSR_{wall+channel}=8.7$ nm and $FSR_{capillary}=5.7$ nm. Just taking their inverse, it's easy to see that (with reference to Figure 3.6(a)) $1/\lambda_1 \approx 1/FSR_{wall} \approx 1/FSR_{channel}$, $1/\lambda_2 \approx 1/FSR_{wall+channel}$ and $1/\lambda_3 \approx 1/FSR_{capillary}$. Since the FSR depends on the wavelength, the mode spacing doesn't remain uniform along all the considered wavelength range; as a consequence, at $1/\lambda_2$ and $1/\lambda_3$ the Fourier spectrum appears broader. Figure 3.6(b) shows the FFT of a numerical spectra relative to a capillary with $t_f=t_b=125$ μm and $d=50$ μm. In this case, given the different dimension of walls thickness and channel depth, the peaks relative to the channel and the walls are separately identifiable. Since the channel depth is unaffected with respect to the previous case, the peak occurring at $1/\lambda_1 \approx 1/FSR_{wall}$ is still identifiable in the same position, while the remaining peak appear shifted toward higher wavenumber values, where $1/\lambda_2 \approx 1/FSR_{wall}$, $1/\lambda_3 \approx 1/FSR_{wall+channel}$ and $1/\lambda_4 \approx 1/FSR_{capillary}$.

As the aim of this study was to recover the RI of capillary filling fluids, we calculated numerical T/R spectra for increasing RI values, in the range between 1.3154 RIU (n_{water}) and 1.3299 RIU (corresponding, as an example, to a solution of glucose in water at a concentration of 10% [w/V]). Glucose RI values were obtained through the relationship $n = n_0 + \alpha \bullet C$ [85], where n_0 is the RI of the solution solvent (here water), C is the concentration of the solute and α is the RI increment, specific for each substance, defined as dn/dC. In case of glucose, $\alpha = 0.145$ g/cm^3 [86]. The RI interval considered in the simulations was chosen in order to obtain the largest T/R shift occurring within the given $\Delta\lambda$, i.e. the maximum RI change exploitable without ambiguity.
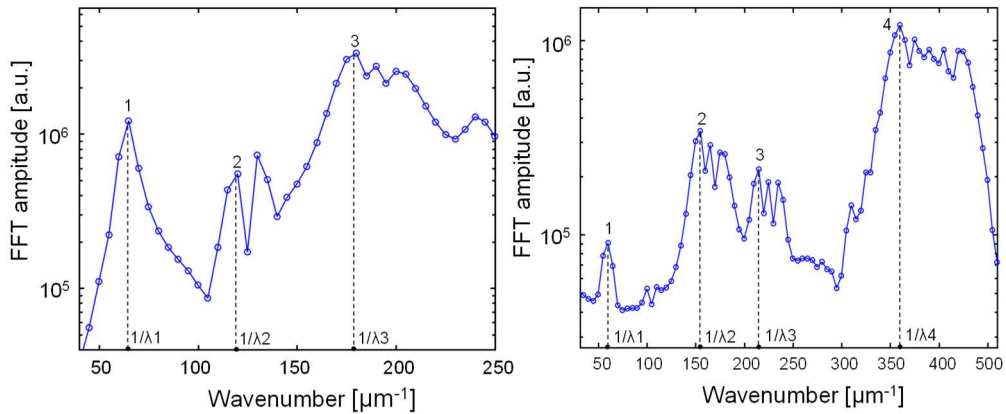
Figure 3.6 Fast Fourier Transform relative to a numerical T/R spectrum
obtained (a) for a capillary with $t_f=t_b=d=50$ μm (blue solid trace in Figure
3.5.) and (b) for a capillary with $t_f=t_b=125$ μm and $d=50$ μm, both filled
with water ($n_{fluid}=1.3154$ RIU).

The position of each T/R spectra maxima was monitored, and, reporting
the corresponding wavelength values as a function of the filling media RI,
we obtained the theoretical calibration curves reported in Figure 3.7. Data
were linearly fitted through last square method to obtain the sensitivity of
each resonance, defined as $S = d\lambda_{max}/dn_{fluid}$. Sensitivities values are
reported on the right side of the graph. In can be noticed as different
sensitivity values were obtained for different spectra resonances.
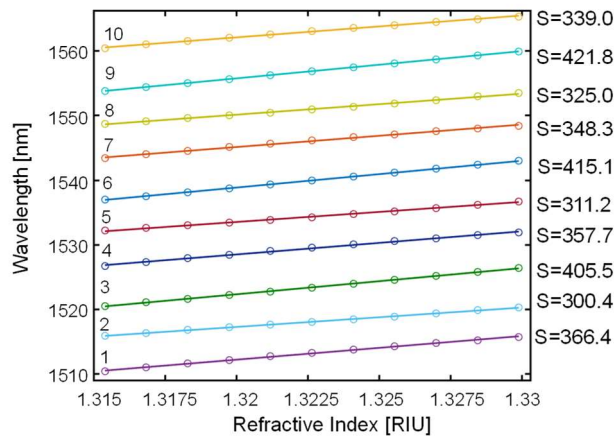
Figure 3.7 Calibration curves obtained from theoretical T/R spectra for a
capillary with $d=t_b=t_f=50$ μm and n_{fluid} in the range of 1.3154-1.3299 RIU.
Numerical values on the right side represent the sensitivities obtained
through linear fitting of the data, reported in nm/RIU units. The numbers
reported near each fitting line recall the peak labels highlighted in Figure
3.5.

Given the fact that the final spectrum results from the superimposition of contributes coming from different cavities, where just the channel represents the sensing one, it could be pointed that channel modes would be the most suitable for sensing purposes; Morrish et al. [66], for example, monitored the shift of channel modes of spectra transmitted through mirrored round glass capillaries as the RI of the filling media increased. Anyway, they were using capillaries with walls thickness much bigger than the channel depth. In our case, channel and walls are of the same size, or of the same order of magnitude: for this reason, it was not possible to label each resonance on the T/R spectrum as coming from a specific interface. On the opposite, each resonance has to be considered as the superimposition of the contributions given by different cavities, where the distance $\Delta\lambda$ between different spectra maxima doesn't equal any of the calculated FSR. Higher sensitivities values obtained for some of the resonances are probably due to a stronger contribution of those components coming from the channel in defining those spectra maxima. To better show this concept, we performed additional numerical simulations, which results are reported in Figure 3.8.
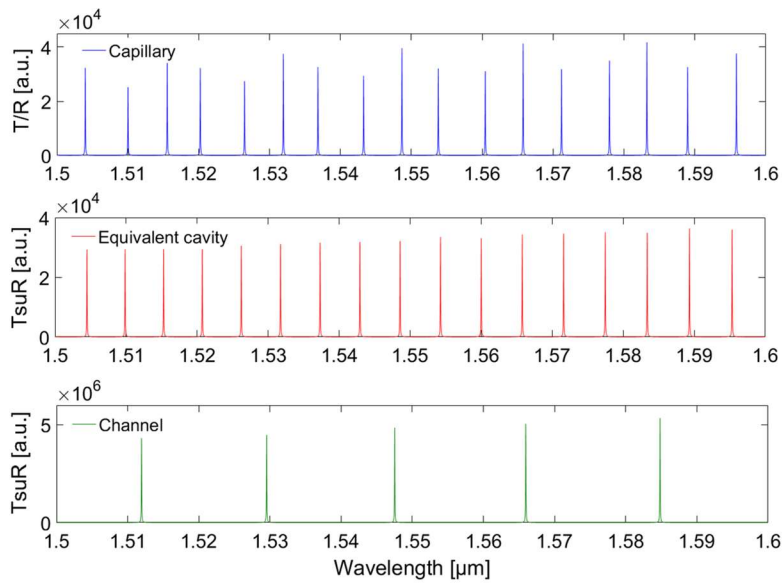
Figure 3.8 Theoretical T/R spectra obtained (a) for a capillary with $t_f=t_b=d=50$ µm filled with water, (b) for a single glass slab with a thickness yielding a total optical path length equal to that of the whole capillary filled with water but only two air-glass interfaces, (c) when considering just the boundaries and the cavity relative to the channel filled with water.

Figure 3.8(a) reports the theoretical T/R spectrum obtained for a capillary with $t_f=t_b=d=50$ µm filled with water, whereas Figure 3.8(b) shows the theoretical T/R spectrum obtained for a single glass slab with a thickness yielding a total optical path length equal to that of the whole capillary filled with water but only two air-glass interfaces. Figure 3.8(c),

72

instead, shows the T/R spectrum obtained when considering just the boundaries and the cavity relative to the channel filled with water. Apparently, the spectra in Figure 3.8(a) and Figure 3.8(b) are similar: it can be noticed as the spectrum in Figure 3.8(b) has the same number of peaks as the one in Figure 3.8(a). However, in the spectrum in Figure 3.8(b) the distance between two consecutive resonances is constant, differently from what happens for the spectrum in Figure 3.8(a). Performing the FFT of the spectrum in Figure 3.8(b), as expected, we found just one peak at $1/\lambda=190\ \mu m^{-1}=1/FSR_{capillary}$. In Figure 3.8(c), instead, the number of resonance peaks is clearly lower, and the spacing is the one expected for the capillary channel filled with water. It can be noticed as the peak positions anyway don't perfectly match with the ones in Figure 3.8(a). From the reported results, it appears that it is not possible to label the resonances as coming from a specific boundary, since each peak appears to be the result of the contributions coming from different cavities and boundaries. This superposition is probably a consequence of the fact that we are considering capillaries with channel depth and walls thickness of the same order of magnitude. Similar results were found by performing numerical simulations on asymmetric capillaries, with channel depth of 50 μm but thinner walls, though of the same order of magnitude.

As stated before, rectangular glass micro-capillaries are disposable devices available in a wide range of dimensions for what concerns the channel depth and walls thickness. It is interesting to understand how device dimensions could impact on its performance for RI sensing. For this reason, we calculated numerical T/R spectra for capillaries with fixed channel depth, set equal to 50 μm, but different walls thicknesses, and increasing filling media RI. In particular, we considered capillaries with walls in the range of 20 μm to 110 μm. Intuitively, as spectra resonance includes reflections components due to the walls, we would expect that the smaller is their dimension compared to the total capillary optical thickness, the higher should be the obtainable sensitivity. This is a consequence of the fact that the sensing part of the device is just represented by the capillary channel. Thus, we defined a parameter $D = d\ /\ [d+n_{glass}\bullet (t_f +t_b)]$, where n_{glass} is the glass RI and $n_{glass}\bullet t$ represents the optical path travelled by light when crossing the glass walls. Then, we retrieved the calibration curves and the resonance sensitivity for each combination of geometrical parameters, and reported the maximum obtained sensitivity (S_{max}) for each capillary structure as a function of its characterizing D. Simulations were performed in the wavelength interval between 1400 and 1600 nm. The results are shown in Figure 3.9. It can be noticed as higher D values corresponds to higher values of best achievable sensitivities. The relationship between the two variables is in good approximation linear, with a correlation coefficient R=0.997. Data reported in Figure 3.9 have been obtained considering in the simulations $t_f=t_b$ and both equal to 20 μm, 27.5 μm, 35 μm, 50 μm, 65 μm, 80 μm, 95 μm, 110 μm, resulting in D

equal, respectively, to 0.462, 0.384, 0.329, 0.256, 0.209, 0.178, 0.153, 0.135 (with n_{glass} = 1.4561 RIU).
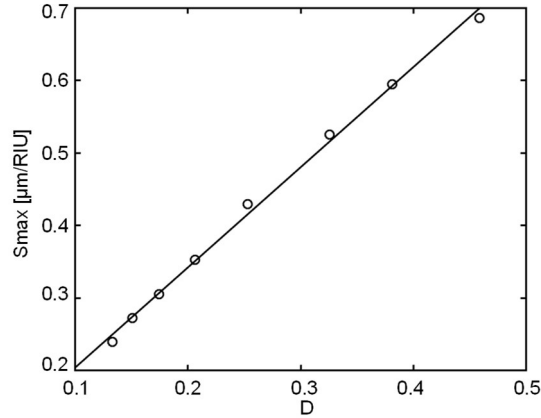
Figure 3.9 Best achievable sensitivities obtained from T/R theoretical spectra calculated for channel depth d = 50 µm and different wall thicknesses (from 20 µm up to 110 µm) as a function of $D = d/[d+n_{glass}\bullet(t_f+t_b)]$, where t_f is the front wall thickness and t_b the back wall thickness.

3.2. Instrumental configuration for T/R spectral measurements

Figure 3.10 shows the specific instrumental configuration employed to perform spectral reflectivity measurements. Technical details about several passive components, such as the optical fibers, the couplers, and the lenses, were already provided in Paragraph 1.3.
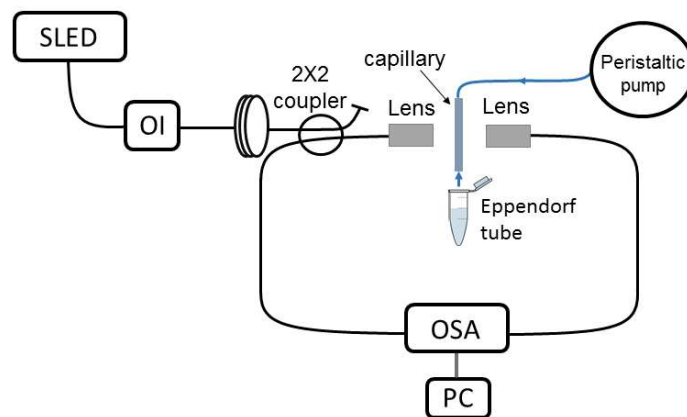
Figure 3.10 Instrumental configuration for T/R spectral measurements. SLED: Superluminescent light emitting diode; OI: Optical Isolator; OSA: Optical Spectrum Analyzer. PC: Personal Computer.

To perform T/R spectral measurements, radiation from a SLED with Gaussian emission spectrum centered at around $\lambda_c \sim 1549$ nm was coupled in standard telecommunication optical fiber. After crossing a 2x2 coupler with 50:50 splitting ratio, it was redirected orthogonally to the flat long side of the capillary under test through an aspheric lens with pigtail focuser shining a 50 μm spot at a distance of 23.5 mm. The unused output port of the coupler was terminated with an angled connector to avoid spurious back reflections. A second lens was placed on the back side of the capillary to collect the optical power transmitted through the device. Reflected and transmitted optical powers were redirected to an Optical Spectrum Analyzer (OSA, Agilent 86142B) that enabled the reconstruction of the collected spectra on the selected wavelength interval with a Resolution Bandwidth RB=0.1 nm. The source was protected by unwanted back reflections by means of a fiber pigtailed optical isolator. Fluids entered into the devices, in most of the cases, just by capillary action dipping the free ending of the capillary into a conic (Eppendorf™) tube containing the fluid to be tested. The device was connected upstream to the fluidic system by means of a plastic heat shrink tubing and a female luer adapter. A plastic tube connected the capillary to a peristaltic pump was employed to push the fluids out of the device channel after the optical detection. The capillary, as well the two lenses, were fixed to a mechanical mounting placed on an x-y-z micropositioner for precise alignment of the device and the read-out beam, as well for efficient fiber coupling of transmitted and reflected optical powers. Figure 3.11 shows the emission spectrum of the SLED source when driven with a pumping current I = 180 mA at a temperature of 20 °C, resulting in an intensity peak at $\lambda_c \sim 1549$ nm, FWHM bandwidth of 57 nm and optical power coupled in standard single-mode optical fibers of approximately 1.8 mW.
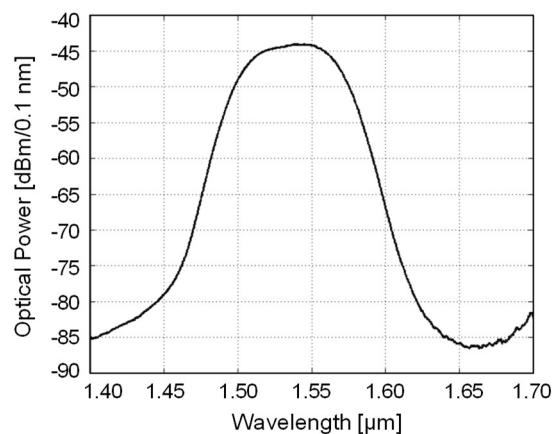
Figure 3.11 Emission spectrum of a SLED source driven with a pumping current I = 180 mA at a temperature T = 20 C°.

As reproduced in numerical simulations, reflected and transmitted optical powers were separately acquired, and the T/R ratio was then retrieved. However, experimental reflected and transmitted spectra were firstly filtered, normalized to reference powers and interpolated. In particular, since the SLED has a Gaussian shaped emission spectrum, reflected optical power was normalized to the spectrum of the optical signal incident on the capillary, while the transmitted spectrum was normalized to a reference spectrum captured by the back lens with no capillary interposed.
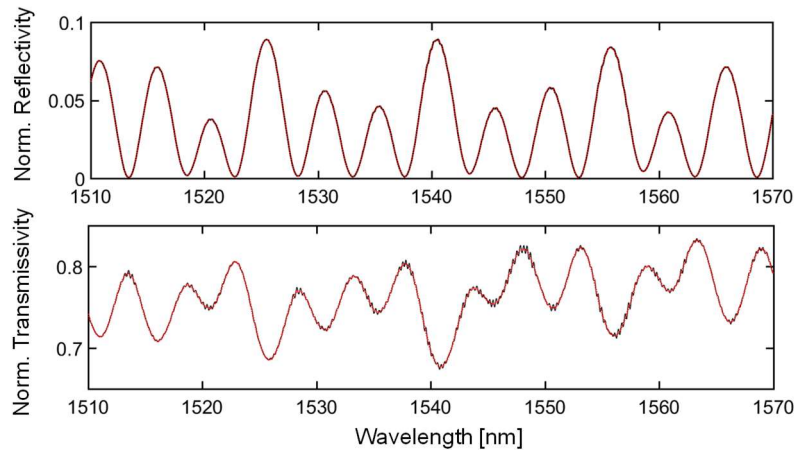
Figure 3.12 Normalized reflectivity (top graph) and transmissivity (bottom graph) acquired on a capillary with $t_f=t_b=d=50$ µm filled with water. Black traces: raw signals; red traces: interpolated and filtered signals. Final wavelength step after interpolation: 10 pm.

Then, a low-pass third order Butterworth digital filter (chosen with a trial and error approach) with $f_t=1/\lambda=2000$ µm^{-1} was applied to improve the signal to noise ratio and data were finally interpolated to obtain a set of data with a wavelength step equal to 10 pm.

Figure 3.12 shows typical normalized transmitted and reflected optical power spectra acquired on a capillary with $t_f=t_b=d=50$ µm filled with water ($n_{fluid}=1.3154$ RIU), before and after filtering. As theoretically expected, transmitted maxima correspond to reflected minima, and vice versa.

3.3. Experimental detection of refractive index variations by T/R spectral shift monitoring

Aim of our study was to detect the RI of homogenous media filling the channel of rectangular glass micro-capillaries through remote optical power measurements. In order to demonstrate the applicability of these devices as core elements of the proposed system, several experimental verifications

were performed. In particular, we tested three different kind of capillaries with glucose solutions in water at different concentrations. Two capillaries with channel depth d equal to 50 µm were used: one with walls thicknesses t_f and t_b equal to 50 µm and width W=1 mm, and one with $t_f=t_b=35$ µm and W=500 µm. Moreover, an even thinner device was tested, with $t_f=t_b=21$ µm d=30 µm and W=300 µm. All capillaries were 5 cm long. Experimental verifications based on the observation of reflectivity spectra for increasing RI of the capillary filling media were previously realized [132] [133] [134]. Here, experimental detection of both reflected and transmitted optical powers for RI monitoring is presented.
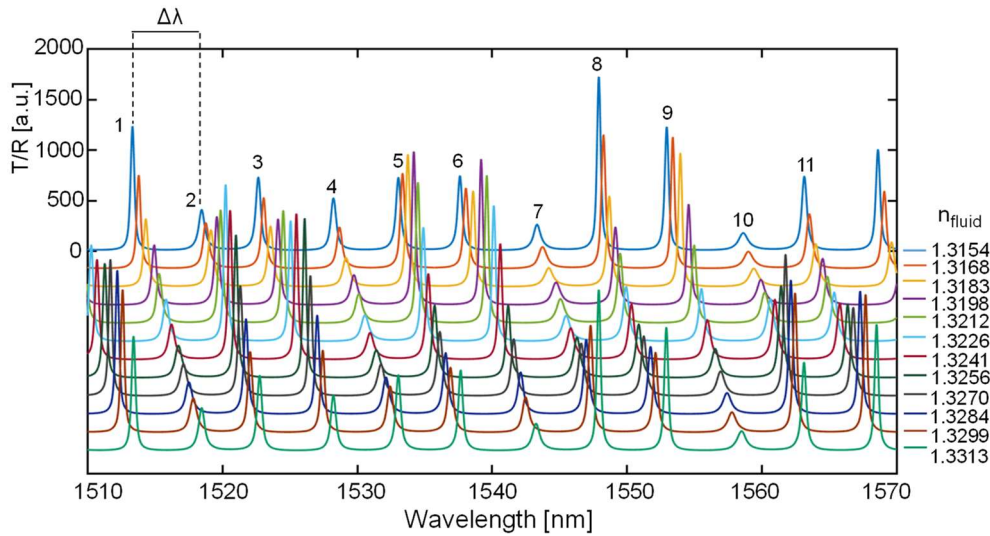
Figure 3.13 T/R spectra ratio acquired on a capillary with $t_f=t_b=d=50$ µm filled with glucose solutions with RI in the range of 1.3154-1.3313 RIU (the legend is reported on the right). Spectra are vertically shifted of -180 a.u. for a better visualization: the values on the y axis on the left refers just to the spectra relative to water.

Figure 3.13 shows the experimental T/R spectra acquired on a capillary with $t_f=t_b=d=50$ µm filled with glucose concentrations in water in the range of 0% to 11%, resulting in RI from 1.3154 to 1.3313 RIU. Spectra are virtually vertically shifted for a better visualization. As expected, for increasing concentrations of glucose in water, and thus increasing RI, a clear shift toward longer wavelengths was observed. Moreover, an amplitude variation of the resonances was observed as the filling fluid changed, as occurring also in numerical simulations. Figure 3.14 offers a 2D view of the 3D representation of data, where the signal amplitude is expressed in false colors and the shift toward longer wavelengths induced by increasing RI is better visualized.
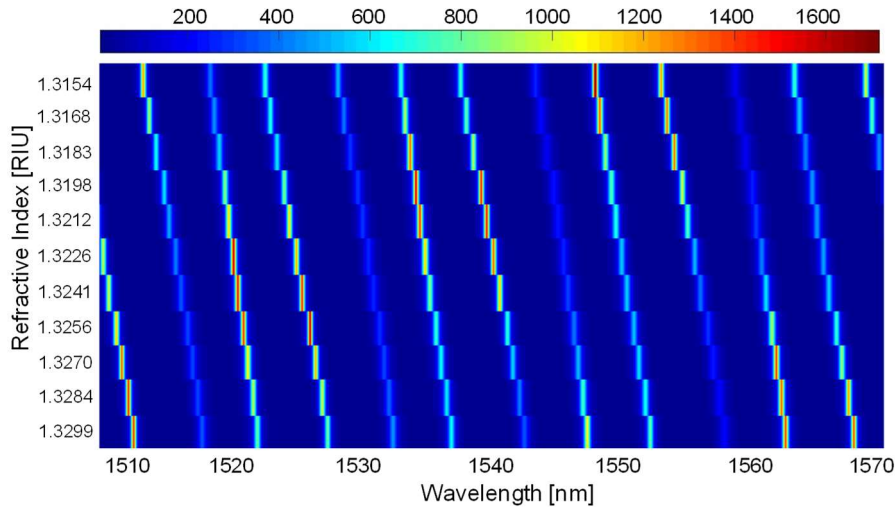
Figure 3.14 2D view of the 3D reconstruction of the T/R spectra reported in
Figure 3.13, relative to a capillary with $t_f=t_b=d=50$ µm. Amplitude is
represented in false colors, indicated on the top of the graphs.

Reporting the resonance position in terms of wavelength as a function of
the filling media RI, we obtained the calibration curves reported in Figure
3.15.
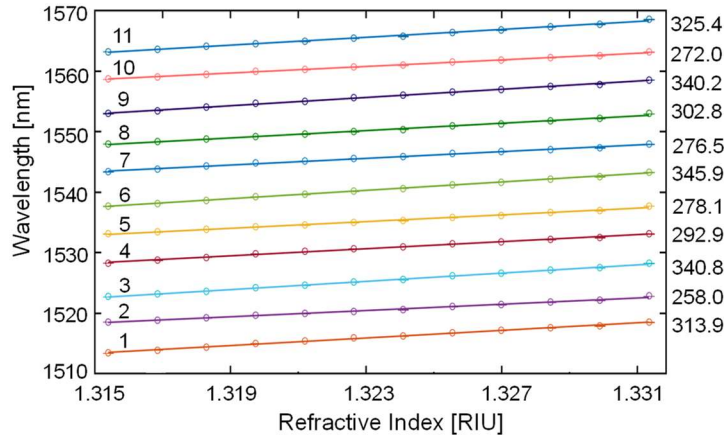
Figure 3.15 Average values (empty circles) and standard deviations (error
bars) of T/R maxima wavelength position as a function of glucose solutions
RI. Numerical values on the right side represent the sensitivities obtained
through linear fitting of the data (straight lines in the graph), reported in
nm/RIU units. Data are relative to the spectra reported in Figure 3.13 and
Figure 3.14, thus relative to a capillary with $t_f=t_b=d=50$ µm.

The straight lines represent the best linear fitting of the data obtained
through least square method. Different values of sensitivities were found
for different resonances of the T/R spectra: a maximum value
$S_{max}=d\lambda_{max}/dn_{fluid}=345.9$ nm/RIU was calculated, relative to peak 6.

78

Another important parameter in the field of sensing is the LoD, already defined as the minimum detectable change of the variable under test. In this experimental set, we calculated LoD between 5.1×10^{-5} and 4.5×10^{-4} RIU. To further investigate the impact of the capillary dimensions, we repeated the experiments on a 35-µm-wall, 50-µm-channel capillary (nominal dimensions) with solutions of glucose in water with RI in the range of 1.3154 RIU to 1.3269 RIU. In this case, a slightly wider $\Delta\lambda_{water-max}$, equal to 7.65 nm, was observed. The calibration curves obtained for this kind of device are reported in Figure 3.16. The linear fitting provided sensitivity values always bigger than those obtained over the previous investigated capillary, with same channel depth but thicker walls. In particular, we obtained S_{max} = 530.9 nm/RIU, relative to trace 2. Regarding the LoD, values of the order of 10^{-5}-10^{-4} RIU were found, i.e. of the same order of magnitude of what observed before.
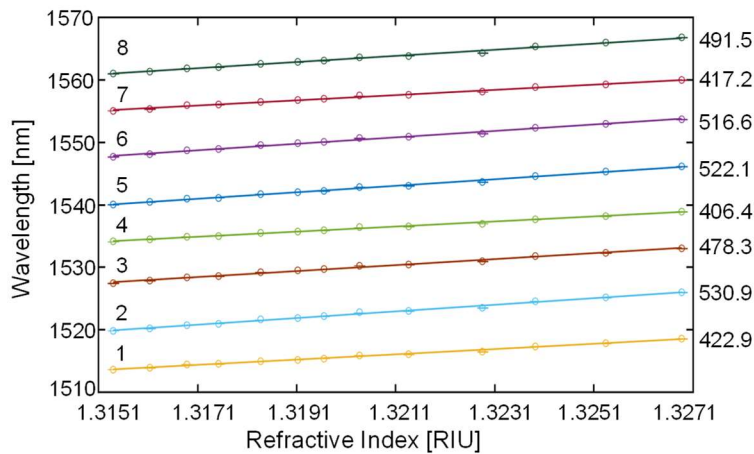
Figure 3.16 Average values (empty circles) and standard deviations (error bars) of T/R maxima wavelength position relative to a capillary with $t_f=t_b$=35 µm and d=50 µm as a function of glucose solutions RI. Numerical values on the right side represent the sensitivities obtained through linear fitting of the data (straight lines in the graph), reported in nm/RIU units.

We then proceeded investigating the last kind of capillary, i.e. the one with $t_f=t_b$=21 µm and d=30 µm, thus allowing to work with even small quantities of material. Figure 3.17 shows the 2D view of the 3D reconstruction of the T/R spectra acquired on this last device filled, again, with glucose solutions at increasing concentrations. Given the narrower channel, the collected spectra presented less resonance in the wavelength region of interest respect to previous investigated capillaries, with a maximum achieved $\Delta\lambda_{water-max}$ = 13.2 nm. Figure 3.18 reports the calibration curves obtained for the four central T/R peaks, i.e. the ones for which peaks relative to all the employed glucose solutions were present in the considered wavelength interval.
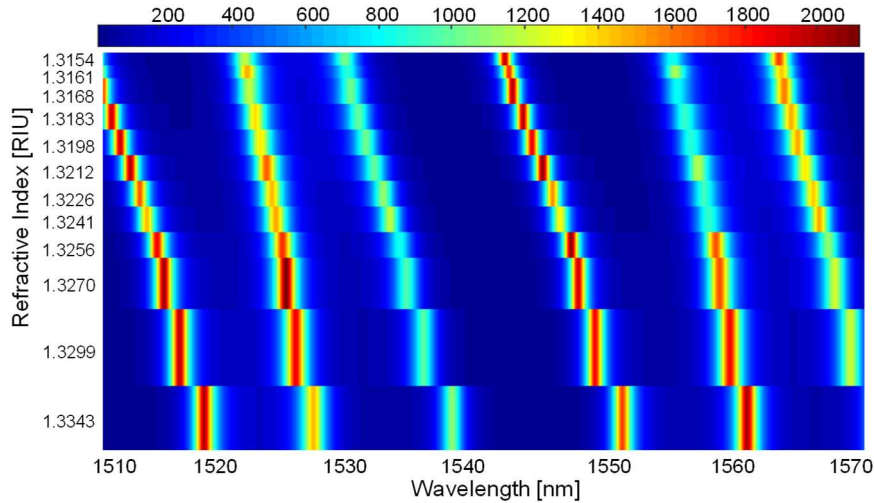
Figure 3.17 2D view of the 3D reconstruction of the T/R spectra relative to
a capillary with $t_f=t_b=21$ µm $d=30$ µm. Amplitude is represented in false
colors, indicated on the top of the graphs.
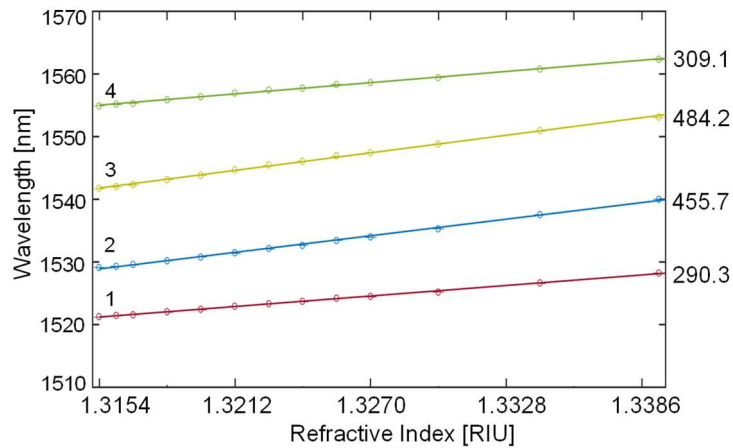
Figure 3.18 Average values (empty circles) and standard deviations (error
bars) of T/R maxima wavelength position relative to a capillary with
$t_f=t_b=21$ µm $d=30$ µm as a function of glucose solutions RI. Numerical
values on the right side represent the sensitivities obtained through linear
fitting of the data (straight lines in the graph), reported in nm/RIU units.

In this case, the maximum obtained sensitivity value was
$S_{max}=484.2$ nm/RIU, thus intermediate between those previously obtained.
Moreover, LoD in the same order of magnitude were obtained. In the
previous section, providing the theoretical results, we observed a good
degree of correlation between the maximum achieved sensitivity over a
specific device, and the characterizing parameter D, already defined as
$D=d/[d+n_{glass}\cdot (t_f, +t_b)]$. The D value was previously, obtained for nominal
values of d, t_f and t_b. Real values, on the other side, can slightly differ from
the nominal ones, with tolerances equal to 20% for the walls thickness and

80

of 10% for the channel depth. Anyway, the product $n_{glass} \cdot (t_f + t_b)$ represent the optical thickness of the capillary walls, and d can be seen as the optical path relative to the empty channel, being $n_{air} \sim 1$ RIU. The optical thicknesses of each layer of all tested capillary sample were obtained through low-coherence refractometric measurements, already presented in Paragraph 2.3.1. Consequently, we were able to obtain the effective D values for each device. In particular, we obtained D = 0.22 for the capillary with $t_f = t_b = d = 50$ µm, D = 0.33 for the device with same channel depth but 35 µm thick walls, and D = 0.31 for the one featuring $t_f = t_b = 21$ µm and d=30 µm. Table 1 summarize the experimental results obtained in terms of maximum achieved sensitivity S_{max}, maximum $\Delta\lambda_{water}$, and the specific device characterizing D. Moreover, we reported the highest index variation detectable without ambiguity, defined as $\Delta n = \Delta\lambda_{max}/S_{max}$, where $\Delta\lambda_{water}$ and S_{max} are related to the same T/R peak. As observed theoretically, the highest is the effective D, the highest the best achieved sensitivity when performing RI detection experiments. The device providing the highest overall sensitivity was the one with $t_f = t_b = 35$ µm and d=50 µm, with S_{max}=540.9 nm/RIU. The capillary with $t_f = t_b = 21$ µm and d=30 µm, on the other side, featured lower sensitivity values, but presents the advantages of the smallest internal dimension, and of the highest Δn detectable without ambiguity. The capillary with $t_f = t_b = d = 50$ µm, instead, was the one that behaved more poorly both in terms of best sensitivity and widest Δn. All tested devices provided comparable response in terms on LoD, with values in the range of 10^{-5}-10^{-4} RIU.

Capillary nominal dimensions t_f-t_b-d [µm]	Highest sensitivity [nm/RIU]	Specific measured D	Widest $\Delta\lambda_{water}$ [nm]	Highest $\Delta n = \Delta\lambda_{max}/S_{max}$ [RIU]
50-50-50	345.9	0.22	5.7	0.0165
35-50-35	530.9	0.33	7.7	0.0143
21-30-21	484.2	0.31	13.2	0.0273

Table 1 Recap of the characterizing parameters and performances relative to the employed rectangular glass micro-capillaries.

3.4. Single λ amplitude measurements: toward a compact instrumental configuration

In the previous section, RI detection was performed by monitoring the shift of the T/R peaks acquired over a 60-nm range. The reconstruction of the optical power spectra on a wide wavelength interval required an OSA, an expensive and bulky instrument. Since input power fluctuations are compensated by taking the ratio between transmitted and reflected optical powers, a possible alternative could lie in the measurement of T/R amplitude at a single wavelength. In order to further investigate this development, we focused our attention to T/R amplitude changes occurring at a selected wavelength. Figure 3.19(a) shows a zoom of some of the spectra acquired on the 30-µm-deep capillary on a 1.5-nm wavelength range. Focusing the attention on the T/R peak occurring at λ = 1541.7 nm, it can be noticed as the T/R amplitude decreased as the RI of the filling fluid increased, as a consequence of the spectra translation toward longer wavelengths. Reporting the amplitude of the T/R spectra resonances as a function of the RI of the filling fluid, we obtained the calibration curve reported in Figure 3.19(b).
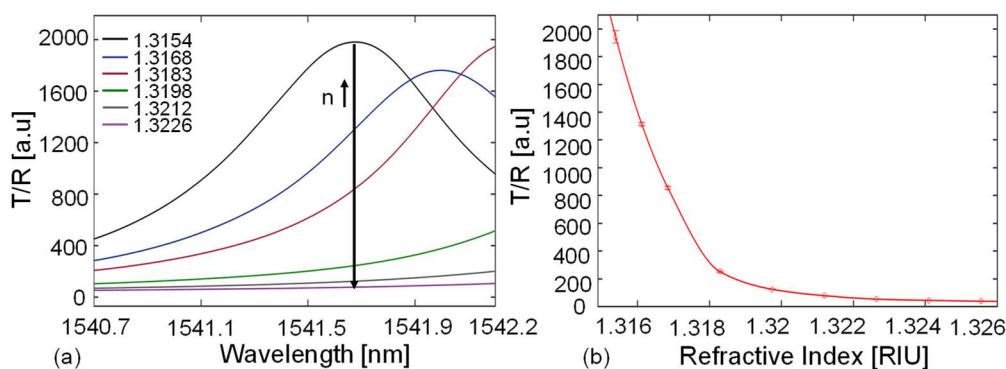
Figure 3.19 (a) Zoom on a 1.5-nm interval of the T/R spectra acquired on a 30-µm-gap 21-µm-walls capillary. At a fixed wavelength, spectra amplitude decreases as the filling media RI increases. (b) Mean value and standard deviations of the amplitude of T/R spectra in (a) at λ = 1541.7 nm as a function of the RI. A shape preserving interpolant provides the fitting of the data.

Average values and standard deviations were calculated on at least three repeated measurements. Data were fitted through a shape preserving interpolant, providing a curve exhibiting two regions with different trends. In particular, for RI values from 1.3154 RIU to 1.3183 RIU, relative to glucose concentration in water from 0% to 2%, a negative slope with high absolute value was observable, while much less significant changes in the amplitude were extracted for RI higher than 1.3256 RIU.

Performing a linear fitting for RI values between 1.3154 and 1.3168 RIU, we obtained a sensitivity equal to 750.3×10^3 [a.u./RIU] and LoD equal to 4.76×10^{-5} RIU, calculated on the central value of the highly sensitive region. These results suggest the possibility to measure fluid RI just by means of a standard semiconductor laser emitting in the telecom range and two photodiodes for the detection of transmitted and reflected optical powers, leading to a more compact and portable system.

Measuring the amplitude of the ratio T/R has the intrinsic advantage of cancelling spurious signals variations due to input power fluctuations.

3.5. Discussion and future perspective

Rectangular glass micro-capillaries integrated in a simple micro-fluidic system were demonstrated suitable as core elements of a refractometric bio-chemical sensor. Being the capillaries transparent devices, we were able to detect both transmitted and reflected optical powers, and consequently to estimate the T/R ratio. This parameter enables to compensate for source power fluctuations, with no need of an external monitoring system. We tested three kinds of capillaries, with different walls thickness and channel depth, to investigate how these parameters impact on the final sensor performances. In particular, we employed two capillaries with a 50-µm deep channel, one with walls of the same thickness and one with 35-µm thick walls, and a capillary with $t_f = t_b = 21$ µm $d = 30$ µm. The transduction method of the presented system is based on the monitoring of the T/R spectra position in terms of wavelength: in fact, as the filling RI increases, T/R spectra maxima shift toward longer wavelengths. T/R spectra were reconstructed by means of a broadband light source emitting in the near infrared, a wavelength interval of minimum invasiveness for the biological tissues. The devices were tested with glucose solutions in water at increasing concentrations (and thus increasing RIes), obtaining sensitivities higher than 258.01 nm/RIU, with a maximum value of 530.9 nm/RIU, relative to the capillary with $t_f = t_b = 35$ µm and $d = 50$ µm. LoD in the range of 10^{-5}-10^{-4} RIU were found. The sensor performances resulted thus comparable with values found in the literature relative to more complex and expensive devices, often obtained through micromachining techniques or other advanced fabrication methods. Additionally, we observed that the maximum sensitivity obtained for each kind of device is related to the ratio between the channel depth and the overall optical path length travelled by light crossing the capillary. We defined this parameter as $D = d/[d + n_{glass} \bullet (t_f, + t_b)]$, and found that the higher was D, the higher was the best achievable sensitivity. Preliminary evaluations of the feasibility of amplitude measurements have been performed with good results. The realization of single λ measurements is within the reach of current technology: indeed, they could be easily performed by means of a semiconductor laser emitting in the telecom

wavelength range and two photodiodes for the detection of transmitted and reflected optical powers. In fact, as shown before, a change in the RI filling fluid results in a change of the T/R spectra amplitude at a single wavelength. The proposed configuration would permit to perform measurements without the need of the OSA and to realize a compact, economically competitive and portable system for RI checking. Furthermore, it must be pointed out that all presented experimental results are relative to volumetric measurements: no surface sensitivity or specificity was demonstrated. However, it has been proved that non-specific refractometric measurements can be suitable to accurately detect solute concentration if associated with different measuring techniques, like for example electrical conductivity measurements [135]. Further development will regard the demonstration of surface sensitivity. Preliminary steps have been done in this direction. In particular, we established contact with two research group, one led by Prof. Marcella Chiari, of the "Istituto di Chimica del Riconoscimento Molecolare-CNR", Milan, and one lead by Prof. Maria Pesavento of the Chemistry Department of University of Pavia. The first group developed a particular mixture of polymers as support for protein and DNA micro-arrays, composed by N,N-dimethylacrylamide (DMA), N,N-acryloyloxysuccinimide (NAS), and [3-(methacryloyl-oxy)propyl]trimethoxysilyl (MAPS) [136]. Each monomer gives a particular feature to the final mixture. NAS represent the reactive group, able to bind to specific proteins amines and to amino-modified DNA. DMA helps the absorption of the polymer on glass, while MAPS gives higher stability to the coating. Starting from a diluted aqueous solution, the developed polymer mixture is able to adsorb to glass in a very short time (10-30 min). The second group, led by Prof Maria Pesavento, employed molecularly imprinted polymers (MIPs) prepared with standard procedure [137] to monitor low levels of different substances of interest, such as furfural and trinitrotoluene [138], [139]. MIPS are developed polymerizing monomers in presence of a template molecule. This molecule is lately extracted, leaving binding sites with high affinity to the template molecules. Both the copoly (DMA-NAS-MAPS) and MIPs have been widely used to functionalize flat surfaces, such as glass slides for DNA and protein experiments [136], [140], or optical fibers [138], but have never been employed to functionalize the internal surfaces of closed structure such as channels. For this reason, we are trying different experimental procedures to be able to reproduce layers of desired and controlled thickness (of the order of nanometers) on the internal faces of a glass micro-capillary, and testing the capability of our optical system to detect thin layers. We are as well investigating the best suited post-elaboration of acquired traces in order to extract the maximum information from available data.

Chapter 4

The Interferometric Reflectance Imaging Sensor (IRIS): working principle and experimental results

4.1. High and Low-magnification IRIS: basic principles

The Interferometric Reflectance Imaging Sensor (IRIS) is an imaging platform allowing the label-free detection of various biomolecules with high-throughput, high sensitivity and reproducibility. IRIS has been applied to the real-time monitoring of protein-protein (antigen/antibody), protein-DNA [141], [142], and DNA-DNA [143] bindings occurring on a flat solid surface, as well as to virus detection [144]. IRIS exploits optical interferometry and spectroscopy to detect and quantify particles accumulation on a bilayer chip composed by silicon and silicon dioxide (SiO_2/Si) in a microarray format. Microarrays were firstly introduced in the 80s, earning increasing interest for micro and nanoparticles detection. A microarray basically consists in a solid flat substrate, usually a glass or polymeric slide, where bioreceptors are immobilized in multiple spots, typically placed following a 2D grid. Different bioreceptors can be linked to different spots, allowing a multiplexed and high-throughput analysis of the sample. As molecules complementary to the probes are deposited over the slide, binding will take place. In standard microarrays, bound molecules are usually marked with fluorescent labels to enable the optical detection. Microarrays have found wide application in the field of genomics research and in protein studies. The IRIS system employs custom designed microarrays to detect biomolecules interaction in most of the cases in a completely label-free way, with no need of additional markers. IRIS sensors are obtained starting from SiO_2/Si wafers with thermally

grown oxide films of desired thickness (purchased from Silicon Valley Microelectronics, Santa Clara, CA). Standard photolithography and wet etching are employed to create fiducial markers [145]. Wafers are then cut to obtain 10 mm x 10 mm x 0.5 mm chips, where a smaller inner section of 2.3 mm x 2.3 mm represent the active region. SiO_2/Si wafers are very well known and characterized materials widely employed in the field of CMOS technology. Moreover, the top SiO_2 layer allows to employ standard glass surface functionalization techniques. In its first version, IRIS was just capable of monitoring the amount of bounded mass. Recently, IRIS have evolved allowing the identification of individual nanoparticles immobilized onto the chip surface. This new version is known as single particle IRIS (SP-IRIS), and has been successfully applied to the label-free highly-sensitive detection of viruses, also from complex media [146], [147]. In this section, I will introduce the principle of operation of the IRIS platform in both configurations: low-magnification IRIS, for real-time detection of biomass accumulation, and high magnification IRIS, or SP-IRIS, for single particle detection. Both configurations exploit the same basic structure with minor changes. Common elements are the LEDs providing the read-out radiation, a beam-splitter employed to redirect the light perpendicularly onto the sensing surface, and a CCD camera to collect real-time images of the chip (Figure 4.1(a)). Both systems are based on a top-illuminated microscope. The principal differences, on the other side, regard the magnification of the optical system and the numerical aperture (NA) of the objective lens. In the first working modality of IRIS, i.e. low-magnification IRIS, spectral reflectivity is at the basis of the transduction mechanism. Briefly, in the last configuration, read-out radiation is provided by a multicolor LED (ACULED VHL, ACL01-MC-RGYB, Excelitas Technologies, Pfaffenhofen, Germany) source providing radiation in the red, green, yellow and blue region. Emitted read-out radiation reaches a beam-splitter, that redirects part of the impinging radiation toward the sensor surface in a perpendicular way. Reflected light crosses again the beam-splitter and, through an objective, reaches a CCD sensor (Retiga, QImaging, Corp., Surrey, BC, Canada). As radiation impinges on the bilayer silicon structure, it is partially reflected and partially transmitted at each interface, as described by the Fresnel model, already introduced in section 3.1.1. In low-magnification IRIS, a low-numerical aperture (NA~0.06) objective is employed: thus, polarization of light can be ignored and the simplified expression of the Fresnel coefficient can be considered. With this approximation, reflection coefficient for the optical field can be calculated through Eq. 26, where $n_1=n_{air}$ and $n_2=n_{SiO2}$ for the air/Si interface, resulting in a coefficient r_1, while $n_1=n_{SiO2}$ and $n_2=n_{Si}$ for the SiO_2/Si interface, resulting in a coefficient r_2. The overall reflectivity can be retrieved as [148]

$$R = |r^2| = \frac{r_1{}^2 + r_2{}^2 + 2r_1r_2\cos(2k_sd)}{1 + r_1r_2 + 2r_1r_2\cos(2k_sd)} \qquad (61)$$

where d is the SiO_2 layer thickness and k_s is the wavenumber of the wave vector perpendicular to the considered interface. Since in Eq. 61 all the variables are well defined beside the thickness d, IRIS exploits an analytical model based on Eq. 61 and a minimization algorithm such as the Levenberg-Marquardt algorithm [149] to retrieve the thickness of the glass upper layer for each pixel in the image. As biomolecules are adsorbed on the slide surface, light shined on the sensor undergoes a phase shift proportional to the amount of accumulated mass (Figure 4.1(b) and (c)), thus resulting in a reflectivity change at a single wavelength. Reflectivity spectra are sampled at various wavelengths by the CCD camera, and consequently, a biomass accumulation results in an intensity change in the acquired images. Figure 4.1(d) shows a typical image acquired by the low-magnification IRIS, where biomolecules spots appear as brighter circles on the darker silicon dioxide background. Biomolecules accumulation can be treated as an additional thickness of the SiO_2 layer with constant RI, that IRIS is able to detect. A conversion factor between the detected SiO_2 layer increase and the amount of effective accumulated biomass has been experimentally determined [142].
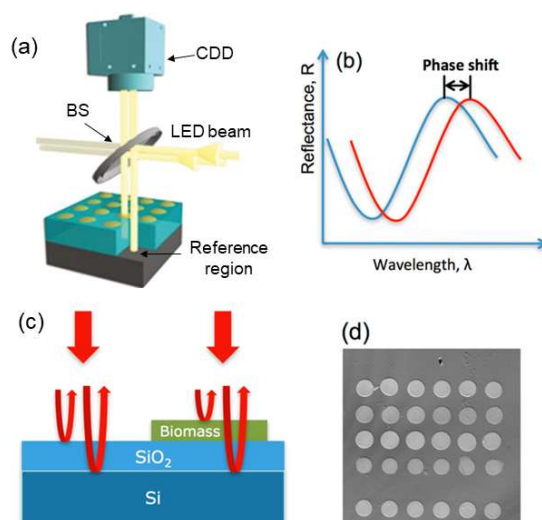
Figure 4.1 Representation (a) of the employed optical imaging system and (c) of a SiO_2/Si substrate from a longitudinal point of view for working principle representation. The red arrows show the reflection of light at each interface. (b) Reflectance spectrum shifts due to an accumulation of biomass on the chip surface like in (c). (d) typical detected image of a protein chip. Reused from [143] and [145].

To accurately reconstruct the reflectivity curves for the sensor surface, it is mandatory to monitor the source emission intensity, in order to compensate for eventual power fluctuations. In its first configuration, IRIS was provided with an additional photodetector for intensity light monitoring. In more recent versions, a simpler solution was implemented: a silicon region of the chip is exposed by etching of the SiO_2 layer and used

as reference region to normalize intensity fluctuations of the read-out light
source [150]. Low-magnification IRIS has been applied to the label-free
dynamic monitoring of antigen-antibody interaction [141]. In particular,
bovine serum albumin (BSA), human serum albumin (HSA), rabbit IgG
and protein G were employed as probes, and the reaction with their specific
antigen has been monitored in real-time. Low-magnification IRIS has been
as well employed [143] to investigate nucleotide sequences denaturation
kinetics as a function of solution ionic concentration. Let's know introduce
the other, and more recent, IRIS configuration: the SP-IRIS. As stated
before, high-magnification IRIS employs the same basic equipment: a
bilayer substrate, the beam-splitter, LED sources and the CCD sensor. The
main difference, on the other side, consists in a different objective: while
low-magnification IRIS exploits a 2x or 4x magnification objective,
SP-IRIS uses a magnification as high as 40x or 50x. Moreover, a higher
numerical aperture is employed, approximately equal to 0.8, against
NA~0.06 of low-magnification IRIS. When working in low-magnification
modality, the resulting field of view (FOV), is sufficiently wide to capture
in a single image the whole active part of the chip. On the contrary, in
SP-IRIS the FOV is significantly reduced, and a single image usually
includes just one spot (biomass spots have usually a diameter around
100-150 μm, and up to 100 spots can fit into the chip active region).
Anyway, SP-IRIS images can be acquired in an automated and consecutive
way in order to acquire information about all the spots immobilized on the
chip in a singular experimental verification. Figure 4.2 shows a schematic
representation of the setup.
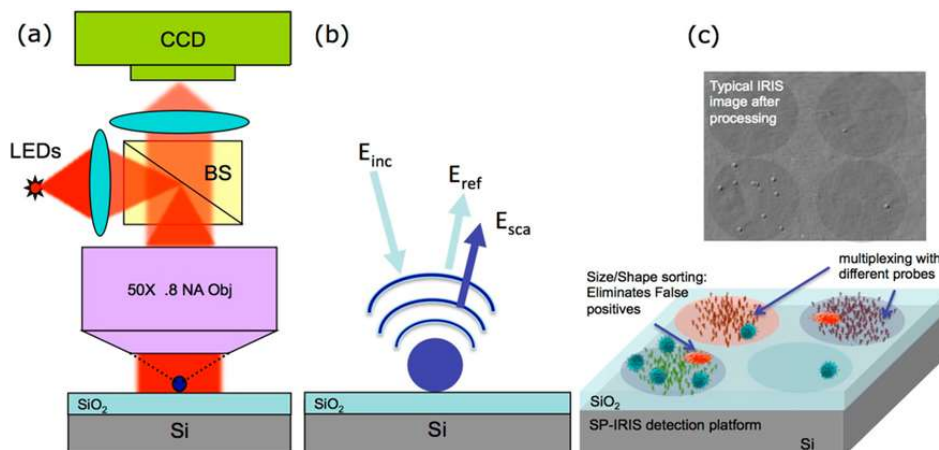
Figure 4.2 (a) Schema of the optical setup for single particle detection. The
principle of operation relies on the enhanced sensitivity given by the
interference of the field scattered by the particle and the reference field
reflected by the silicon substrate as shown in (b). (c) Picture of a typical
chip with different capture probes, allowing a multiplexed detection. Single
particles are detected in the image captured by the CCD camera as brighter
dots, which contrast is related to the particle size itself. Reused from [148].

In SP-IRIS, as a particle is bound to the SiO_2, it produces scattering effects of the incident read-out beam. The scattered field intensity, for particles such as protein or viruses, is very small and very challenging to detect with traditional imaging systems. SP-IRIS exploits the principles of interferometry to enhance the scattered field. The reflected field at the SiO_2/Si interface interferes with the field scattered by the nanoparticle of interest (see Figure 4.2(b)). If the thickness of the SiO_2 layer is correctly engineered, the interference yields an enhancement of the scattered field by the bound biomolecule, that becomes detectable by the CCD camera. In fact, the phase delay introduced between the reference and the scattered field depends on the top glass layer thickness. Consequently, the SiO_2 layer dimension is optimized in order to obtain the maximum contrast for the particles of interest. According to the Mie theory, the electric field scattered from a nanoparticle in free-space is proportional to the dipole moment p, which, in turn, depends on the polarizability of the particle and on the incident electric field according to [151]

$$E_s \propto p = \alpha E_i \tag{62}$$

and

$$|E_s| \propto \alpha^2 \tag{63}$$

If the particle size is much smaller than the wavelength of light, the Rayleigh approximation is applied, and the polarizability of the particle can be retrieved as

$$\alpha = 4\pi\varepsilon_0 r^3 \frac{\varepsilon_p - \varepsilon_m}{\varepsilon_p + 2\varepsilon_m} \tag{64}$$

where ε_0 is the permittivity of the vacuum, ε_m that of the surrounding media and ε_p that of the particle of radius r. From Eq. 63 and Eq. 64 it is clear that the intensity of the scattered signal scales with r^6. For nanometric particles, this leads to a weak signal that is easily buried in the system noise. When the scattered field, instead, interferes with a reference field E_{ref}, the detected intensity is given by:

$$I \propto |E_{ref}|^2 + |E_{sca}|^2 + 2|E_{ref}||E_{sca}| \cos \emptyset \propto r^3 \tag{65}$$

where $\emptyset$ is the phase delay between the scattered and reference field. In this equation, $|E_{ref}|^2$ provides constant background intensity, $|E_{sca}|^2$, as

89

said before, scales with the sixth power of the radius and thus is negligible in case of nanometric particles, while the cross-term $|E_{ref}||E_{sca}|$ dominates the signal coming from the particle of interest. The described system behaves like a common path interferometer, in which reference and measuring beams travels along the same path. Practically, thanks to fields interference, immobilized particles generate a signal that interacts with the reference light reflected by the substrate, producing an optical signal that can be more efficiently detected by the CCD sensor. In other words, we can say that the reference field enhances the field scattered by particles adsorbed on the chip surface; particles thus result as diffraction limited brighter dots in the image captured by the camera, as shown in Figure 4.2(c). Taking into account the contrast of the particle, its size is retrieved from the image with a forward model [152]. Size calculation allows to eliminate false positive signals coming from impurities deposited on the chip surface. For single particle detection, SP-IRIS have demonstrated performances [153], [154] that overcome those of Surface Plasmon Resonance (SPR) systems [155], [156], allowing a label-free detection of single molecules with a compact and cost-effective system.

4.2. Low magnification IRIS for rare mutation identification: thermodynamic analysis of nucleotide sequences

During my staying in the OCN laboratory at Boston University I gave my contribution to activities in the framework of a wider project, aimed to the identification of rare-mutation in nucleotide sequences for cancer identification and treatment. Experimental detection of DNA sequences had already been performed with the SP-IRIS through standard end-point measurements before my arrival. In order to obtain single molecule DNA detection, an additional step with comparison to virus detection was required. In particular, given the ultra-low dimension of the strands, to obtain a sufficiently high particle contrast over the image background, binding of gold nanoparticles (AuNP) with the sequence to be detected was found necessary. Although good results were obtained, a limit of detection higher than what theoretically reachable was found. This issue was probably addressable to a high level of non-specific binding. In order to improve the specificity of the test, we chose to better analyze the probe hybridization thermodynamics. In fact, double-stranded DNA, where single nucleotide polymorphism (SNP) are present, is expected to be characterized by a lower melting temperature, as a consequence of the weaker bound between the not fully complementary sequences. With this aim, during my stay I personally realized real-time experiments where DNA dehybridization was induced by temperature variation [157]. As

double-stranded DNA denatured, unbound material was washed by a flowing buffer and the relative intensity change was monitored by means of the low-magnification IRIS. In the experimental verifications, we focused our attention on KRAS wild-type (WT) and KRAS G12D mutant sequences, differentiated by a single mutation that occurs at the codon 12 of the gene [158]. KRAS gene codifies for the generation of a GTPase protein (KRAS protein, precisely), and is included in the list of oncogenes related to several type of cancer. KRAS genes are involved in a signal pathway known as the RAS/MAPK pathway: as KRAS binds to GTP molecules, it turns into an active state, during which regulates cell growth and differentiation. As GTP is converted to GDP, KRAS protein is turned off. SNP in the KRAS genes can have the effect of shifting its nucleotide-binding equilibrium toward its active state [159], leading to an uncontrolled cell growth and division. Approximately 36–40% of patients with colorectal cancer have tumor-associated KRAS mutations [160] and between them 33.5-34.4 % present a specific G12D mutation. KRAS G12D is also associated with lung adenocarcinoma with a frequency of 17% [158].

Let's see in more detailed the followed experimental procedure. Si chips with thermally grown SiO_2 silicon dioxide layer with thickness equal to 100 nm were employed.
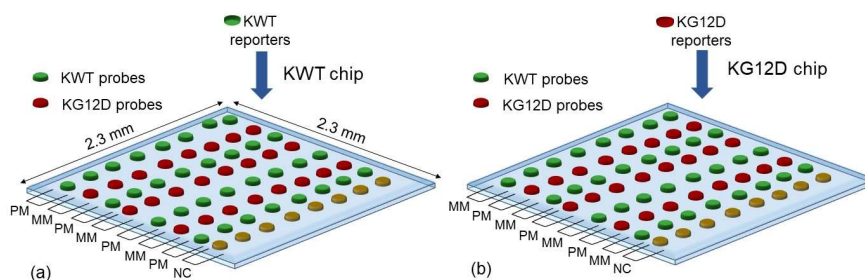
Figure 4.3 Preparation of the two different kind of chips employed for the DNA melting experiments. Wild-type KRAS sequences (KWT, green dots) and mutated KRAS G12D sequences (KG12D, red dots), are deposited on the chip as probes. Chips are then incubated with DNA reporters perfectly complementary to the KWT sequence (a, KWT chip) or to the KG12D sequence (b, KG12D chip). Complementary sequences will perfect bind (PM: perfect match), while sequences differing by a SNP will result in a weaker bound (MM: mismatch). For KWT chip, PM: KWT+anti-KWT and MM: KG12D+anti-KWT. For KG12D chip: PM: KG12D+anti-KG12D, MM: KWT+anti-KG12D.

Wafers were preliminary treated as described in the previous section. Then, chips were subject to plasma etching in oxygen environment for surface cleaning. Afterward, the SiO_2 surface was functionalized by absorption of a layer of copoly (DMA-NAS-MAPS) to avoid unspecific binding and allow a stronger link of biomolecules to the sensor surface.

The polymer mixture and his properties were already discussed in Paragraph 3.5. Subsequently, chips were spotted with solution of single-stranded DNA molecules at 25 µM concentration arranged as in Figure 4.3 and incubated overnight. Deposited spots had usually diameter around 100 µm. DNA solutions were obtained starting from 2 µl of 100 µM amino-modified DNA solution diluted with 4 µl of Deionized (DI) water and 2 µl of Sodium Phosphate Buffer (NaPB), obtaining 25 µM concentrated DNA solutions. Subsequently, solutions of wild-type KRAS (KWT) and KG12D complementary sequences (reporters) were prepared adding 24 µl of saline-sodium citrate (SSC) 2X buffer to 1 µl of DNA solution at 100 µM concentration. Different chips were prepared as follow: solution of KWT reporter was deposited on the first chips (KWT chip), while solution of KG12D reporters was deposited on the second (KG12D chip), as clarified in Figure 4.3. Fully complementary DNA strands bound in a perfect match (PM), while sequences differing by a SNP result in a mismatch (MM). Consequently, in the KWT chip, PM are constituted by a KWT probe and a KWT reporter, and MM by a KWT probe and a KG12D reporter. On the opposite, in the KG12D chip PM are constituted by two KG12D sequences and MM by a KG12D probe and a KWT reporter. Chips were incubated for at least 90 minutes, and then washed multiple times with buffer solutions. At this point, chips were ready for the melting experiments. For each experimental verification, chips were inserted into a custom designed polymeric cartridge [146] with two connection to the external fluidic, one for fluid insertion and one for the waste exit. The plastic support was then leaned over a stage connected to a temperature controller. The cartridge was connected upstream to a peristaltic pump through standard tubing dipped at the other end into an Eppendorf™ tube containing SSC 0.5X buffer. In each experiment an image of a bare SiO_2/Si wafer (mirror image) was as well collected and subsequently employed to correct for eventual un-uniformity of read-out light over the chip. Then, real-time images were acquired at interval of 30 seconds as the stage temperature was linearly increased from 25 °C to 75 °C and buffer was flowing over the chip to remove the unbound DNA material.

(a) (b)
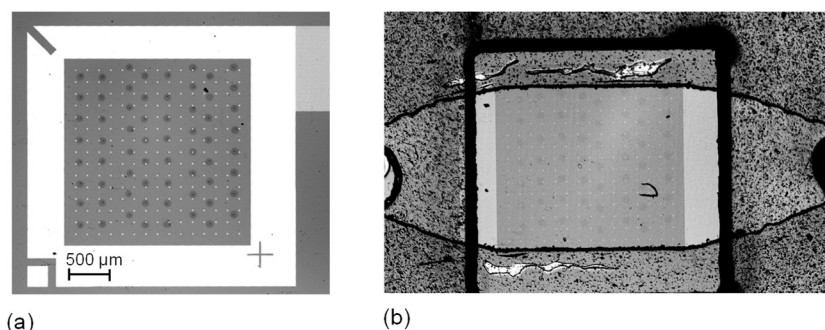
Figure 4.4 Low-magnification IRIS images of a SiO_2/Si sensor functionalized with KRAS probes and reporters. Image (a) of a dry chip and (b) of a chip inserted into the polymeric cartridge and immersed in buffer.

Figure 4.4 shows two low-magnification images acquired with the IRIS system in dry and wet conditions. Figure 4.4 (a) shows a picture of a dry chip functionalized with KWT and KG12D reporters. The DNA spots are identifiable as darker circles over the brighter background. Figure 4.4 (b), instead, shows the chip inserted into the polymeric cartridge and covered with flowing SSC buffer. It can be noticed as the contrast of the spots over the background is highly reduced when collecting images of the chip in fluid. Whereas initially multicolor images were acquired, we then found that higher contrast for our specific experimental conditions was provided by the blue LED. For this reason, images were subsequently acquired employing just the blue LED as read-out source. A preexisting MATLAB code was already available for low-magnification image analyses, but a custom one needed to be developed for the extraction of the parameters of interest for image acquired in our specific experimental condition. Consequently, I personally developed a custom software in order to monitor the reflectivity change of the DNA spots due to DNA denaturation as a function of the set temperature. Each acquired image was preliminary normalized to a bare silicon region to correct for eventual source fluctuations and to a mirror image to eliminate for light un-uniformity over the FOV. Images were then filtered with a moving average filter to reduce the overall noise. In order to obtain an automated extraction of parameter of interest, images alignment was the first requirement. As reference image, the first one in the acquired stack (i.e. the dry chip one) was employed.
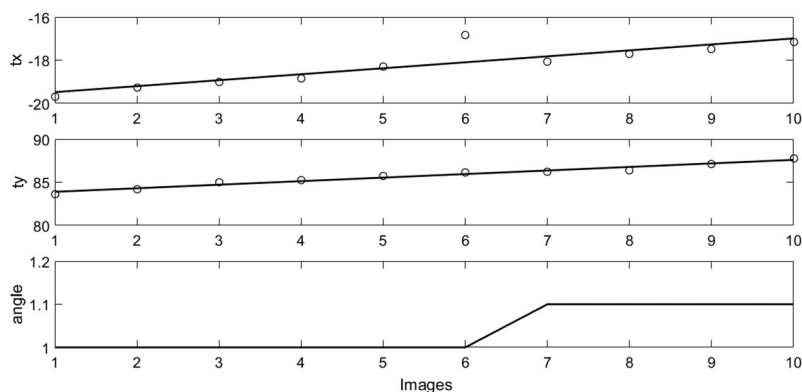
Figure 4.5 Detected translation along the x (upper graph) and y (middle graph) axes (in pixel units) and angle of rotation (lower graph) applying the registration algorithm on a stack of 10 consecutive images. The straight lines in the upper and middle graph represent the linear fitting of the data.

To obtain the image registration, the bare silicon exposed points (identifiable in Figure 4.4 as brighter dots over the chip background) were employed as fiducial marks. Alignment is performed for all the image in the stack exploiting a phase correlation method to reduce the distance between the reference and targets images. Figure 4.6(a) and 4.6(b) shows as exemplification the superimposition of a cropped region of the reference

image and a target one, before (a), and after (b) the alignment. Figure 4.5
shows the detected translation and rotation over a 10 images stack. Image
alignment algorithm was demonstrated perfectly repeatable. After having
obtained the image alignment, the user is required to select a specific
region of the images that contains the spots that need to be analyzed. Based
on a radius interval given by the user (Figure 4.6(c)), spots in the region of
interest are automatically detected through the *imfindcircles* MATLAB
function based on the circular Hough transform (CHT). An annulus
surrounding each spot is as well selected. All described steps were
performed on the binary version of the images. Dirt or blemish can
sometimes be wrongly identified by the code as biomass spots. The number
of incorrectly detected spots strongly depends on the quality of the image
and cleanliness of the chip: in the performed experimental verification it
usually varied from 0 to less than 10 % on the total number of detected
spots. For this reason, the center position of the detected spots is compared
to a reference grid. The spots which centers lie farther from the grid centers
than a given distance are discarded and not considered into the reflectivity
detection (Figure 4.6(e)). If two or more spots fall in the same region
within a maximum distance parameter, the user is required to manually
select which spot must be considered for the subsequent examination.
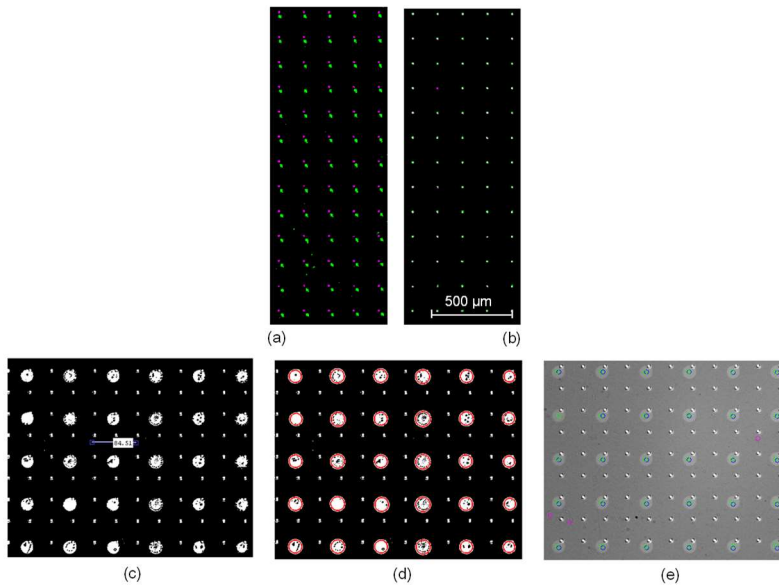
Figure 4.6 Superimposition of the same cropped region of two consecutive
acquired images before (a) and after (b) di alignment. Purple and green dots
correspond to the bare silicon fiducial mark of the chip. The user, helped by
a measuring tool, enter a possible interval for the spots radii (c), then
detected exploiting the CHT transform (d). (e) Example of the grid
application for avoiding false spots detection. Blue dots represent the
detected spots centers, the green dots are the grid points employed for
comparison, while pink dots represent the center of region identified by the
CHT as spots region but that don't find correspondence in the grid and are
thus subsequently discarded.

At this point, median gray values of each spot (Med_{spot}) are subtracted to the relative surrounding annulus median value ($Med_{annulus}$), in order to retrieve the reflectivity spots difference over the background $\Delta_{ref}=Med_{annulus} - Med_{spot}$. To obtain the overall PM and MM reflectivity values, the average Δ_{ref} over all the PM ($\Delta_{ref,PM}$) and MM spots ($\Delta_{ref,MM}$) is calculated. Finally, plotting $\Delta_{ref,PM}$ and $\Delta_{ref,MM}$ as a function of the temperature, the experimental melting curves are obtained. The same procedure was followed to detect the reflectivity change of negative control spots. Outliers are removed from the curves on the basis of a distance function. It must be pointed out that during the experiments we had to face the problem of air bubbles generation, in particular for high temperatures. Buffer sonication was performed before each experimental verification, reducing, but not eliminating, the formation of bubbles. For this reason, not in all the experimental verifications was possible to average over the whole number of spots in the chip. Figure 4.7 shows the un-normalized traces for PM, MM and NC obtained over a KWT chip.
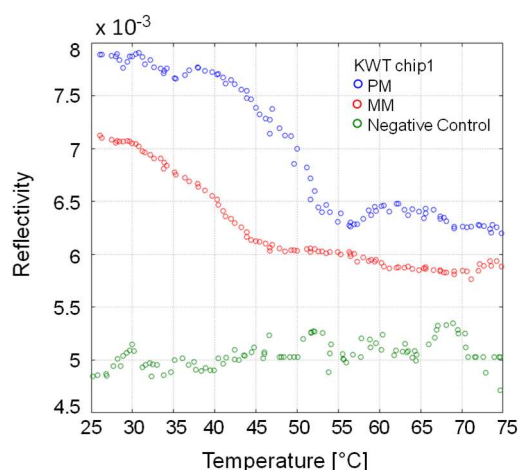
Figure 4.7 Melting curves relative to a KWT chip. Reflectivity values are obtained averaging over multiple spots. Blue dots: PM spots, red dots: MM spots, green dots: negative control spots.

Since curves start from different reflectivity values, addressable to different levels of reporters hybridization in PMs and MMs, the curves were normalized to the peak value for better readability. Figure 4.8(b) shows the normalized melting curves obtained from Figure 4.7 for PM and MM. Fittings are provided by a 9th degree interpolant. PM and MM curves appears sufficiently different: in particular, if we consider the temperature at which half of the material appears to be denatured, known as the melting temperature (considering the starting and ending value of reflectivity), we can find $T_{m,MM} \sim 39.5$ °C and $T_{m,PM} \sim 48.1$ °C. Figure 4.8(b) reports an additional experimental set. In this case, closer values of melting

temperature were found, but anyway distinguishable. Specifically, $T_{m,PM} \sim$ 46 °C and $T_{m,MM} \sim$ 41 °C.
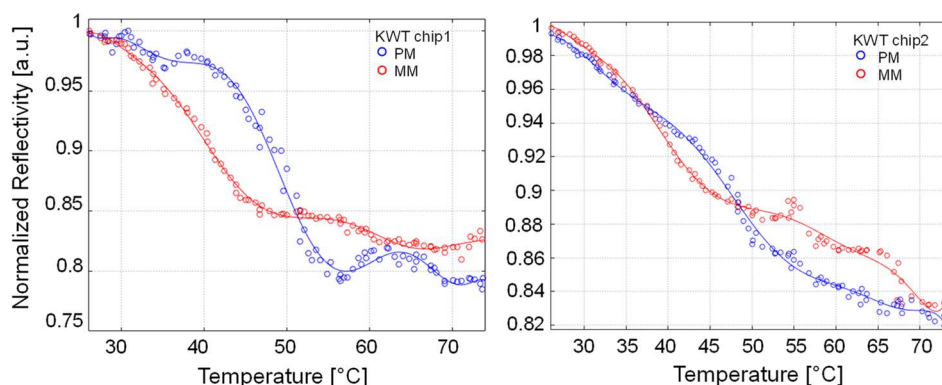
Figure 4.8 Normalized melting curves (a) obtained from Figure 4.4, (b) relative to an additional KWT chip. Blue dots: PM spots, red dots: MM spots. The negative control is no longer reported. Solid lines provide the 9th grade fitting of the data.

The situation is quite different for the KG1D chips, as exemplified by Figure 4.9. It can be noticed as the PM melting curve results quite similar to those previously obtained, while the MM curve exhibits a very small variation for increasing temperature, starting from a low reflectivity value, that seems due to a low starting level of hybridized reporters. Similar results were found in additional KG12D experiments.
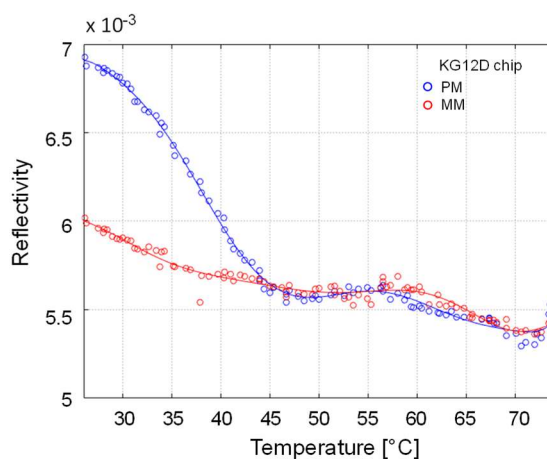
Figure 4.9 Melting curves relative to a KG12D chip. Reflectivity values are obtained averaging over multiple spots. Blue dots: PM spots, red dots: MM spots.

An explanation to the observed phenomenon comes from a subsequently realized experiment. The interaction between KWT and KG12D probe and

reporters for PM and MM was investigated by means of the SP-IRIS through standard end-point measurements, in order to obtain an estimation of the number of bound molecules. NC probes, KWT probes and KG12D probes were spotted on both chips. Chip 1 was then incubated with KG12D reporters and chip 2 with KWT reporters. Finally, both chips were incubated with both KWT and KG12D AuNP labels, to enable particle counting. The histogram in Figure 4.10 shows the number of bound reporters to the three different kind of spots. It is clear how KWT reporters bind to both KWT and KG12D with the same affinity. On the opposite, KG12D reporters appears to highly bind to PM probes, but have very low affinity for the KWT probes. In summary, wild-type reporters have very high level of cross-hybridization, while mutant reporters bind well just with fully complementary probes. This result helps to explain the different melting curves obtained for the MM spots in KWT and KG12D chips.
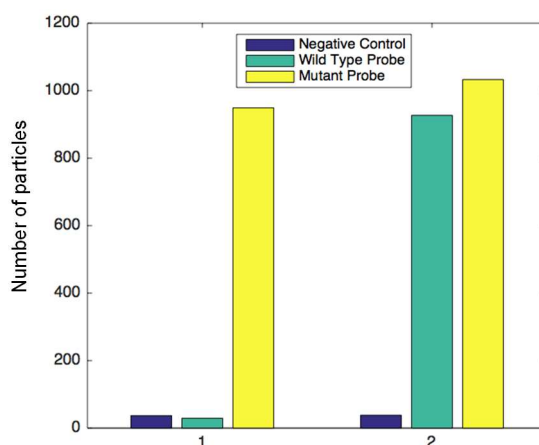
Figure 4.10 Counting of bound reporters over two different chips performed with the SP-IRIS technology. Both chips were preliminarily spotted with KWT, KG12D and NC solutions. Chip 1 was then incubated with KG12D reporters, and chip 2with KWT reporters. To enable particle counting, chips were then incubated with Au nanoparticles labels for both KWT and KG12D sequences. It is clear how wild-type and mutant probes have different mismatch affinities.

In conclusion, the proposed method allows to monitor in real-time the variation of biological material bound to a SiO_2/Si sensor in a micro-array format. The detection doesn't require the use of additional biomarkers, and can be performed in a high-throughput and multiplexed way. The developed system could be potentially applied to the monitoring of bimolecular interaction of small particles (for example, avidin-biotin) or in the field of drug-discovery. Label-free nucleic acid hybridization thermodynamics study showed that melting curves relative to cross-hybridized and fully complementary sequences are sufficiently different if compared one to the other, even if further experimental verification would be required to obtain more reliable results.

The performed experiments are of course not suited to distinguish rare mutations, but deeper understanding of the thermodynamic properties of specific nucleotide sequences could be useful in the design of rare mutation experiments realized with the SP-IRIS system in order to overcome the resolution limit of the system given by high cross-hybridization levels. Melting curves reconstruction could also be an interesting tool for comparison of different primer design algorithms. Different algorithms are employed to design primers for maximum sensitivity and specificity. The proposed label-free detection method could be at the basis for the development of an easiest way to experimentally test the designed primers compared to standard fluorophores labeled detection.

4.3. Silicon dioxide erosion evaluation and investigation on alternatives materials

It is known that acids are capable of eroding SiO_2. In order to investigate the amount of erosion of the SiO_2 due to acid buffers, a chip was prepared spotting just buffer on half of the spots, while a regular KWT probes solution was spotted on the remaining. Chips were subsequently incubated overnight, then washed and analyzed through standard low-magnification IRIS measurements. Figure 4.11 shows the height variation, in nanometers, with respect to the starting condition, due to probes immobilization and to the erosion induced by NaPB 15 mM after the overnight incubation at room temperature.
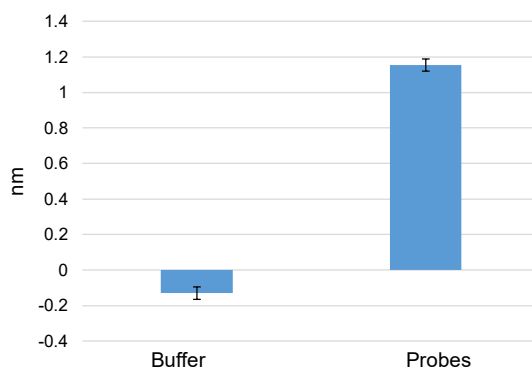
Figure 4.11 Average values and standard deviation of the SiO_2 thickness change due to erosion induced by NaPB 15 mM and DNA probes accumulation.

The average erosion, converted in nanometers through the application of the forward model defined in [153], was found equal to H_{buffer}=130 pm $\pm$

39 pm, while H_{probes}= 1.153 nm $\pm$ 42 pm. SiO_2 erosion amount could also significantly increase when working at higher temperatures, like the ones employed in previously presented experiments.

Thus, it was found that acid buffers could have an impact on SiO_2 thickness when dealing with long incubation times. This effect could lead to an underestimation of the effective amount of bound molecules.

For this reason, we start to evaluate the possibility of substituting the SiO_2 layer with polymeric materials. As alternative material, polymethyl methacrylate (PMMA) 495 (i.e. with 495000 molecular weight) was firstly chosen. PMMA is a versatile material well suited for imaging applications that provides good chemical resistance to acids [161]. PMMA is one of the hardest thermoplastics, with high mechanical strength and good resistance to scratching: moreover, it exhibits good dielectric propertied and good resistance to temperature changes [162].

PMMA 495 was deposited on bare silicon wafers through spin coating. Bare silicon wafers were firstly cleaned by immersion in acetone for 2 minutes and subsequently rinsed and immersed in isopropanol for 30 seconds. Wafers were subsequently immersed in water for 1 minute and let dry on a hotplate. In order to obtain the desired thickness (around 100 nm), different sets of parameters for spin coating were tested. The layer thickness was then estimated by means of an ellipsometer. After several trials, we were able to obtain a coating thickness value close to desired one, particularly equal to 102.2 nm. This result was obtained with the following procedure: 1 µl of PMMA 495 was spin coated at a speed of 4000 rpm with acceleration equal to 1000 rpm/s for 45 seconds and then stopped with a deceleration set as well to 1000 rpm/s. Wafers were then baked at 120 °C on a hotplate for 1 minute and then at 185 °C for 2 minutes. Coated wafers were subsequently imaged through the low-magnification IRIS, demonstrating good uniformity. Students and members of the OCN Laboratory are now carrying on this activity, by testing different materials, such as Teflon, optically characterizing the obtained chips and adapting the forward optical model for the estimation of the amount of accumulated biomass.

Chapter 5

Overall conclusions

The research activity that I performed in the course of my PhD regards as main theme the development and application of label-free optical biosensors exploiting interference effects. As principle goal, the development of a refractometric micro-opto-fluidic chemical sensor working in the near-infrared has been pursued. Two main methods of experimental detection have been demonstrated, respectively based on low-coherence interferometry and spectral T/R monitoring. Both methods rely on an all-fiber, easily reconfigurable, measuring system, exploiting broad-band radiation in the near-infrared to perform remote and minimally invasive optical detection. Devices exploited as core-elements of the proposed system were rectangular glass micro-capillaries and the polymeric IBIDI™ VI$^{0.1}$ μ-Slide. All devices present several advantages: they are off-the-shelf low-cost devices, allow to work with low quantities of material, can be easily integrated into an external fluidic system, are realized in materials with good optical properties and offer a flat surface perfectly suitable for the optical imaging.

Read-out radiation was provided by broadband light sources emitting in the near-infrared, in particular a Tungsten lamp with a flat emission spectrum (white light) in the wavelength range 1.3 μm up to 1.6 μm, and two SLED sources emitting an approximately Gaussian spectrum centered respectively around λ_c~1300 nm an λ_c~1550 nm.

Low-coherence interferometry has been applied to the RI detection of homogenous fluids, such as solutions of ethylene glycol and glucose in water, but has been as well demonstrated suitable for the investigation of highly scattering media, such as dairy products and RBCs. As an advanced proof-of-principle, this measuring technique has been applied to the RI detection of normal and malignant population of cells gently confined into rectangular glass micro-capillaries.

Exploiting the SLED source centered around λ_c~1300 nm, providing a higher emitted optical power on a narrower emission wavelength with

respect to the Tungsten lamp, we were able to monitor multiple roundtrip of light through the channel of an IBIDI™ μ-slide, obtaining a maximum sensitivity as high as 177.8×10^3 nm/RIU and best LoD of the order of 10^{-3} RIU. Exploiting the Tungsten lamp, a best LoD of the order of 10^{-4} and a maximum sensitivity $S = 95.7 \times 10^3$ nm/RIU were obtained. When testing rectangular micro-capillaries by means of the Tungsten lamp, LoD of the order of 10^{-3} were obtained, with a maximum sensitivity value equal to 59.11×10^3 nm/RIU.

Exploiting the same equipment, with minor changes to the overall configuration, spectral T/R measurements were as well performed. As the read-out beam provided by a SLED source with central emission wavelength $\lambda_c \sim 1550$ nm was shined orthogonally to the flat long side of a capillary, reflected and transmitted spectra were collected with an OSA. By taking the T/R ratio of the collected data and monitoring the T/R spectra shift as a function of the filling media RI, calibration curves of the implemented sensing system were reconstructed. The evaluation of the T/R ratio allowed to compensate for eventual read-out source fluctuations with no need of an additional monitoring system. Glass microtubes with different combinations of internal channel depth and walls thickness were tested and their sensing performances were related to the relative dimensions of the composing layers. In particular, using glucose solution as test fluids, we obtained sensitivities as high as 530.9 nm/RIU for a capillary providing walls thicknesses $t_f = t_b = 35$ μm and channel depth $d = 50$ μm. All tested devices behaved similarly in terms of LoD, with values in the range of 10^{-5}-10^{-4} RIU. Experimental results were found in accordance with the theoretically expected values obtained through numerical simulations by modeling the device as a cascade of Fabry-Pérot etalons.

Preliminary investigations for translating the spectral shift into intensity measurements at a single wavelength have shown the feasibility of this approach for simple detection of RI variations. The intensity-ratio could be easily attained combining a semiconductor laser source emitting in the traditional telecom wavelength range with two photodiodes for the detection of the transmitted and reflected optical power. This alternative approach would allow to get rid of the OSA, developing a more compact, portable, and cheaper system.

Comparing the results provided by both optical techniques, we found that, despite the higher sensitivity reached through low-coherence interferometry, higher resolution was obtainable exploiting spectral detection methods. On the other side, low-coherence interferometry is an interesting technique since it allows a direct estimation of the RI of the fluids under test. Spectral detection, on the other side, just permits to detect RI variations with respect to a reference value. Moreover, spectral measurements have a limited dynamic range of detection, a problem not occurring when dealing with low-coherence interferometry. These techniques can thus answer to different needs. Low-coherence interferometry is suitable when the RI of a substance need to be directly retrieved, and its application is advised when a wide range of detection is

needed. Spectral detection, on the other side, is better suited when RI monitoring must be achieved on a small range but with high resolution. Further development would regard the actual implementation of a compact setup for intensity measurements at a single wavelength and the incorporation of a temperature control. Moreover, the functionalization of the internal faces of rectangular glass micro-capillaries for demonstration of surface sensitivity is under investigation.

An additional part of my PhD studies have been conducted at the OCN Laboratory of Boston University. In particular, I have applied an interferometry-based imaging system (the low-magnification IRIS) to the label-free monitoring of nucleotide sequences dehybridization induced by temperature variation. The results of my experiments have led to a better understanding of the thermodynamic properties of sequences of interest (KRAS sequences) in cancer investigation for improving rare mutations detection by the SP-IRIS system. Label-free, nucleic acid dehybridization thermodynamic studies showed that melting curves relative to cross-hybridized and fully complementary sequences were sufficiently different if compared one to the other, based on the DNA duplex melting temperature. The proposed method could also be of interest as a tool for the experimental test of primers designing algorithms, and could also be applied to the study of binding and de-binding kinetics of other small particles.

Appendix A

This section treats a minor activity I worked on during the PhD program. It regards the development of structured light systems working in the near-infrared for 3D imaging based on microelectromechanical systems (MEMS). I will firstly describe the employed micro-devices and the realized experimental setup. Then, preliminary results on object depth perception are presented. Results were published in [163][164].

A.1 Infrared structured light generation for 3D imaging

One of the main challenges in imaging system development relies on the ability of collecting 3D images. Most of the existing camera and imaging systems, on the other way, are just able to collect 2D images, completely ignoring the object depth perception. Still, in past several decades a great interest has been addressed to the development of 3D imaging system for 3D object recognition and tracking. Not just research institutes, but also industries, have put a lot of efforts in the realization of new technologies for different applications, with a special consideration to aspects like miniaturization and light source integration. 3D imaging systems are of great impact in consumer gadgets development, in cultural heritage application, reverse engineering, for industrial applications like the inspection of manufactured parts, and others. 3D imaging can be of great interest also in the medical field, with different possible applications, such as body parts tracking and monitoring during surgery. Recently, the increasing availability of new techniques and components helped the production and commercialization of a wide range of products, with measurement resolution as low as few nanometers.

3D imaging systems relying on different operating principles have been developed, such as interferometric measurements, laser triangulation, stereo video visualization, Moiré fringes range contour, shape detection from shadows, shading or focusing and time of flight systems [165].

Time of flight based systems are costly and have low depth resolution even if can work with good acquisition rates and are usually independent by the ambient light. Stereo cameras present different drawbacks, like the high required processing power, the low acquisition data range and the need of high contrast for good image reconstruction. Interferometric techniques, beside their sub-micron accuracy in micro-ranges, are just

applicable to quasi-flat surfaces as well as Moiré fringes range contour, limited to the measurement of smooth surfaces. Laser triangulators are relatively simple systems and can perform at high acquisitions rates, but are costly, slow and can work on a limited range. Systems based on shape by focusing or shadows are simple and low cost but present the weakness of low resolution [165].

As an alternative to the cited methods, a particularly attractive technique for depth detection is represented by structured light. Structured light consists in the projection of a light pattern with a specific and known structure and wavelength on the scene to be filmed, monitored by an image sensor. The pattern can be composed by a sequence of dots or of horizontal and/or vertical lines usually generated using one or more lasers: as a 3D object is present on the scene, the projected light structure undergoes a deformation. The same phenomenon obviously occurs in case of subject movements. Comparing the reference light patterns with the deformed one, through specific image processing and elaboration, is possible to retrieve geometrical information about the 3D objects on the scene, as well to track their movement. Structured light has been applied in a wide range of fields, such as earth science, civil engineering, automotive, super resolution microscopy and medical imaging. The use of the structured light in the medical field is still object of research.

Undoubtedly, the most popular application of structured light is the Kinect™ platform [166] [167] [168]. The Kinect™ makes use of a structured light pattern composed by a sequence of dots. Even if it was created as a gaming platform, its potentialities have been explored in several fields, including the medical one. For example, the Kinect™ platform has been proposed as an aid for the controller-free exploration of medical images in the operating room [168], as well as an aid for the motor learning in patients suffering from spinal muscular atrophy (SMA). The employment of Kinect™ videogames for the carry-out of physical exercise in the older adults has also been proposed [169].

Different structured light approaches for medical application have been as well proposed in the literature: Laughner et al. used a digital light processing (DLP) projector to map the cardiac surface with a structured light approach [170], while in [171] structured light was proposed as a method for head motion tracking in 3D brain imaging. Patterned light was also exploited in super resolution microscopy, where is used to remove the out of focus fluorescence and for depth discrimination [172]–[174].

Together with the spreading of the applications that benefit from the use of structured light, a growing interest is addressed to the development of miniaturized and innovative systems able to generate patterned light. Particularly interesting are those working in the infrared region, as they do not interfere with imaging systems working with visible light; moreover, infrared radiation is invisible to the human eye, an additional advantage for example in medical applications, where the projection of visible light could create discomfort to the patient.

In our laboratory, we demonstrated the functionality of a single-axis torsional micro-mirror realized with MEMS technology combined with silicon microstructures as diffractive optical elements working in reflection for the generation of structured light suitable for the 3D recognition of objects. We focused on the development of a compact system able to generate a pattern of light with known geometry, composed by a CMOS camera, a light source, a mirror and a diffractive element. Briefly, light generated by a laser diode emitting in the near infrared impinges on the torsional micro-mirror, electrostatically actuated. Reflected light reaches a silicon diffractive structure, which reflects the light on a target at known distance, creating a diffractive pattern. Next paragraphs provide details about the employed miniaturized components, as well as on the developed setup. Finally, experimental results about object depth perception obtained with the realized system are presented.

A.2 MEMS micro-mirrors and silicon diffractive structures

The central elements of the proposed system for the generation of patterned light are torsional MEMS micro-mirrors and silicon diffractive structures. All used miniaturized devices were manufactured by STMicroelectronics. We employed different kind of diffractive structures, differing by the pitch dimension. Regarding the micro-mirrors, a HG6 silicon micro-mirror was employed, a picture of which is shown in Figure A.1.
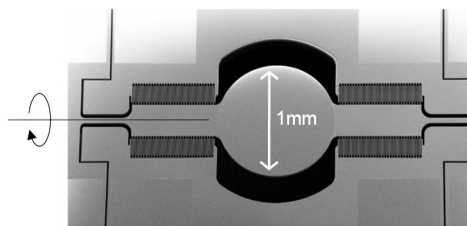
Figure A.1 Picture of a torsional MEMS micro-mirror HG6 (STMicroelectronics).

The silicon micro-mirror is a MEMS device composed by a circular reflective mirror of diameter equal to 1 mm. The mirror, i.e. the rotor, is suspended on a cavity and linked to the supporting structure through two springs (the stators). Rotor and stators are equipped with comb-fingers, employed for the electrostatic actuation of the mirror.

The micro-mirror can be considered an analog device as the torsional angle can be varied in a continuous way. When actuated, the silicon

structure rotates at the frequency of the torsional mode, about 25 kHz. The MEMS chip was mounted and wire bonded to a custom-designed printed circuit board with electrical connection, fixed to a micropositioner stage moving along the x-y-z axis and mounted with the rotational axis perpendicular to the optical table plane. The mirror can undergo a torsion equal to ±12°, thus resulting in a maximum scan of the laser beam equal to ±24°.

All diffractive micro-structures were fabricated with the ThELMA process, (*Thick Epipoly Layer for Microactuators and Accelerometers*), developed by STMicroelectronics specifically for the production of MEMS devices. The technique consists in growing layers of polysilicon on a silicon substrate, where a layer of sacrificial oxide is grown as well. This last layer is then removed through treatment with acids, creating polysilicon suspended masses, eventually able to rotate if electrostatically actuated. The resulting structures are formed by periodic arrays of parallel polysilicon rectangular stripes; if shined with a light beam, they behave as reflection amplitude diffraction gratings. We employed structures with stripes length equal to 400/500 µm, separated of 2 µm, and pitch (p) between 10 µm and 23.8 µm. These structures are also called "Venetian blind" structures. Figure A.2 shows optical microscopy images of a chip including four different kind of employed diffractive devices, while Figure A.3. reports the image of an additional diffractive structure with array pitch p = 23.8 µm, length L = 500 µm and height H = 480 µm.
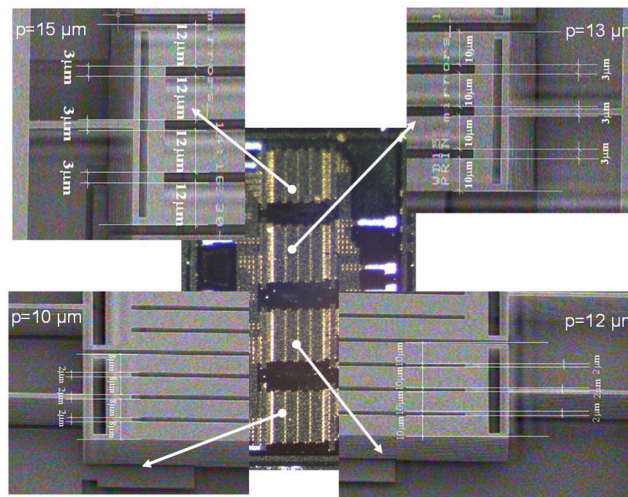
Figure A.2 Picture taken with an optical microscope of a chip including four "Venetian blind" diffractive structures consisting of periodic arrays of parallel poly-silicon stripes with different array pitch on a single chip (p=10, 12, 13, 15 µm). The insets show details about the different diffractive structures.
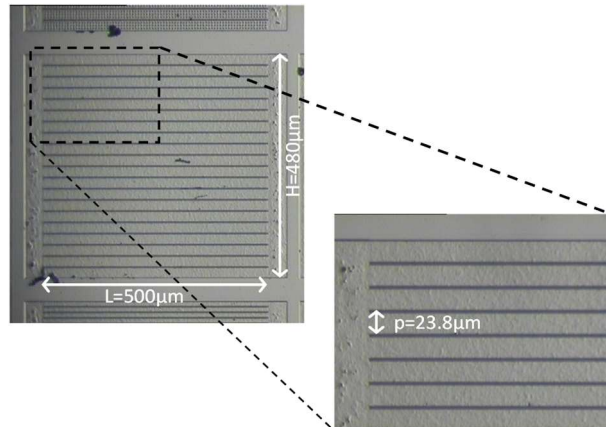
Figure A.3 Picture taken with an optical microscope of a "Venetian blind" diffractive structure consisting of periodic arrays of parallel poly-silicon stripes with array pitch p = 23.8 µm.

A.4 Principle of operation and setup for object depth perception

As stated before, structured light consists in a light distribution with specific and known geometrical characteristic. Through the presented silicon structures (micro-mirrors and diffractive structures), we were able to project on the target a pattern of horizontal stripes with uniform spacing. The principle of operation can be better understood looking at Figure A.4 and A.5. In Figure A.4, a laser diode projects a light beam on the mirror, placed at 45° with respect to the beam direction. The beam is again reflected at 90° with respect to his original direction, and reaches a second reflective structure, again placed at 45°. The beam is finally redirected on the target, and the scene is filmed by a camera. If the mirror is un-actuated, as in Figure A.4(a), the camera captures a single light dot. As the mirror is actuated, and thus rotating, the light beam is translated, and the captured image is a line, being one frame acquired in 33 ms, thus a time much longer than the rotational period T= 0.04 ms of the mirror.

In Figure A.5 instead, the second reflector is replaced by a diffractive structure; when the mirror is fixed, as in Figure A.5(a), the projected pattern consists in a sequence of vertical dots along the direction perpendicular to the silicon stripes. The dots spacing is inversely proportional to the array pitch and the sequence corresponds to the various orders of diffraction of the grating. Finally, Figure A.5(b) represents the actual experimental configuration: the MEMS mirror is rotating and scanning the laser beam onto the diffractive microstructure. The light spots projected on the target are translated and the detected light pattern appears as a sequence of horizontal bright lines.
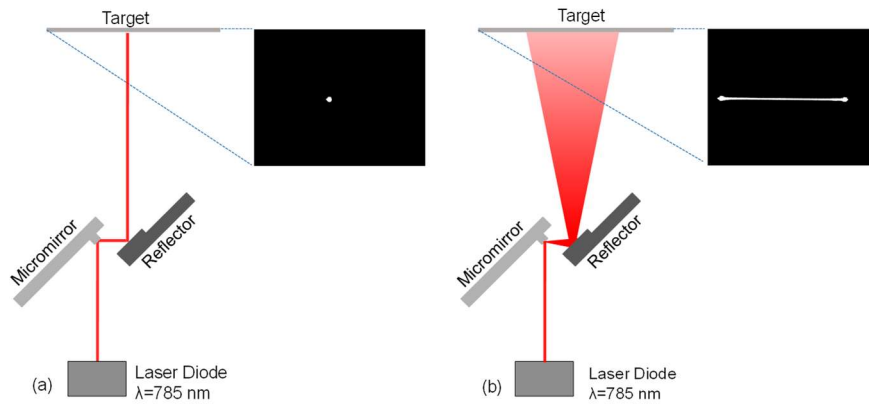
Figure A.4 Illustration of the operating principle of the silicon microsystem for patterned light projection and detection. (a) Projected picture by two reflective mirrors collected by a CMOS camera with a laser diode source. (b) Image generated when the MEMS micromirror is rotating and scanning the laser beam onto a reflective surface. LD: Laser Diode
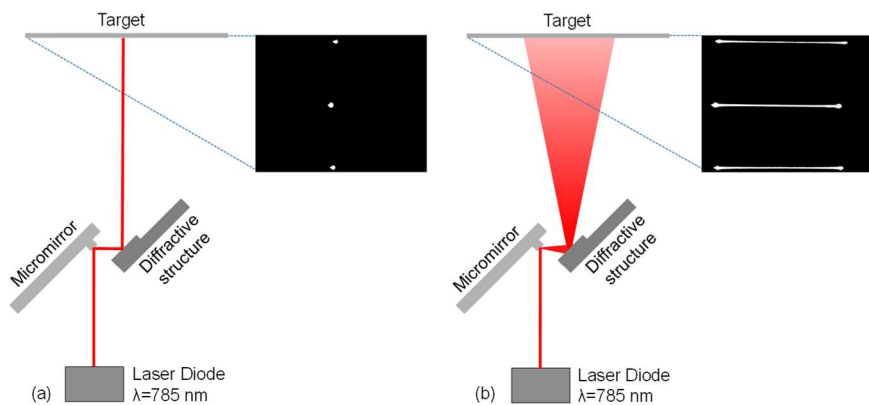
Figure A.5 Illustration of the operating principle of the silicon microsystem for patterned light projection and detection. Images are generated as the MEMS mirror is redirecting the laser beam on a diffractive reflective microstructure, being (a) in static position, (b) rotating. LD: Laser diode.

Figure A.6 represent a schema of the final experimental configuration and a picture of the real laboratory setup. A laser diode emitting in the near infrared at λ = 785 nm (Hitachi HL7851G) was employed. These devices present several advantages: they are commercially available at low cost, are compact, important factor in view of the realization of a miniaturized system, and work in a wavelength region invisible to the human eye. The light beam generated by the laser impinged on the micro-mirror with an angle of 45° and was reflected at 90° (respect to the original direction). The mirror was mounted with the torsional axis perpendicular to the optical table. The reflected laser beam impinged on a silicon diffractive structure,

again placed at 45° respect to the beam, and finally reached the target, filmed through a CMOS camera (IDS UI-3240CP-NIR-G) with enhanced sensitivity in the NIR and resolution of 1280 x 1024 pixels. The camera mounted a 25-mm objective lens with variable focus and aperture (max aperture ratio: 1.4). The mirror and the diffractive structure was positioned at a distance equal to 2 mm, while the camera was placed at a distance d=7.1 cm above the diffractive structure and connected to a PC. The distance between the mirror and the target was equal to l = 50 cm. We piloted the mirror with a positive square wave at about 50 kHz (twice the resonance frequency) and duty cycle of 25% to optimize the actuation efficiency.
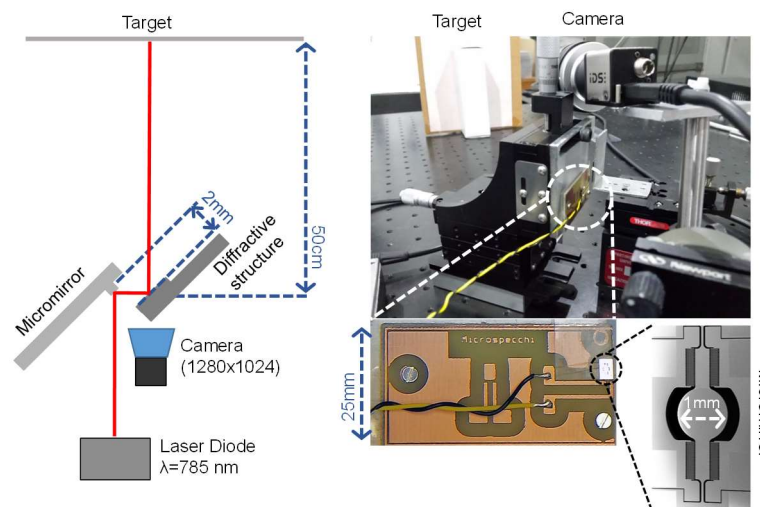
Figure A.6 Left: schema of the instrumental configuration employed for the generation of structured light. Right: picture of the experimental setup with details about the printed circuit board holding the micro-mirror and the micro-mirror itself.

As stated before the mirror can rotate of ± 12°, resulting in a laser scanning angle equal to ± 24°. The length of the light projected lines depends on the distance. In order to minimize the losses, the projected beam must lie within the boundaries of the diffractive structure. The distance of 2 mm between mirror and diffractive structure wasn't sufficient to exploit all the rotation angle of the mirror. Keeping the distance constant, a silicon structure with stripes length about 4 mm, obtainable with micromachining techniques, would be necessary in order to exploit the whole mirror dynamic.

A.5 Experimental results

According to the diffraction theory, when working in far field, the intensity profile of the diffraction pattern can be calculated through the

Fraunhofer diffraction equation, and the distance s between two consecutive orders can be approximated by the relation:

$$s = \frac{\lambda * l}{p}$$

(62)

where λ is the source emitted wavelength, l is the distance between the diffractive structure and the target and p the array pitch. Here, $\lambda = 785$ nm and $l = 50$ cm. It is evident from Eq. 62 as structures with higher pitch must result in closer projected light stripes. We tested different diffractive structures, with pitch p equal to 10, 12, 13, 15 µm, resulting in spacing s respectively equal to 39.2 mm, 32.7 mm, 30.2 mm and 26.2 mm. As can be seen in Figure A.7, the distance between the different diffraction order was inversely proportional to the array pitch, according to what theoretically expected. The brighter central line represents the zero diffraction order.
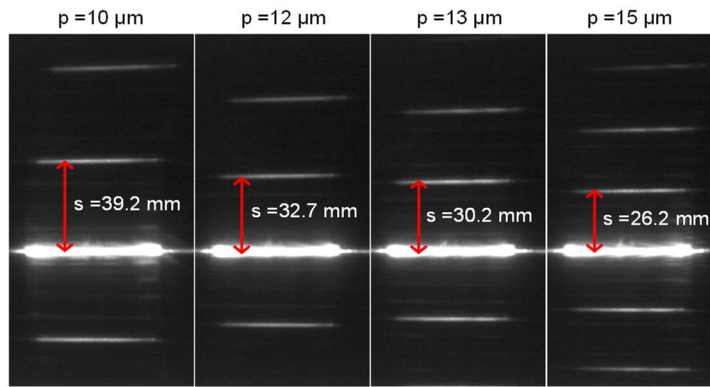
Figure A.7 Light patterns generated with diffractive structure with different array pitch p captured by a CMOS camera. The spacing s between consecutive diffraction is inversely proportional to the pitch p.

As a proof of concept, we applied the proposed system to the generation of patterned light for the detection of object depth. For the test, we used a card-box with a square cross-section and side length of 1 cm and a second square box with side length equal to 5 cm. It is clear from what shown above that the bigger is the diffractive structure array pitch the better is the obtained vertical resolution of the generated structured light pattern. For this reason, we selected the diffractive structure with p = 23.8 µm, resulting in a spacing s = 16.5 mm. Figure A.8 shows the objects placement and the obtained light pattern when they were present on the filmed scene, as well as the un-deformed one. In particular, Figure A.8(b) shows the un-deformed light pattern projected on the target when no object was present. Figure A.8(d) and (e) show the deformed patterned due to the presence of 3D objects (respectively placed as in Figure A.8(a) and (c)).
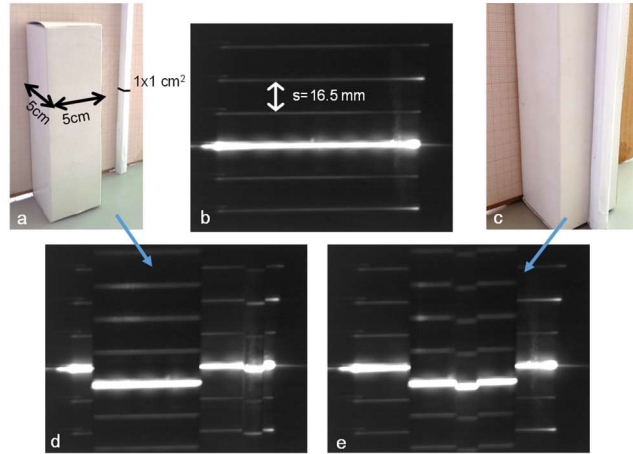
Figure A.8 Card-boxes with square cross-section and side length of 5 and 1 cm, placed (a) side by side, (c) one in front of the other. Light patterns generated by a diffractive structure with array pitch p= 23.8 µm captured by a CMOS camera: (b) when no object was present on the scene, (d) when the objects were placed as in (a) and (e) when the objects where placed as in (c).

The camera acquires gray scale image with a resolution of 1280 X 1024 pixels and 8 b for pixel. For convenience, the shown images were cropped in a square matrix of 1024 x 1024 pixels. It can be seen as the zero order of diffraction was much brighter than the others. In order to obtain a pattern with uniform intensity, we converted the 8-b gray scale images (256 levels) in 1-b black and white (2 levels) images. Given the different intensity of the various order of diffraction, different threshold levels were applied to different region of the image: a threshold equal to 200 was applied to the region around the zero order, whereas a threshold of 50 was used everywhere else. All pixel with grayscale level higher than the threshold were set to 1 (white), while all remaining were set to 0 (black). Figure A.9 shows the result of the thresholding applied to Figure A.8(e).
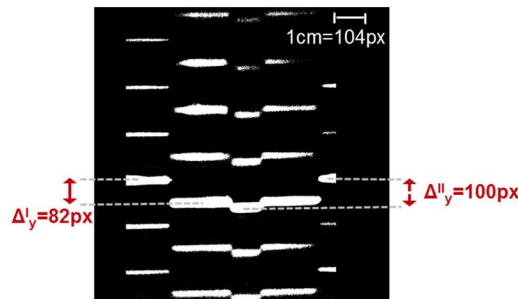
Figure A.9 Result of the application of a progressive threshold to Figure A.8(e). Δ^{I}_{y}: distance between the un-deformed line due to the background target and the deformed line relative to the larger card-box. Δ^{II}_{y}: distance between the un-deformed line due to the background target and the deformed line relative to the superposition of both boxes. px = pixels.

113

In the same figure is as well highlighted the pixel shift caused by the presence of 3D objects, taken as the distance between the un-deformed lines in the background and the line of the same order deformed by the objects. The larger box caused a shift $\Delta^I = 82$ pixels, while the two superimposed objects lead to $\Delta^{II} = 100$ pixels. From these values, and knowing the distance between the various setup components, it's possible to retrieve the depth a of the object. In particular, the object depth can be obtained as:

$$a = \frac{l * \Delta_{y-m}}{\Delta_{y-m} + c} \tag{66}$$

with l the distance between the camera and the target, c the vertical distance between the grating and the camera and Δ_{y-m} the shift of the lines after conversion of pixels in metric units of length. Figure A.10 clarifies the applied relationship, where $l = 50$ cm and $c = 7.1$. By applying the conversion 1 cm = 104 pixels, we retrieved depth values $a = 4.99$ cm $\pm$ 0.07 cm for the bigger card box, while for the two superimposed objects we obtained an overall depth $a = 5.96$ cm $\pm$ 0.07 cm. The obtained values are in good agreement with the geometrical depth of the objects under test. The reported error, equal to $\pm$ 0.07 cm was estimated considering the maximum obtainable resolution, i.e. 1 pixel, thus corresponding to the minimum measurable Δy, converting it to metric units and applying Eq. 66.

For what concerns the limit of detection of the system, with the employed setup configuration, we can consider the minimum detectable depth of the order of 1 mm. In fact, even if the projected light stripes have a quite broad profile, it is possible to detect their central position through image elaboration. Anyway, the employed optical setup, in particular the collimating lens, it is not optimized to reach the best possible resolution, and the diameter of the light beam generated on the target has a size that is much bigger than 1 pixel. With suitably chosen optical components, it would be possible to further decrease the minimum detectable object depth.
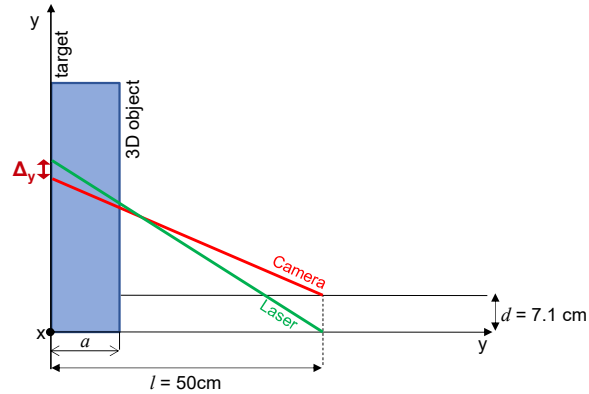
Figure A.10 Schematic cross-section of the scene. Δ_y: line shift; a: depth of the object; l: distance between background target and camera; c: vertical distance between the camera and diffractive element.

The proposed method resulted successful for the generation of IR structured light suitable for 3D imaging. Indeed, the depth of simple 3D was retrieved with good accuracy. The use of a low-power and commercially available light source emitting in the near infrared, invisible to the human eye, allowed the realization of a safe system employable even, for example, for face imaging. In the presented test, all components were separately mounted on the optical table: anyway, it would be easy to create a compact and miniaturized system hosting the light source, the silicon structures (i.e. the MEMS mirror and the diffractive grating) and the image sensor. The high frequency of the mirror rotation leads to a fast operating system, suitable also for rapid movements tracking. Further improvements of the proposed system would regard the use of different diffractive structure with longer rectangular stripes. In fact, as mentioned before, to keep the projected light beam within the boundaries of the silicon gratings, at a distance of 2 mm from the mirror, its rotational angle had to be limited. In order to exploit all the mirror dynamic, keeping the same distance d, a diffractive grating with length l = 4 mm would be required, feasible with micromachining techniques. This solution would provide 45-cm-long projected lines at a 50-cm distance, allowing a larger scene to be monitored. Additionally, it would be possible to create more elaborated structured light patterns through modulation of the laser driving current, and thus its emitted power.

References

[1]   Bakerian Lecture. Experiments and calculations relative to physical optics," *Phil. Trans. R. Soc. Lond.*, vol. 94, no. 94, pp. 1–16, 1804.

[2]   M. Norgia, S. Donati, and D. D'Alessandro, "Interferometric measurements of displacement on a diffusing target by a speckle tracking technique," *IEEE J. Quantum Electron.*, vol. 37, no. 6, pp. 800–806, 2001.

[3]   H. K. Hunt and A. M. Armani, "Label-free biological and chemical sensors," *Nanoscale*, vol. 2, no. 9, pp. 1544–1559, 2010.

[4]   I. M. White and X. Fan, "On the performance quantification of resonant refractive index sensors," *Opt. Express*, no. 2, pp. 117–127, 2008.

[5]   W. W. Lam, L. H. Chu, C. L. Wong, and Y. T. Zhang, "A surface plasmon resonance system for the measurement of glucose in aqueous solution," *Sensors Actuators B. Chem.*, vol. 105, no. 2, pp. 138–143, 2005.

[6]   X. Yang, L. Ying, B. Liu, and J. Yao, "Simultaneous measurement of refractive index and temperature based on SPR in D -shaped MOF," *Appl. Opt.*, vol. 56, no. 15, pp. 4369–4374, 2017.

[7]   Y. Al-Qazwini, A. S. M. Noor, Z. Al-Qazwini, M. H. Yaacob, S. W. Harun, and M. A. Mahdi, "Refractive index sensor based on SPR in symmetrically etched plastic optical fibers," *Sensors Actuators A. Phys.*, vol. 246, pp. 163–169, 2016.

[8]   T. Hu, Y. Zhao, and A. Song, "Fiber optic SPR sensor for refractive index and temperature measurement based on MMF-FBG-MMF structure," *Sensors Actuators B. Chem.*, vol. 237, pp. 521–525, 2016.

[9]   C. Zhang, Z. Li, S. Zhen, C. Hui, S. Cai, and J. Yu, "U-bent fiber optic SPR sensor based on graphene / AgNPs," *Sensors Actuators B. Chem.*, vol. 251, pp. 127–133, 2017.

[10] Z. Lei, X. Zhou, J. Yang, X. He, Y. Wang, and T. Yang, "Second-order distributed-feedback surface plasmon resonator for single-mode fiber end-facet biosensing," *Appl. Phys. Lett.*, vol. 110, no. 17, pp. 171107-1-5, 2017.

[11] J. Dostalek, J. Ctyroky, J. Homola, E. Brynda, M. Skalsky, P. Nekvinodva, J. Spirkova, J. Skvor, and J. Schrofel, "Surface plasmon resonance biosensor based on integrated optical waveguide," *Sensors Actuators, B Chem. Phys.*, vol. 76, pp. 8-12, 2001.

[12] A. Suzuki, J. Kondoh, Y. Matsui, and K. Suzuki, "Development of novel optical waveguide surface plasmon resonance (SPR) sensor with dual light emitting diodes," *Sensors Actuators B. Chem.*, vol. 106, no. 1, pp. 383–387, 2005.

[13] C. Ciminelli, C. M. Campanella, F. Dell'Olio, C. E. Campanella, and M. N. Armenise, "Label-free optical resonant sensors for biochemical applications," *Prog. Quantum Electron.*, vol. 37, no. 2, pp. 51–107, Mar. 2013.

[14] E. Makarona, P. Petrou, S. Kakabakos, K. Misiakos, and I. Raptis, "Point-of-Need bioanalytics based on planar optical interferometry," *Biotechnol. Adv.*, vol. 34, no. 3, pp. 209–233, 2016.

[15] B. H. Lee, Y. H. Kim, K. S. Park, J. B. Eom, M. J. Kim, B. S. Rho, and H. Y. Choi, "Interferometric Fiber Optic Sensors," *Sensors*, vol. 12, pp. 2467–2486, 2012.

[16] B. Y. Shew, Y. C. Cheng, and Y. H. Tsai, "Monolithic SU-8 micro-interferometer for biochemical detections," *Sensors Actuators A Phys.*, vol. 141, pp. 299–306, 2008.

[17] A. Dér, S. Valkai, A. Mathesz, I. Andó, E. K. Wolff, and P. Ormos, "Chemical Protein-based all-optical sensor device," *Sens. Actuators B Chem.*, vol. 151, pp. 26–29, 2010.

[18] E. F. Schipper, A. M. Brugman, C. Dominguez, L. M. Lechuga, R. P. H. Kooyman, and J. Greve, "The realization of an integrated Mach-Zehnder waveguide immunosensor in silicon technology," *Sens. Actuators B Chem* , vol. 40, pp. 147–153, 1997.

[19] Q. Liu, Z. Gu, M. K. Park, and J. Chung, "Experimental demonstration of highly sensitive optical sensor based on grating-assisted light coupling between strip and slot waveguides," *Opt. Express*, vol. 24, no. 12, pp. 3399–3405, 2016.

[20] F. Brosinger, H. Freimuth, M. Lacher, W. Ehrfeld, E. Gedig, A. Katerkamp, F. Spener, and K. Cammann, "A label-free affinity sensor with compensation of unspecific protein interaction by a highly sensitive integrated optical Mach-Zehnder interferometer on silicon," *Sens. Actuators B Chem.*, vol. 44, pp. 350–355, 1997.

[21] R. G. Heideman and P. V Lambeck, "Remote opto-chemical sensing with extreme sensitivity : design , fabrication and performance of a pigtailed integrated optical phase-modulated Mach-Zehnder interferometer system," *Sensors Actuators B. Chem.*, vol. 61, pp. 100–127, 1999.

[22] Y. Gao, Q. Gan, Z. Xin, X. Cheng, and F. J. Bartoli, "Plasmonic Mach-Zehnder interferometer for ultrasensitive on-chip biosensing," *ACS Nano*, vol. 5, no. 12, pp. 9836–9844, 2011.

[23] Z. Li, C. Liao, D. CHen, J. Song, W. Jin, G.-D. P. Peng, F. Zhu, Y. Wang, H. Jun, and Y. Wang, "Label-free detection of bovine serum albumin based on an in-fiber Mach-Zehnder interferometric biosensor," *Opt. Express*, vol. 25, no. 15, pp. 17105–17113, 2017.

[24] J. M. Schmitt, "Optical coherence tomography (OCT): a review," *IEEE J. Sel. Top. Quantum Electron.*, vol. 5, no. 4, pp. 1205–1215, 1999.

[25] J. Zhang, H. Sun, R. Wang, D. Su, and T. Guo, "Simultaneous Measurement of Refractive Index and Temperature Using a Michelson Fiber Interferometer With a Hi-Bi Fiber Probe," *IEEE Sensors Journal*, vol. 13, no. 6, pp. 2061–2065, 2013.

[26] J. Zhou, Y. Wang, C. Liao, B. Sun, J. He, G. Yin, S. Liu, Z. Li, G. Wang, X. Zhong, and J. Zhao, "Intensity modulated refractive index sensor based on optical fiber Michelson interferometer," *Sensors Actuators B Chem.*, vol. 208, pp. 315–319, 2015.

[27]   Z. Tian, S. S.-H. Yam, and H.-P. Loock, "Refractive index sensor based on an abrupt taper Michelson interferometer in a single-mode fiber," *Opt. Lett.*, vol. 33, no. 10, pp. 1105–1107, 2008.

[28]   L. Ahmadi, M. Hiltunen, P. Stenberg, J. Hiltunen, S. Aikio, M. Roussey, J. Saarinen, and S. Honkanen, "Hybrid layered polymer slot waveguide Young interferometer," *Opt. Express*, vol. 24, no. 10, pp. 8089–8094, 2016.

[29]   A. Ymeti, J. S. Kanger, J. Greve, G. A. J. Besselink, P. V Lambeck, R. Wijn, and R. G. Heideman, "Integration of microfluidics with a four-channel integrated optical Young interferometer immunosensor," *Biosens. Bioelectron.*, vol. 20, pp. 1417–1421, 2005.

[30]   K. Schmitt, B. Schirmer, C. Hoffmann, A. Brandenburg, and P. Meyrueis, "Interferometric biosensor based on planar optical waveguide sensor chips for label-free detection of surface bound bioreactions," *Biosens. Bioelectron.*, vol. 22, pp. 2591–2597, 2007.

[31]   D. Duval, A. B. Gonzalez-Guerrero, S. Dante, J. Osmond, R. Monge, J. Luis, K. E. Zinoviev, C. Domınguez, and L. M. Lechuga, "Nanophotonic lab-on-a-chip platforms including novel bimodal interferometers , microfluidics and grating couplers," *Lab Chip*, vol. 12, pp. 1987–1994, 2012.

[32]   K. E. Zinoviev, A. B. González-guerrero, C. Domínguez, and L. M. Lechuga, "Integrated Bimodal Waveguide Interferometric Biosensor for Label-Free Analysis," *J. Light. Technol.*, vol. 29, no. 13, pp. 1926–1930, 2011.

[33]   Y. Liu and S. Qu, "Optical fiber Fabry – Perot interferometer cavity fabricated by femtosecond laser-induced water breakdown for refractive index sensing," *Appl. Opt.*, vol. 53, no. 3, pp. 469–474, 2014.

[34]   X. Li, Y. Shao, Y. Yu, Y. Zhang, and S. Wei, "A Highly Sensitive Fiber-Optic Fabry–Perot Interferometer Based on Internal Reflection Mirrors for Refractive Index Measurement," *Sensors*, vol. 16, no. 6, p. 794, 2016.

[35]   C. Wu, Z. Liu, A. P. Zhang, B. Guan, and H. Tam, "In-line open-cavity Fabry-Pérot interferometer formed by C-shaped fiber for temperature-insensitive refractive index sensing," *Opt. Express*, vol. 22, no. 18, pp. 21757-66, 2014.

[36] S. Surdo, F. Carpignano, L. M. Strambini, S. Merlo, and G. Barillaro, "Capillarity-driven (self-powered) one-dimensional photonic crystals for refractometry and (bio)sensing applications," *RSC Adv.*, vol. 4, no. 94, pp. 51935–51941, 2014.

[37] S. Mandal, J. M. Goddard, and D. Erickson, "A multiplexed optofluidic biomolecular sensor for low mass detection," *Lab Chip*, vol. 9, no. 20, pp. 2924–2932, 2009.

[38] D. Yang, H. Tian, and Y. Ji, "Nanoscale photonic crystal sensor arrays on monolithic substrates using side-coupled resonant cavity arrays," *Opt. Express*, vol. 19, no. 21, pp. 11709–11717, 2011.

[39] S. Wang, X. Sun, C. Wang, G. Peng and Y. Qi, "Liquid refractive index sensor based on a 2D 10-fold photonic quasicrystal*," J. Phys. D: Appl. Phys* , vol. 50, no. 36, p. 365102-1–365102-6, 2017.

[40] J. Wu, D. Day, M. Gu, J. Wu, D. Day, and M. Gu, "A microfluidic refractive index sensor based on an integrated three-dimensional photonic crystal," *Appl. Phys. Lett.*, vol. 92, no. 7, pp. 71108-1–71108-3, 2008.

[41] A. N. Chryssis, S. S. Saini, S. M. Lee, H. Yi, W. E. Bentley and M. Dagenais "Detecting Hybridization of DNA by Highly Sensitive Grating Sensors," *IEEE J. Quantum Electron.*, vol. 11, no. 4, pp. 864–872, 2005.

[42] K. Schroeder, W. Ecke, R. Mueller, R. Willsch, and A. Andreev, "A fibre Bragg grating refractometer," *Meas. Sci. Technol.*, vol. 12, pp. 757–764, 2001.

[43] M. C. P. Huy, G. Laffont, V. Dewynter, P. Ferdinand, P. Roy, J. Auguste, D. Pagnoux, W. Blanc, and B. Dussardier, "Three-hole microstructured optical fiber for efficient fiber Bragg grating refractometer," *Opt. Lett.*, vol. 32, no. 16, pp. 2390–2392, 2007.

[44] A. Sun and Z. Wu, "A Hybrid LPG/CFBG for Highly Sensitive Refractive Index Measurements," *Sensors*, vol. 12, no. 6, pp. 7318–7325, 2012.

[45] X. Wang and O. S. Wolfbeis, "Fiber-Optic Chemical Sensors and Biosensors (2013 − 2015)," *Anal. Chem.*, vol. 88, pp. 203–227, 2016.

[46] C. A. Barrios, "Optical Slot-Waveguide Based Biochemical Sensors," *Sensors*, vol. 9, no. 6, pp. 4751–4765, 2009.

[47] Q. Xu, V. R. Almeida, R. R. Panepucci, and M. Lipson, "Experimental demonstration of guiding and confining light in nanometer-size low-refractive-index material," *Opt. Lett.*, vol. 29, no. 14, pp. 1626–1628, 2004.

[48] V. M. N. Passaro, F. D. Olio, C. Ciminelli, M. N. Armenise, and P. Bari, "Efficient Chemical Sensing by Coupled Slot SOI Waveguides," *Sensors*, vol. 9, no. 2, pp. 1012–1032, 2009.

[49] C. a. Barrios, M. J. Bañuls, V. González-Pedro, K. B. Gylfason, B. Sánchez, A. Griol, A. Maquieira, H. Sohlström, M. Holgado, and R. Casquel, "Label-free optical biosensing with slot-waveguides.," *Opt. Lett.*, vol. 33, no. 7, pp. 708–710, 2008.

[50] J. T. Robinson, L. Chen, and M. Lipson, "On-chip gas detection in silicon optical microcavities," *Opt. Express*, vol. 16, no. 6, pp. 4296–4301, 2008.

[51] T. Claes and J. Giron, "Label-free biosensing with silicon-on-insulator slotted racetrack resonator Waveguide design," in *Proceedings Symposium IEEE/LEOS Benelux Chapter*, 2008, pp. 23–26.

[52] A. Di Falco, L. O'Faolain, and T. F. Krauss, "Chemical sensing in slotted photonic crystal heterostructure cavities," *Appl. Phys. Lett.*, vol. 94, no. 6, p. 63503, 2009.

[53] A. N. Oraevsky, "Whispering-gallery waves," *Quantum Electron.*, vol. 32, no. 5, pp. 377–400, 2002.

[54] G. Kim, G. Son, H. Lee, K. Kim, and S. Lee, "Integrated photonic glucose biosensor using a vertically coupled microring resonator in polymers," *Opt. Commun.*, vol. 281, pp. 4644–4647, 2008.

[55] H. Sohlstrom and M. Oberg, "Refractive index measurements using integrated ring resonators," in *EICO'97, 8th European Conference on Integrated Optics*, 1997, pp. 322–325.

[56] T. Claes, W. Bogaerts, and P. Bienstman, "Experimental characterization of a silicon photonic biosensor consisting of two cascaded ring resonators based on the Vernier-effect and introduction of a curve fitting method for an improved detection limit," *Opt. Express*, vol. 18, no. 22, pp. 22747–22761, 2010.

[57] C. A. Barrios, K. B. Gylfason, B. Sánchez, A. Griol, H. Sohlström, M. Holgado, and R. Casquel, "Slot-waveguide biochemical sensor," *Opt. Lett.*, vol. 32, no. 21, pp. 3080–3082, 2007.

[58] M. Sumetsky, R. S. Windeler, Y. Dulashko, and X. Fan, "Optical liquid ring resonator sensor," *Opt. Express*, vol. 15, no. 22, pp. 14376–14381, 2007.

[59] H. Li and X. Fan, "Characterization of sensing capability of optofluidic ring resonator biosensors," *Appl. Phys. Lett.*, vol. 97, no. 1, p. 11105, 2010.

[60] T. Tsuda, J. V. Sweedler, and R. N. Zare, "Rectangular capillaries for capillary zone electrophoresis," *Anal. Chem.*, vol. 62, no. 19, pp. 2149–2152, 1990.

[61] N. M. M. Pires, T. Dong, U. Hanke, and N. Hoivik, "Recent developments in optical detection technologies in lab-on-a-chip devices for biosensing applications," *Sensors*, vol. 14, no. 8, pp. 15458–15479, 2014.

[62] J. O. Harris, "Techniques and experiments," 1975. [Online]. Available: http://www.vitrocom.com/pdf/VITROTUBES-techniques-experiments.pdf.

[63] B. Hammarström, M. Evander, H. Barbeau, M. Bruzelius, J. Larsson, T. Laurell, and J. Nilsson, "Non-contact acoustic cell trapping in disposable glass capillaries," *Lab Chip*, vol. 10, no. 17, pp. 2251–2257, 2010.

[64] M. Evander and M. Tenje, "Microfluidic PMMA interfaces for rectangular glass capillaries," *J. Micromechanics Microengineering*, vol. 24, no. 2, p. 27003, 2014.

[65] B. Hammarström, M. Evander, J. Wahlström, and J. Nilsson, "Frequency tracking in acoustic trapping for improved performance stability and system surveillance," *Lab Chip*, vol. 14, no. 5, pp. 1005–13, 2014.

[66] W. Morrish, P. West, N. Orlando, E. Klantsataya, K. Gardner, S. Lane, R. Decorby, A. François, and M. ALkiviathes, "A Refractometric Micro-Sensor Using a Mirrored Capillary Resonator," *Opt. Express*, vol. 94, no. 2009, pp. 21540–21551, 2016.

[67] T. Tsuda, J. V. Sweedler, and R. N. Zare, "Rectangular capillaries for capillary zone electrophoresis," *Anal. Chem.*, vol. 62, no. 19, pp. 2149–2152, 1990.

[68] Y. Temiz, R. D. Lovchik, G. V. Kaigala, and E. Delamarche, "Lab-on-a-chip devices: How to close and plug the lab?," *Microelectron. Eng.*, vol. 132, pp. 156–175, 2015.

[69] Ibidi®, "µ–Slide VI 0.1," 2014. [Online]. Available: http://ibidi.com/xtproducts/en/ibidi-Labware/Channel-Slides/m-Slide-VI-0.4.

[70] J. Liebl, S. B. Weitensteiner, L. Taka, R. Fu, and A. M. Vollmar, "Cyclin-dependent kinase 5 regulates endothelial cell migration and angiogenesis," *J. Biol. Chem.*, vol. 285, no. 46, pp. 35932–35943, 2010.

[71] A. Ganguly, H. Zhang, R. Sharma, S. Parsons, and K. D. Patel, "Isolation of Human Umbilical Vein Endothelial Cells and Their Use in the Study of Neutrophil Transmigration Under Flow Conditions," *J. Vis. Exp.*, vol. 66, pp. 160–174, 2012.

[72] N. E. Ashpole, D. R. Overby, C. R. Ethier, and W. D. Stamer, "Shear Stress-Triggered Nitric Oxide Release From Schlemm's Canal Cells," *Invest. Ophthalmol. Vis. Sci.*, vol. 55, pp. 8067-8076, 2017.

[73] F. Carpignano, G. Rigamonti, and S. Merlo, "Characterization of rectangular glass microcapillaries by low-coherence reflectometry," *IEEE Photonics Technol. Lett.*, vol. 27, no. 10, pp. 1064–1067, 2015.

[74] G. Rigamonti, S. Merlo, and F. Carpignano, "Rectangular glass micro-capillaries for biophotonic applications," in *2015 Fotonica AEIT Italian Conference on Photonics Technologies*, 2015, pp. 5–8.

[75] F. Carpignano, G. Rigamonti, G. Mazzini, and S. Merlo, "Low-Coherence Reflectometry for Refractive Index Measurements of Cells in Micro-Capillaries," *Sensors,* vol. 16, no. 10, 2016.

[76] G. Rigamonti, M. Guardamagna, and S. Merlo, "Non-contact reflectometric read-out of disposable microfluidic devices by near infra-red low-coherence interferometry," *AIMS Biophys.,* vol. 3, no. 4, pp. 585–595, 2016.

[77] A. Ymeti, J. Greve, P. V Lambeck, T. Wink, T. A. M. Beumer, and R. R. Wijn, "Fast , Ultrasensitive Virus Detection Using a Young Interferometer Sensor," *Nano Lett.*, vol. 7, no. 2, pp. 394–397, 2007.

[78] V. S. Lin, K. Motesharei, K. S. Dancil, M. J. Sailor, and M. R. Ghadiri, "A Porous Silicon-Based Optical Interferometric Biosensor," *Science*, vol. 278, no. 5339, pp. 840-3, 1997.

[79] P. Lu, L. Men, K. Sooley, Q. Chen, P. Lu, L. Men, K. Sooley, and Q. Chen, "Tapered fiber Mach – Zehnder interferometer for simultaneous measurement of refractive index and temperature," *Appl. Phys. Lett.* vol. 94, no. 13, p. 131110, 2009.

[80] T. Wei, Y. Han, Y. Li, H.-L. Tsai, and H. Xiao, "Temperature-insensitive miniaturized fiber inline Fabry-Pérot interferometer for highly sensitive refractive index measurement," *Opt. Express*, vol. 16, no. 8, p. 5764, 2008.

[81] T. Zhang, P. Pathak, S. Karandikar, R. Giorno, and L. Que, "A polymer nanostructured Fabry–Perot interferometer based biosensor," *Biosens. Bioelectron.*, vol. 30, no. 1, pp. 128–132, 2011.

[82] Q. Liu, Y. Shin, J. Sheng, K. Woo, S. Rafeah, M. Rafei, A. Promoda, X. Tu, G. Lo, E. Ricci, M. Colombel, E. Chiong, J. Paul, and M. Kyoung, "Mach–Zehnder interferometer (MZI) point-of-care system for rapid multiplexed detection of microRNAs in human urine specimens," *Biosens. Bioelectron.*, vol. 71, pp. 365–372, 2015.

[83] W. Z. Song, X. M. Zhang, A. Q. Liu, C. S. Lim, P. H. Yap, and H. M. M. Hosseini, "Refractive index measurement of single living cells using on-chip Fabry-Pérot cavity," *Appl. Phys. Lett.*, vol. 89, pp. 203901-1-203901–3, 2006.

[84] K. Misiakos, I. Raptis, E. Makarona, A. Botsialas, A. Salapatas, P. Oikonomou, A. Psarouli, P. S. Petrou, S. E. Kakabakos, K. Tukkiniemi, M. Sopanen, and G. Jobst, "All-silicon monolithic Mach-Zehnder interferometer as a refractive index and bio-chemical sensor," *Opt. Express*, vol. 22, no. 22, pp. 329–333, 2014.

[85] P. L. Gourley, "Biocavity laser for high-speed cell and tumour biology," *J. Phys. D. Appl. Phys.*, vol. 36, pp. R228–R239, 2003.

[86] T. Tumolo, L. Angnes, and M. S. Baptista, "Determination of the refractive index increment (dn/dc) of molecule and macromolecule solutions by surface plasmon resonance," *Anal. Biochem.*, vol. 333, no. 2, pp. 273–279, 2004.

[87] S. Elmore, "Apoptosis: a review of programmed cell death.," *Toxicol. Pathol.*, vol. 35, no. 4, pp. 495–516, 2007.

[88] "Refractive index of SCHOTT - multiple purpose - BOROFLOAT33." [Online]. Available: https://refractiveindex.info/?shelf=glass&book=SCHOTT-multipurpose&page=BOROFLOAT33.

[89] S. Kedenburg, M. Vieweg, T. Gissibl, and H. Giessen, "Linear refractive index and absorption measurements of nonlinear optical liquids in the visible and near-infrared spectral region," *Opt. Mater. Express*, vol. 2, no. 11, p. 1588, Oct. 2012.

[90] J. V. Herráez and R. Belda, "Refractive Indices, Densities and Excess Molar Volumes of Monoalcohols + Water," *J. Solution Chem.*, vol. 35, no. 9, pp. 1315–1328, Jul. 2006.

[91] S. Kedenburg, M. Vieweg, T. Gissibl, and H. Giessen, "Linear refractive index and absorption measurements of nonlinear optical liquids in the visible and near-infrared spectral region," *Opt. Mater. Express*, vol. 2, no. 11, pp. 1588–1611, 2012.

[92] E. Sani and A. Dell'Oro, "Optical constants of ethylene glycol over an extremely wide spectral range wide spectral range," *Opt. Mater. (Amst).*, vol. 37, pp. 36–41, 2014.

[93] N. Argov, D. G. Lemay, and J. B. German, "Milk fat globule structure and function: nanoscience comes to milk production," *Trends Food Sci. Technol.*, vol. 19, no. 12, pp. 617–623, 2008.

[94] V. Tuchin, *Tissue Optics: Light Scattering Methods and Instruments for Medical Diagnosis*. SPIE Press, Bellingham, WA, 2007.

[95] J. Yim, H. Kim, S. Ryu, S. Song, H. O. Kim, K. A. Hyun, H. Il Jung, and C. Joo, "Photothermal spectral-domain optical coherence reflectometry for direct measurement of hemoglobin concentration of erythrocytes," *Biosens. Bioelectron.*, vol. 57, pp. 59–64, 2014.

[96] V. V Tuchin, "Handbook of Optical Sensing of Glucose in Biological Fluids and Tissues," in *Handbook of Optical Sensing of Glucose in Biological Fluids and Tissues Series in Medical Physics and Biomedical Engineering*, CRC Press, 2009, p. 419.

[97] V. V Tuchin, X. Xu, and R. K. Wang, "Dynamic optical coherence tomography in studies of optical clearing, sedimentation, and aggregation of immersed blood," *Appl. Opt.*, vol. 41, no. 1, pp. 258–271, 2002.

[98] M. Brezinski, K. Saunders, C. Jesser, X. Li, and J. Fujimoto, "Index matching to improve optical coherence tomography imaging through blood.," *Circulation*, vol. 103, no. 15, pp. 1999–2003, 2001.

[99] C. L. Curl, C. J. Bellair, T. Harris, B. E. Allman, P. J. Harris, A. G. Stewart, A. Roberts, K. a. Nugent, and L. M. D. Delbridge, "Refractive index measurement in viable cells using quantitative phase-amplitude microscopy and confocal microscopy," *Cytom. Part A*, vol. 65, pp. 88–92, 2005.

[100] R. Barer, "Determination of dry mass, thickness, solid and water concentration in living cells.," *Nature*, vol. 172, pp. 1097–1098, 1953.

[101] N. Lue, W. Choi, G. Popescu, Z. Yaqoob, K. Badizadegan, R. R. Dasari, and M. S. Feld, "Live cell refractometry using hilbert phase microscopy and confocal reflectance microscopy," *J. Phys. Chem. A*, vol. 113, pp. 13327–13330, 2009.

[102] W. J. Choi, D. I. Jeon, S.-G. Ahn, J.-H. Yoon, S. Kim, and B. H. Lee, "Full-field optical coherence microscopy for identifying live cancer cells by quantitative measurement of refractive index distribution.," *Opt. Express*, vol. 18, no. 22, pp. 23285–23295, 2010.

[103] Z. Wang, K. Tangella, A. Balla, and G. Popescu, "Tissue refractive index as marker of disease," *J. Biomed. Opt.*, vol. 16, no. 11, pp. 116017-1–116017-7, 2011.

[104] L. K. Chin, a. Q. Liu, C. S. Lim, X. M. Zhang, J. H. Ng, J. Z. Hao, and S. Takahashi, "Differential single living cell refractometry using grating resonant cavity with optical trap," *Appl. Phys. Lett.*, vol. 91, pp. 243901-1–243901-3, 2007.

[105] V. Backman, M. B. Wallace, L. T. Perelman, J. T. Arendt, R. Gurjar, M. G. Müller, Q. Zhang, G. Zonios, E. Kline, J. a McGilligan, S. Shapshay, T. Valdez, K. Badizadegan, J. M. Crawford, M. Fitzmaurice, S. Kabani, H. S. Levin, M. Seiler, R. R. Dasari, I. Itzkan, J. Van Dam, and M. S. Feld, "Detection of preinvasive cancer cells.," *Nature*, vol. 406, pp. 35–36, 2000.

[106] Y. Liu, S. Uttam, S. Alexandrov, and R. K. Bista, "Investigation of nanoscale structural alterations of cell nucleus as an early sign of cancer.," *BMC Biophys.*, vol. 7, no. 1, pp. 1–16, 2014.

[107] X. J. Liang, a. Q. Liu, C. S. Lim, T. C. Ayi, and P. H. Yap, "Determining refractive index of single living cell using an integrated microchip," *Sensors Actuators, A Phys.*, vol. 133, pp. 349–354, 2007.

[108] P. Wang, R. Bista, R. Bhargava, R. E. Brand, and Y. Liu, "Spatial-domain low-coherence quantitative phase microscopy for cancer diagnosis," *Opt. Lett.*, vol. 35, no. 17, pp. 2840–2842, 2010.

[109] R. K. Bista, S. Uttam, P. Wang, K. Staton, S. Choi, C. J. Bakkenist, D. J. Hartman, R. E. Brand, and Y. Liu, "Quantification of nanoscale nuclear refractive index changes during the cell cycle.," *J. Biomed. Opt.*, vol. 16, no. 7, pp. 70503-1–70503-3, 2011.

[110] C. Ma, M. Song, Y. Zhang, M. Yan, M. Zhang, and H. Bi, "Nickel nanowires induce cell cycle arrest and apoptosis by generation of reactive oxygen species in HeLa cells," *Toxicol. Reports*, vol. 1, pp. 114–121, 2014.

[111] X. Wu, "Dual AO/EB Staining to Detect Apoptosis in Osteosarcoma Cells Compared with Flow Cytometry," *Med. Sci. Monit. Basic Res.*, vol. 21, pp. 15–20, 2015.

[112] P. Wang, R. K. Bista, W. Qiu, W. E. Khalbuss, L. Zhang, R. E. Brand, and Y. Liu, "An insight into statistical refractive index properties of cell internal structure via low-coherence statistical amplitude microscopy.," *Opt. Express*, vol. 18, no. 21, pp. 21950–21958, 2010.

[113] B. Rappaz, A. Barbul, Y. Emery, R. Korenstein, C. Depeursinge, P. J. Magistretti, and P. Marquet, "Comparative study of human erythrocytes by digital holographic microscopy, confocal microscopy, and impedance volume analyzer," *Cytom. Part A*, vol. 73, no. 10, pp. 895–903, 2008.

[114] S. Uttam, R. K. Bista, K. Staton, S. Alexandrov, S. Choi, C. J. Bakkenist, D. J. Hartman, R. E. Brand, and Y. Liu, "Investigation of depth-resolved nanoscale structural changes in regulated cell proliferation and chromatin decondensation," *Biomed. Opt. Express*, vol. 4, no. 4, pp. 596–613, 2013.

[115] M. A. Choma, A. K. Ellerbee, C. Yang, T. L. Creazzo, and J. A. Izatt, "Spectral-domain phase microscopy," *Opt. Lett.*, vol. 30, no. 10, pp. 1162–1164, 2005.

[116] W. Z. Song, A. Q. Liu, S. Swaminathan, C. S. Lim, P. H. Yap, and T. C. Ayi, "Determination of single living cell's dry/water mass using optofluidic chip," *Appl. Phys. Lett.*, vol. 91, no. 22, pp. 89–92, 2007.

[117] H. Nakahara, T. Otani, T. Sasaki, Y. Miura, Y. Takai, and M. Kogo, "Involvement of Cdc42 and Rac small G proteins in invadopodia formation of RPMI7951 cells," *Genes Cells*, pp. 1019–1027, 2003.

[118] T. Yasokawa, I. Ishimaru, M. Kondo, S. Kuriyama, T. Masaki, K. Takegawa, and N. Tanaka, "A method for measuring the three-dimensional refractive-index distribution of single cells using proximal two-beam optical tweezers and a phase-shifting Mach-Zehnder interferometer," *Opt. Rev.*, vol. 14, no. 4, pp. 161–164, 2007.

[119] Y. C. Tung, N. T. Huang, B. R. Oh, B. Patra, C. C. Pan, T. Qiu, P. K. Chu, W. Zhang, and K. Kurabayashi, "Optofluidic detection for cellular phenotyping.," *Lab Chip*, vol. 12, no. 19, pp. 3552–3565, Oct. 2012.

[120] N. Lue, G. Popescu, T. Ikeda, R. R. Dasari, K. Badizadegan, and M. S. Feld, "Live cell refractometry using microfluidic devices.," *Opt. Lett.*, vol. 31, no. 18, pp. 2759–2761, 2006.

[121] V. Yashunsky, V. Lirtsman, M. Golosovsky, D. Davidov, and B. Aroeti, "Real-time monitoring of epithelial cell-cell and cell-substrate interactions by infrared surface plasmon spectroscopy," *Biophys. J.*, vol. 99, no. 12, pp. 4028–4036, 2010.

[122] W. Choi, C. Fang-Yen, K. Badizadegan, S. Oh, N. Lue, R. R. Dasari, and M. S. Feld, "Tomographic phase microscopy," *Nat. Methods*, vol. 4, no. 9, pp. 1–3, 2007.

[123]   H. B. Mann and D. R. Whitney, "On a test of whether one of two random variables is stochastically larger than the other," *Ann. Math. Stat.*, vol. 18, no. 1, pp. 50–60, 1947.

[124]   L. Fiorani, R. Fantoni, A. Lai, and A. Palucci, "First simultaneous determination of size, refractive index, light scattering depolarization and fluorescence of phytoplankton cells by laser scanning flow cytometry," *EARSeL eProceedings*, vol. 6, no. 2, pp. 47–57, 2007.

[125]   S. G. Ackleson and R. W. Spinrad, "Size and refractive index of individual marine participates: a flow cytometric approach.," *Appl. Opt.*, vol. 27, no. 7, pp. 1270–1277, 1988.

[126]   R. E. Green, H. M. Sosik, R. J. Olson, and M. D. DuRand, "Flow cytometric determination of size and complex refractive index for marine particles: comparison with independent and bulk estimates," *Appl. Opt.*, vol. 42, no. 3, pp. 526–541, 2003.

[127]   J. Zhao, L. Bowman, X. Zhang, X. Shi, B. Jiang, V. Castranova, and M. Ding, "Metallic nickel nano- and fine particles induce JB6 cell apoptosis through a caspase-8/AIF mediated cytochrome c-independent pathway," *J. Nanobiotechnology*, vol. 7, no. 2, pp. 1–13, 2009.

[128]   A. Oblak, J. Pohar, and R. Jerala, "MD-2 Determinants of Nickel and Cobalt-Mediated Activation of Human TLR4," *PLoS One*, vol. 10, no. 3, pp. 1–15, 2015.

[129]   P. Foladori, A. Quaranta, and G. Ziglio, "Use of silica microspheres having refractive index similar to bacteria for conversion of flow cytometric forward light scatter into biovolume," *Water Res.*, vol. 42, no. 14, pp. 3757–3766, 2008.

[130]   G. Rigamonti, M. Guardamagna, V. Bello, S. Marconi, F. Auricchio, and S. Merlo, "Flow-through micro-capillary refractive index sensor based on T/R spectral shift monitoring," *Biomed. Opt. Express*, vol. 8, no. 10, pp. 4438–4453, 2017.

[131]   C. Peucheret, "Note on Fabry-Pérot Interferometers," *DTU Fotonik*, vol. 1, no. 1. pp. 1–9, 2011.

[132]   F. Carpignano, G. Rigamonti, T. Migliazza, and S. Merlo, "Refractive Index Sensing in Rectangular Glass Micro-Capillaries by Spectral Reflectivity Measurments," *IEEE J. Sel. Top. Quantum Electron.*, vol. 22, no. 3, pp. 383–391, 2016.

[133] G. Rigamonti and S. Merlo, "A novel microfluidic sensing platform based on miniature rectangular glass capillaries and optical read-out," in *ECCTD 2017 Special Session on "Microfluidics Systems: Technology and Applications*, 2017, pp. 1–4.

[134] G. Rigamonti, S. Merlo, F. Carpignano, "Spectral reflectivity measurements on glass capillaries for micro-fluidic applications," in *18th Italian National Conference on Photonic Technologies (Fotonica 2016)*, 2016, pp. 1–4.

[135] K. Zirk and H. Poetzschke, "A refractometry-based glucose analysis of body fluids," *Med. Eng. Phys.*, vol. 29, pp. 449–458, 2007.

[136] M. Cretich, G. Pirri, F. Damin, I. Solinas, and M. Chiari, "A new polymeric coating for protein microarrays," *Anal. Biochem.*, vol. 332, no. 1, pp. 67–74, 2004.

[137] A. G. Mayes and K. Mosbach, "Molecularly imprinted polymers: useful materials for analytical chemistry?," *Trends Anal. Chem.*, vol. 16, no. 6, pp. 321–332, 1997.

[138] N. Cennamo, L. De Maria, G. D'Agostino, L. Zeni, and M. Pesavento, "Monitoring of Low Levels of Furfural in Power Transformer Oil with a Sensor System Based on a POF-MIP Platform," *Sensors*, vol. 15, no. 4, pp. 8499–8511, 2015.

[139] N. Cennamo, G. D. Agostino, R. Galatus, L. Bibbò, M. Pesavento, and L. Zeni, "Sensors based on surface plasmon resonance in a plastic optical fiber for the detection of trinitrotoluene," *Sensors Actuators B. Chem.*, vol. 188, pp. 221–226, 2013.

[140] G. Pirri, F. Damin, M. Chiari, E. Bontempi, L. E. Depero, R. Molecolare, and S. Chimica, "Characterization of A Polymeric Adsorbed Coating for DNA Microarray Glass Slides," *Anal. Chem.*, vol. 76, no. 5, pp. 1352–1358, 2004.

[141] E. Özkumur, J. W. Needham, D. A. Bergstein, R. Gonzalez, M. Cabodi, J. M. Gershoni, B. B. Goldberg, and M. S. Ünlü, "Label-free and dynamic detection of biomolecular interactions for high-throughput microarray applications," *Proc. Natl. Acad. Sci. U. S. A.*, vol. 105, no. 23, pp. 7988–7992, Jun. 2008.

[142] E. Özkumur, A. Yalçın, M. Cretich, C. A. Lopez, D. A. Bergstein, B. B. Goldberg, M. Chiari, and M. S. Ünlü, "Quantification of DNA and Protein Adsorption by Optical Phase Shift," *Biosens. Bioelectron.*, vol. 25, no. 1, pp. 167–172, Sep. 2009.

[143] E. Özkumur, S. Ahn, A. Yalçın, C. A. Lopez, E. Çevik, R. J. Irani, C. DeLisi, M. Chiari, and M. Selim Ünlü, "Label-free microarray imaging for direct detection of DNA hybridization and single-nucleotide mismatches," *Biosens. Bioelectron.*, vol. 25, no. 7, pp. 1789–1795, 2010.

[144] C. A. Lopez, G. Daaboul, R. Vedula, E. Özkumur, D. A. Bergstein, T. W. Geisbert, H. E. Fawcett, J. H. Connor, B. B. Goldberg, and M. S. Ünlü, "Label-free, multiplexed virus detection using spectral reflectance imaging," *Biosens. Bioelectron.*, vol. 26, no. 8, pp. 3432–3437, Apr. 2011.

[145] D. Sevenler, O. Avci, and M. S. Ünlü, "Quantitative interferometric reflectance imaging for the detection and measurement of biological nanoparticles," *Biomed. Opt. Express*, vol. 8, no. 6, pp. 2976–2989, Jun. 2017.

[146] S. M. Scherr, G. G. Daaboul, J. Trueb, D. Sevenler, H. Fawcett, B. Goldberg, J. H. Connor, and M. S. Ünlü, "Real-Time Capture and Visualization of Individual Viruses in Complex Media," *ACS Nano*, vol. 10, no. 2, pp. 2827–2833, 2016.

[147] E. Seymour, G. G. Daaboul, X. Zhang, S. M. Scherr, N. L. Ünlü, J. H. Connor, and M. S. Ünlü, "DNA-Directed Antibody Immobilization for Enhanced Detection of Single Viral Pathogens," *Anal. Chem.*, vol. 87, no. 20, pp. 10505–10512, 2015.

[148] O. Avci, N. L. Ünlü, A. Y. Özkumur, and M. S. Ünlü, "Interferometric Reflectance Imaging Sensor (IRIS)—A Platform Technology for Multiplexed Diagnostics and Digital Detection," *Sensors*, vol. 15, no. 7, pp. 17649–17665, 2015.

[149] A. P. Reddington, "Instrument desing and optimization of Interferometric Reflectance Imaging Sensors for in vitro diagnostic," Boston University, 2014.

[150] R. Vedula, G. Daaboul, A. Reddington, E. Özkumur, and D. A. Bergstein, "Self-referencing substrates for optical interferometric biosensors," *J. Mod. Opt.*, vol. 57, no. 16, pp. 1564–1569, 2010.

[151]   G. Mie, "Beiträge zur Optik trüber Medien, speziell kolloidaler Metallösungen," *Ann. Phys.*, vol. 330, no. 3, pp. 377–445, 1908.

[152]   A. Yurt, G. G. Daaboul, J. H. Connor, B. B. Goldberg, and M. S. Ünlü, "Single nanoparticle detectors for biological applications," *Nanoscale*, vol. 4, no. 3, pp. 715–726, Feb. 2012.

[153]   G. G. Daaboul, C. A. Lopez, J. Chinnala, B. B. Goldberg, and J. H. Connor, "Digital Sensing and Sizing of Vesicular Stomatitis Virus Pseudotypes in Complex Media : A Model for Ebola and Marburg Detection," *ACS Nano*, vol. 8, no. 6, pp. 6047–6055, 2014.

[154]   M. R. Monroe, G. G. Daaboul, A. Tuysuzoglu, C. A. Lopez, F. F. Little, and M. S. Ünlü, "Single Nanoparticle Detection for Multiplexed Protein Diagnostics with Attomolar Sensitivity in Serum and Unprocessed Whole Blood," *Anal. Chem.*, vol. 85, no. 7, pp. 3698–3706, 2013.

[155]   H. J. Lee, D. Nedelkov, and R. M. Corn, "Surface Plasmon Resonance Imaging Measurements of Antibody Arrays for the Multiplexed Detection of Low Molecular Weight Protein Biomarkers," *Anal. Chem.*, vol. 78, no. 18, pp. 6504–6510, Sep. 2006.

[156]   B. P. Nelson, T. E. Grimsrud, M. R. Liles, R. M. Goodman, and R. M. Corn, "Surface Plasmon Resonance Imaging Measurements of DNA and RNA Hybridization Adsorption onto DNA Microarrays," *Anal. Chem.*, vol. 73, no. 1, pp. 1–7, Jan. 2001.

[157]   D. Sevenler, G. Rigamonti, S. Scherr, and M. S. Unlu, "Digital detection and discrimination of nucleic acids with interference reflectance imaging," in *Biosensors 2016: 26th Anniversary World Congress on Biosensors, Gothenburg, Sweden*.

[158]   "KRAS c.35G)A (G12D) Mutation in Colorectal Cancer - My Cancer Genome." [Online]. Available: https://www.mycancergenome.org/content/disease/colorectal-cancer/kras/34/.

[159]   M. Hee, S. Nickerson, E. T. Kim, C. Liot, G. Laurent, R. Spang, and M. R. Philips, "Regulation of RAS oncogenicity by acetylation," *PNAS*, vol. 109, no. 27, pp. 10843–10848, 2012.

[160] J. Neumann, E. Zeindl-Eberhart, T. Kirchner, and A. Jung, "Frequency and type of KRAS mutations in routine diagnostic analysis of metastatic colorectal cancer," *Pathol. - Res. Pract.*, vol. 205, no. 12, pp. 858–862, 2009.

[161] "CHEMICAL RESISTANCE PMMA." [Online]. Available: http://www-eng.lbl.gov/~shuman/XENON/MATERIALS&COMPONENTS/TMA_PMMA/Acrylic-Rod-and-Tube_chemical-resistance.pdf.

[162] Milena Koleva, "Poly(methyl methacrylate) (PMMA),", pp.1-5.

[163] S. Merlo, F. Carpignano, D. Riccardi, G. Rigamonti and M. Norgia, "Infrared structured light generation by optical MEMS and application to depth perception," *2017 IEEE International Workshop on Metrology for AeroSpace (MetroAeroSpace)*, Padua, 2017, pp. 518-522.

[164] F. Carpignano, G. Rigamonti, D. Riccardi, M. De Fazio, S. Merlo, "A Silicon Microsystem for Generation of Infrared Patterned Light," *Journal of Display Technology,* vol. 12, no. 9, pp. 907–911, 2016.

[165] G. Sansoni, M. Trebeschi, and F. Docchio, "State-of-The-Art and Applications of 3D Imaging Sensors in Industry, Cultural Heritage, Medicine, and Criminal Investigation," *Sensors*, vol. 9, no. 1, pp. 568–601, 2009.

[166] K. D. Mankoff and T. A. Russo, "The Kinect : a low-cost , high-resolution , short-range 3D camera," *Earth Surf. Process. Landforms*, vol. 38, no. 9, pp. 926–936, 2013.

[167] W. Zeng and Z. Zhang, "Multimedia at Work Microsoft Kinect Sensor and Its Effect," *IEEE Multimed.*, vol. 19, no. 2, pp. 4–10, 2012.

[168] L. Gallo, A. P. Placitelli, M. Ciampi, and V. Pietro Castellino, "Controller-free exploration of medical image data : experiencing the Kinect," in *2011 24th International Symposium on Computer-Based Medical Systems (CBMS), Bristol*, 2011, pp. 1–6.

[169] E. C. Marinelli and W. A. Rogers, "Identifying potential usability challenges for XBOX 360 Kinect exergames for older adults," in *Proceedings of the Human Factors and Ergonomics Society 58th Annual Meeting - 2014*, 2014, pp. 1247–1251.

[170]   J. I. Laughner, S. Zhang, H. Li, C. C. Shao, I. R. Efimov, J. I. Laughner, S. Zhang, H. Li, C. C. Shao, and I. R. Efimov, "Mapping cardiac surface mechanics with structured light imaging Mapping cardiac surface mechanics with structured light imaging," *Am. J. Physiol. - Hear. Circ. Physiol.*, vol. 303, no. 6, pp. H712–H720, 2012.

[171]   O. V. Olesen, R. R. Paulsen, L. Højgaard, B. Roed, and R. Larsen, "Motion Tracking for Medical Imaging : A Nonvisible Structured Light Tracking Approach," *IEEE Trans. Med. Imaging*, vol. 31, no. 1, pp. 79–87, 2012.

[172]   M. G. L. Gustafsson, "Nonlinear structured-illumination microscopy : Wide-field fluorescence imaging with theoretically unlimited resolution," in *Proceedings of the National Academy of Sciences of the United States of America*, 2005, vol. 102, no. 37, pp. 13081–13086.

[173]   M. G. L. Gustafson, "Surpassing the lateral resolution limit by a factor of two using structured illumination microscopy," *J. Microsc.*, vol. 198, pp. 82–87, 2000.

[174]   T. Wilson, "Method of obtaining optical sectioning by using structured light in a conventional microscope," *Opt. Lett.*, vol. 22, no. 24, pp. 1905–1907, 1997

List of Figures

List of Publications

ISI Journals:

[1]   Giulia Rigamonti, Marco Guardamagna, Valentina Bello, Stefania Marconi, Ferdinando Auricchio, Sabina Merlo, "Flow-through micro-capillary RI sensor based on T/R spectral shift monitoring", Biomedical Optics Express, vol. 8, no. 10, pp. 4438-4453, 2017. 10.1364/BOE.8.004438

[2]   Giulia Rigamonti, Marco Guardamagna, Sabina Merlo, "Non-contact reflectometric read-out of disposable microfluidic devices by near infra-red low-coherence interferometry", AIMS Biophysics, vol. 3, no. 4, pp. 585-595, 2016. 10.3934/biophy.2016.4.585

[3]   Francesca Carpignano, Giulia Rigamonti, Giuliano Mazzini, Sabina Merlo, "Low-coherence reflectometry for RI measurements of cells in micro-capillaries", Sensors, vol. 16, no. 10, 1670, 2016. 10.3390/s16101670

[4]   Francesca Carpignano, Giulia Rigamonti, Domenico Riccardi, Marco De Fazio, Sabina Merlo, "A silicon microsystem for generation of infrared patterned light", IEEE Journal of Display Technology, vol. 12, no. 9, pp. 907-911, 2016. 10.1109/JDT.2016.2543962

[5]   Francesca Carpignano, Giulia Rigamonti, Tommaso Migliazza, Sabina Merlo, "RI sensing in rectangular glass micro-capillaries by spectral reflectivity measurements", IEEE Journal of Selected Topics in Quantum Electronics (Special Issue on Biophotonics), vol. 22, no. 3, pp. 383-391, 2016. 10.1109/JSTQE.2015.2455339

[6]   Francesca Carpignano, Giulia Rigamonti, Sabina Merlo, "Characterization of rectangular glass micro-capillaries by low-coherence reflectometry", IEEE Photonics Technology Letters, vol. 27, no. 10, pp. 1064-1067, 2015. 10.1109/LPT.2015.2407271

Conference proceedings:

[7]   Giulia Rigamonti, Sabina Merlo, "A novel microfluidic sensing platform based on miniature rectangular glass capillaries and optical read-out", ECCTD 2017 Special Session on "Microfluidics Systems: Technology and Applications", pp. 4-6 Sept. 2017.

[8]   Sabina Merlo, Francesca Carpignano, Domenico Riccardi, Giulia Rigamonti, Michele Norgia, "Infrared structured light generation by optical MEMS and application to depth perception", 2017 IEEE International Workshop on Metrology for AeroSpace (MetroAeroSpace), Padua, pp. 518-522, June 2017.10.1109/MetroAeroSpace.2017.7999628

[9]   Giulia Rigamonti, Francesca Carpignano, Giuliano Mazzini, Sabina Merlo, "Cell RI sensing in rectangular glass micro-capillaries", 5th International Conference on Bio-Sensing Technology, Riva Del Garda, May 2017.

[10]   Giulia Rigamonti, Francesca Carpignano, Giuliano Mazzini, Sabina Merlo, "Low-coherence reflectometry for cell RI sensing", 19th Italian National Conference on Photonic Technologies (Fotonica 2017), Padua, May 2017.

[11]   Giulia Rigamonti, Francesca Carpignano, "Reconfigurable setup for solution concentration detection in rectangular capillary", V Congresso Nazionale di Bioingegneria, Naples, June 2016.

[12]   Giulia Rigamonti, Sabina Merlo, Francesca Carpignano, "Spectral reflectivity measurements on glass capillaries for micro-fluidic applications", 18th Italian National Conference on Photonic Technologies (Fotonica 2016), Rome, pp. 1-4, 2016. 10.1049/cp.2016.0898.

[13]   D. Sevenler, G. Rigamonti, S. Scherr, M.S. Unlu, "Digital detection and discrimination of nucleic acids with interferometric reflectance imaging", Biosensor 2016, 26° Anniversary World Congress on Biosensors, Gothenburg, Sweden, May 2016.

[14]   G. Rigamonti, S. Merlo, F. Carpignano, "Rectangular glass micro-capillaries for biophotonic applications", 2015 Fotonica AEIT Italian Conference on Photonics Technologies, Turin, pp. 1-4, May 2015. 10.1049/cp.2015.0185.